University of Liège
Faculty of Applied Sciences

Application of the time-domain induced polarization technique to characterize the ORman gold prospect in Mondulkiri Province, Cambodia

supervised by
Dr. Nguyen Frédéric

Graduation Studies conducted for obtaining the Master's degree in Mining and Geological Engineering by

Thibaut Robin

Academic year 2016 - 2017

Acknowledgements

First of all, I would like to thank my supervisors, Professor Frédéric Nguyen and Doctor Bun Kim Ngun (Institute of Technology of Cambodia), who made this project possible and sparked my interest in new subjects.

I want to express my gratitude to Craig Johnson (Emerald Resources NL) who gladly provided us the means to conduct our work, and made us discover the OKvau Exploration Camp.

It was fantastic to have the opportunity of sharing this adventure with Annie Royen and Doctor Thomas Kremer, with whom I spent unforgettable times in the jungles of Cambodia.

Special thanks to the wonderful "IP team" for their help during the investigations, and I really appreciated the company and assistance of the three ITC students that stayed with us during the first week of the survey, Kimhouy Oy, Muoyheang Soy and Reaksmey Kry.

My biggest thanks to the amazing Cambodian people that welcomed us during our two-months stay in the country.

I also want to thank Thomas Hermans and Maxime Evrard who kindly helped me for various technical aspects of the work.

Last but not least, the writing of this thesis was made possible thanks to the wonderful team, family and friends, that surrounded me all along.

Le voyage réalisé dans le cadre du présent travail a été rendu possible grâce au soutien financier de l'Académie de recherche et d'enseignement supérieur de la Fédération Wallonie-Bruxelles, Belgique, dans le cadre de sa politique de Coopération au développement.

The work realized for this master thesis has been supported by the "Académie de Recherche et d'Enseignement supérieur" (ARES) of the Wallonia-Brussels Federation of Belgium.

Abstract

The aim of this thesis is to develop a new approach in the implementation of the minimum gradient support regularization operator, applied to a time-domain induced polarization problem. Indeed, this promising functional has not been enough implemented in real and large surveys yet. It is mainly confined to research studies applied to synthetic cases, although it can often offer significant advantages compared to the traditional smooth inversions, according to Occam's principle. The resistivity and induced polarization data was acquired during a geophysical campaign in Mondulkiri Province, Cambodia, on the largest known gold resource of the country. The deposit is an Intrusion Related Gold system, characterized by polarizable sulphides minerals. Four long profiles were realized on the contact zone between a magmatic intrusive and the hosting sediment formations, which is a zone of interest concerning gold mineralizations. By implementing different inversion approaches and tuning the focusing parameter, the a-priori information has revealed itself as being of uttermost importance on the process convergence towards a stable and realistic solution, and a methodology is therefore established.

Keywords : minimum gradient support, focusing parameter, sharp inversion, induced polarization, resistivity, Cambodian gold deposit.

Contents

List of Figures

List of Tables

Chapter 1

Introduction

> The explanation requiring the fewest assumptions is most likely to be correct.
>
> William of Ockham, 1287–1347 A.C.

The global objective of this work is to develop a methodology for the sharp inversion of resistivity and induced polarization problems.

In order to do so, data was collected during a two-week survey in March/April 2017, Mondulkiri Province, Cambodia, over the largest known gold deposit in the country, called the OKvau Project. It belongs to the recently defined Intrusion Related Gold System class of deposits (Hart, 2005). The mineralizations are associated to sulphides, mainly arsenopyrite, pyrite and pyrrhotite. The exploitation rights belong to Emerald Resources NL, and the exploration is handled by Renaissance Minerals Cambodia Ltd., a Cambodian branch of the first company. At that time the project was in the Definitive Feasibility Study process.

The main problem discussed here is the recovery from observed data of objects that are *not smooth* in nature. Smoothness is a feature that most of today's inversion schemes are implemented with, according to Occam's razor principle. An example is the famous Res2dinv software (Loke, 2017).

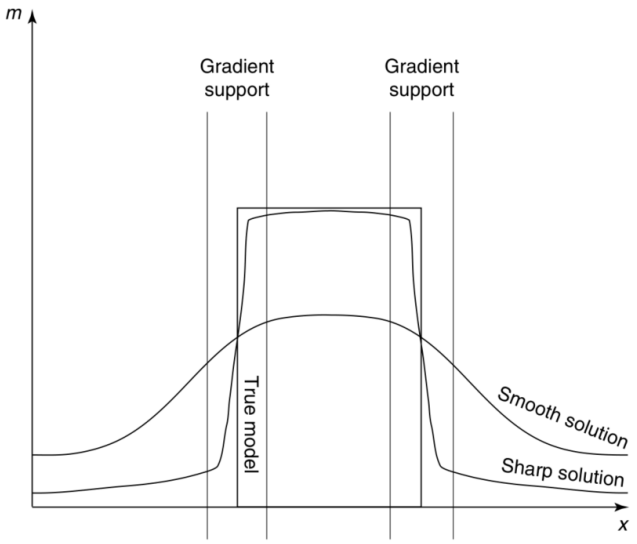

Figure 1.1: Illustration of the principle of a sharp inversion. Here, the true model is a rectangle. The smooth solution produces a model that does not match reality, contrarily to the sharp one (Zhdanov, 2009).

A new method that "minimizes the area where strong model parameter variations and discontinuity occur", named the *minimum gradient support*, was developed in 1999 by Portniaguine and Zhdanov. It was based on the previous work of Last and Kubik (1983), who wanted to maximize the compactness of causative bodies to recover plausible geological features. It was refined and modified by several authors over the years. Specifically, the implementation of the minimum gradient support requires the user to choose a *focusing parameter*, commonly named β. There is no universal method concerning the selection of this value. It is left to the user based on their experience or the level of satisfaction the solution procures, which is very subjective. Several authors have explored different approaches over the years. Their contributions are detailed hereafter.

Last and Kubik (1983) first consider a **Minimum Support functional**, a new criterion for the inversion of gravity data. The aim is to maximize the compactness (minimize the volume) of causative bodies, in order to recover desirable and plausible geological features. Their recommendation concerning the β-value is to choose a value that is "sufficiently small", relatively to machine precision (10^{-11} in their case).

Portniaguine and Zhdanov (1999) tackle the problem of developing a stable inverse procedure that can resolve complex geological features, contrarily to the traditional smoothness constraint approach which provides unfocused images. They are the first to introduce the **Minimum Gradient Support functional**. However, they do not discuss the choice of β.

Zhdanov and Tolstaya (2004) describe a "new approach to sharp boundary geophysical inversion" applied to a synthetic 3D magnetotelluric inverse problem. They propose a method to estimate the optimum value of β in a similar fashion than the regularization parameter in the L-curve approach; starting from the starting model m_0 (m_i = model parameters at iteration i, $i \geq 0$), they plot the normalized value of the minimum support stabilizer versus β. The result is a monotonically decreasing function, where β is chosen to be in the vicinity of the maximum convex curvature point.

Zhdanov et al. (2006) apply the Minimum Support functional to a crosswell travel-time tomography problem. They utilize the approach developed in Zhdanov and Tolstaya (2004) for selecting the focusing parameter value. They use synthetic models with at most two anomalous bodies.

Ajo-Franklin et al. (2007) develop a differential traveltime tomography algorithm which produces compact models, adapted from the minimum support regularization methods, and then apply it to a real CO_2 sequestration monitoring dataset. As for the choice of β, they consider the approach cited above, and decide to fix it at a "reasonable value" determined by their experience, typically between 10^{-7} and 10^{-4}.

Blaschek et al. (2008) present a "new sensitivity-controlled focusing regularization scheme for the inversion of induced polarization data based on the minimum gradient support". They study the regularization term variation as a function of the model gradient for different values of β for various synthetic cases, and conclude that an optimal β value exists. Their recommended value is $\beta_{opt} = 3.0 \times 10^{-1}$. However, they also suggest that "instead of using a standard value for β, it is also possible to scan through a range of different values and select the result that corresponds best with available a priori information on the model".

Rosas Carbajal et al. (2012) study the use of radio and audio magnetotelluric data to monitor groundwater processes. For the numerical experiments considered in their work, they find that $\beta = \sum_{n=1}^{N} |\frac{m_n}{N}|$ (with $m_n = n_{th}$ model parameter) produces "satisfactory solutions".

Nguyen et al. (2016) propose a data-driven selection of the β-value relying on the data misfit only, applied to a time-lapse resistivity case. They select β by performing a line-search at the first iteration, and choosing the value that minimizes the data misfit. The value is then kept constant during the inversion process.

In the previous studies, some authors use the MS functional, and others the MGS. Their formulation is similar. They are stabilizers that pick inverse models from a class of models with the minimum area or volume of the domain where the anomalous parameters distribution lie (MS), or inverse models with a minimum area or volume where the gradient of the

model parameters is non-zero (MGS) (Zhdanov, 2009). A full description of the stabilizers can be found in Chapter 9.

Few of those studies have presented inversions results with a varying β, and several authors only justify their choice by experience or by the obtention of "satisfactory results". Furthermore, their applications are too often restricted to synthetic data with one or two bodies to resolve. During the combination of the literature studies, I haven't found a single documented case of the use of the MS or the MGS functionals for real and large investigation data.

It is clear that there is a gap in geophysics around the implementation of the Minimum Gradient Support functional, perhaps because common softwares haven't implemented it in their core, due to the subjective choice of the focusing parameter, or a combination of both. The traditional Occam inversion is useful when the user has initially no idea what to look for in his data, but its results can be questioned when a-priori knowledge indicates that smooth parameter variations *should not* naturally occur in the subsurface.

Numerous trials have shown that none of the outlined approaches can directly be applied in the inversion of the field datasets of this work. A combination of the most interesting ideas and the development of new ones will be necessary in order to find satisfactory solutions.

I will try to prove that the minimum gradient approach can successfully be implemented for large DC/IP surveys, that it provides pertinent results, and develop a framework concerning the choice of the focusing parameter. To do so, a complete theoretical and contextual background is realized, compiling all the available information kindly provided by Renaissance Minerals Ltd., to allow an objective assessment of the obtained results. I noticed in the preliminary inversions a great influence of the a-priori information on the inversion process. It will be further explored to develop new methods for the choice of the focusing parameter β.

Structure

- Chapter 2 describes the geographical and geological context of the investigation area.
- Chapter 3 introduces the basic theory behind the electrical properties of earth materials.
- Chapter 4 presents the results of a petrophysical study of rock samples collected in the survey area.
- Chapter 5 explains the different data acquisition techniques when dealing with electrical methods.
- Chapter 6 justifies the survey lines design based on the objectives of the work.
- Chapter 7 outlines some geophysical studies conducted by private consultants prior to this investigation.
- Chapter 8 unfolds the theory behind the inversion techniques.
- Chapter 9 points out the properties of the Minimum Gradient Support, and trials on synthetic models are conducted.
- Chapter 10 tests the properties of the Minimum Gradient Support on several synthetic cases, in the aim of developing a methodology to use on the field data.
- Chapter 11 gets across the processing of the collected data before it can be used in the inversion process.
- Chapter 12 presents the field data inversion results and their interpretation.
- Chapter 13 concludes the thesis and discusses about future perspectives.

Softwares used

- The preliminary inversions *on the fly* during the investigations were realized thanks to Res2Dinv (Geotomo Software) (Loke, 2017).
- The inversion code used in the framework of this study is CRTomo (Kemna, 2000), with the forward modeling based on a finite element scheme, and the inversion algorithm implemented with particular schemes.
- Wolfram Mathematica was extensively used for data processing and visualization, image analysis and other figures generation (Wolfram Research Inc., 2017).
- Several illustrations were realized with Adobe Illustrator CC 2017.

Chapter 2

Geographical and geological context

Synopsis

The geographical background is briefly described before introducing the geological and mineralization contexts. The aim of this chapter is to bring light into the formation of the OKvau deposit as well as into the nature and history of the mineralizations. Once the variety of materials described, the next chapter will introduce the electrical properties of rocks.

2.1 Geographical context

The OKvau gold deposit is located in the forests of the Mondulkiri Province, Cambodia, South-East Asia (Figure 2.1).

2.1.1 Topography

The topography of the OKvau Project area is undulating (see Figure 2.2), with a relief 80 to 200 meters above sea level. It is divided by several episodic drainage merging with the perennial Prek Te River flowing south-west approximately 600 m north of the gold deposit. The project is based within a sub-catchment of the Prek Te, with an area about 19.8 km^2. The topography was thus quite favorable towards the equipment positioning and data acquisition. Furthermore, a sediment layer was almost always present in order to plant the electrodes. Few of them were missed because of rock outcrops.

2.1.2 Environment

OKvau is positioned in the south-eastern Indochina Dry Evergreen Forests ecoregion (tropical dry broadleaf forest), undergoing long dry and wet seasons. The data acquisition occurred in late March/early April in the heart of the dry season. Those conditions were favourable regarding the vegetation density and the fauna, since the field trips took place in the forest, but very unfavourable towards the electric methods. Indeed, the subsurface was completely dry on the first few meters. However, unexpected heavy raining sparse events completely resolved this problem.

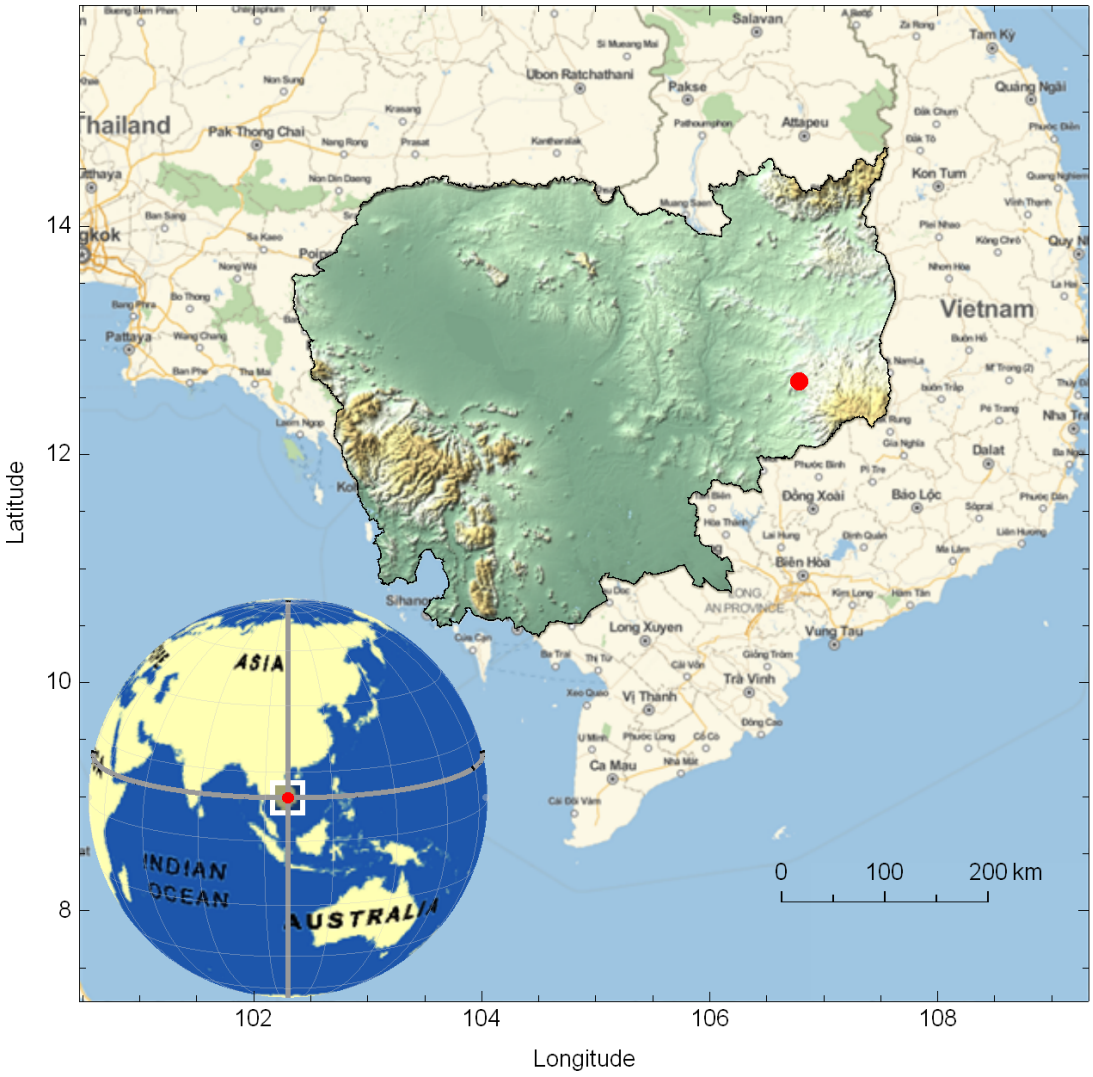

Figure 2.1: Position of the OKvau gold deposit as indicated by the red dot.

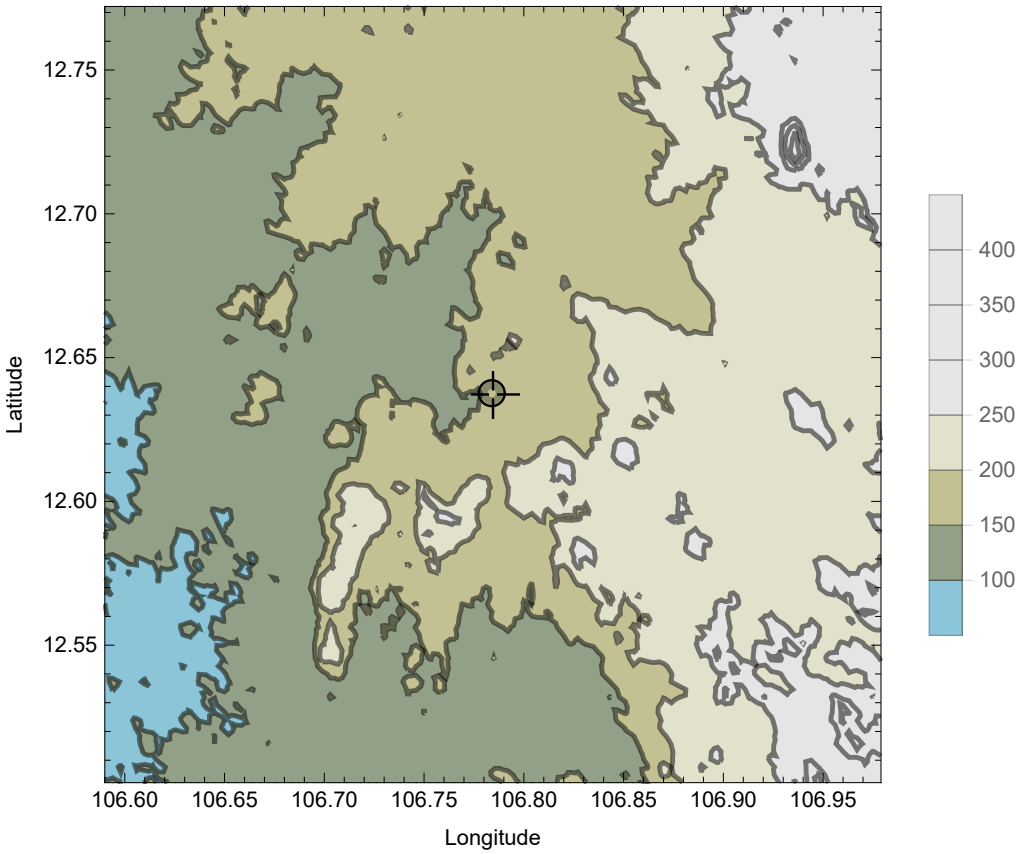

Figure 2.2: Elevation above the sea level around the OKvau gold deposit, in the centre of the map. The units are decimal degrees. The span of the plot is 30 km both in latitude and longitude. Elevation data courtesy of Wolfram Research Inc. (2017).

2.1.3 Artisanal mining

It is worth mentioning that artisanal mining has been occurring at OKvau for more than a decade, and it is one of the reasons the deposit was first "discovered" by Oxiana Ltd., an Australian exploration company that ceased operations in 2008 (Franey, 2014).

Artisanal mining is restricted to shallow, near-surface material. The ore is treated via in-situ cyanide leaching in make-shift vats on site.

The artisans left large and deep pits behind in the Okvau area. During the data acquisition, this posed some problems when a designed profile had to cross one of these. Some electrodes were failed to be placed.

2.2 Geological context

This section is based on the preliminary work of Franey (2014) who compiled the available information gathered over the years to produce a synthetic report on the geology and genesis of the mineralization at the OKvau deposit.

2.2.1 Regional geology

Cambodia is located in the South-Central part of South-East Asia. The tectonic framework is predominated by five magmatic belts Kamvong (2014), surrounding the Indochina Terrane. They are all enriched in copper-gold mineralizations, produced in plates subduction-related contexts. The **Dalat-Kratie** belt, a Cretaceous (U-Pb Zr age : 120-75 Ma), with calc-alkaline, adakitic, I-type plutons in South-East Cambodia, contains the OKvau gold deposit.

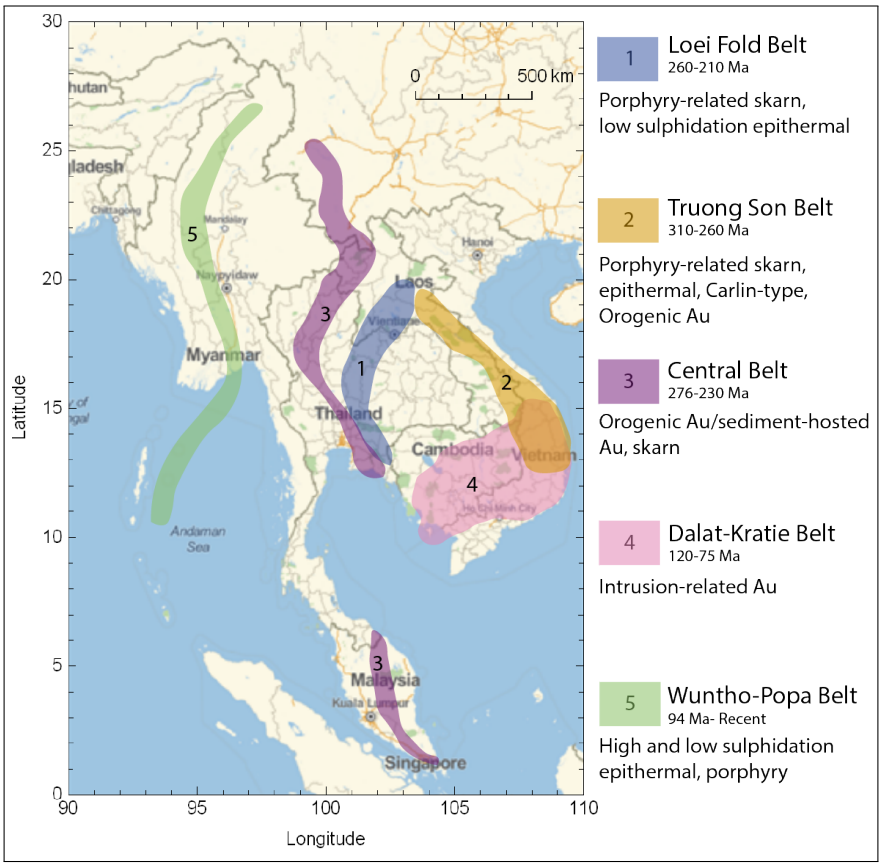

Figure 2.3: Metallogenic belts of South-East Asia. Modified from Kamvong (2014).

2.2.2 Geology of Eastern Cambodia

The stratigraphic sequence of Eastern Cambodia is summarized in Figure 2.4. There is a clear dominant NE-trending structural grain in the region, by the effects of regional dextral shearing. The evidence is obvious in faults and folds relationship, producing classic sigmoidal patterns (King, 2008a). Most of the mineralizations at OKvau is related to mineralized veins, linked to faults and fractures. Their origin is still discussed (Franey, 2014).

Period	Stratigraphy
Quaternary	Alluvium & recent basalt flows
Lower Cretaceous	The *Khorat Sequence* - continental red-bed sequence derived mainly from Khorat Plateau in Thailand. Basal unconformity relates to Indosinian 2 Orogeny (the collision of Shan Thai and West Burma terranes).
Middle Jurassic	
Lower Jurassic	Variegated sequence, transitional between marine and continental conditions, with continental clastics in upper part. Contains volcanics and thin limestone units. Basal unconformityrelates to Indosinian 1 Orogeny (the collision of Indochina with the Shan Thai terrane).
Upper Triassic	
Middle Triassic	Marine sequence, with Permian limestones; no red beds. Basal unconformity relates to the Variscan Orogeny.
Carboniferous	
Lower Carboniferous	Metamorphic basement
Cambrian	

Figure 2.4: Stratigraphy of Eastern Cambodia, from Kamvong (2014).

2.2.3 Local geology

The OKvau gold deposit belongs to the still pubescent and evolving **Intrusion-Related Gold System** model (Hart, 2007). Hart, a world expert on this family of deposits visited himself the OKvau Project in 2008 and confirmed its nature (Franey, 2014).

The local geology of the OKvau area has been assembled from field mapping handled by diverse teams and companies since 2006, combined with drill logs (Franey, 2014). King (2010) described the local geology as follows :

- Most of the mineralization is hosted in a Cretaceous diorite intrusive. The latter is itself hosted in a hornfelsed Triassic sedimentary sequence, which can also bear substantial mineralizations.
- The host sedimentary sequence consists of sandstone and siltstone, variably bedded and hornfelsed. A few bedding parallel shear zones are undeniably existent, and

behaved as preferential conduits for "skarning" fluids. On the other hand, some other greatly altered zones look to be more strictly related to lithological variations within the sedimentary sequence, and/or magmatic intrusion.

- The contact zone between the host sedimentary sequence and the diorite is pretty variable in nature. In some cases, the contact is visibly faulted, but in others it looks like an ordinary intrusive contact. It can be mineralized.

Alliborne (2013) mentioned that the OKvau deposit is essentially enclosed in a 100-200 meters wide north-trending diorite apophysis, on the edge of an meters bigger composite diorite-granitoid pluton. The volume of arsenopyrite-mineralized veins plummets at the junction between the host sedimentary sequence and the intrusive, which points in the direction of the diorite playing a great part in positioning the veins. However, broader mineralized shears persist into the adjacent sedimentary sequence.

The local geological map is displayed on Figure 2.6.

Diorite

Types The igneous rocks are mostly porphyritic in texture, even though a few are inequigranular. Rock type ranges from :

- Microgranodiorite
- Micromonzonite
- Monzodiorite
- Quartz diorite

Alteration Several intrusive rocks present substantial alterations, primary minerals destructions and partial textural annihilation. However, many of the igneous rocks have simply undergone weak to moderate pervasive alteration, mostly of propylitic type. This implies that replacement of primary igneous material occurred by phases, including albite, chlorite, carbonate, sericite, actinolite, epidote-clinozoiste, titanite and trace pyrite, arsenopyrite, chalcopyrite and pyrrhotite (Ashley, 2006). Accessory veining manifests in rock with propylitic alteration, with assemblages including K-feldspar, quartz, carbonate, prehnite, laumonite, pyrrhotite, actinolite, arsenopyrite, chalcopyrite and pyrite. Some of the igneous rocks exhibit much vigorous hydrothermal alteration with replacement by assemblages consisting of one or more of K-feldspar, biotite, amphibole, quartz, sulphides (e.g. arsenopyrite, pyrrhotite, pyrite), rutile and sericite. These strongly altered rocks are thought to be possible examples of endoskarn replacement.

Zonation Alliborne (2014) observed that ilmenite is certainly the prevailing Fe-Ti oxide in samples of the intrusives. When present, magnetite represents roughly $\leq 20\%$ of the Fe-Ti oxide in every sample. Intrusive rock bodies are usually zoned, and the massive diorite body in the OKvau district obeys this rule, as the pluton margin features a somewhat reduced ilmenite-rich mineralogy and the core a more oxidized magnetite-rich mineralogy. This might be a primary characteristic of the magma itself, or a result of the interactions between the intrusion and sedimentary rocks (Alliborne, 2014). Plutons associated to intrusion-related gold deposits usually display reduced oxidation states along the boundary between the magnetite and ilmenite series (Hart and Goldfarb, 2005; Hart, 2007). The presence of both ilmenite and magnetite in the intrusives involves an oxidation state within the dioritic magma similar to that in several other intrusions associated with IRGS. However, the pluton lack of characteristics commonly thought to be linked with intrusive fertile for intrusion-related magmatic hydrothermal gold deposits such as pegmatites, aplites, composite magmatic-hydrothermal veins with sulphide minerals, and miarolitic cavities.

Formation Other data from petrographic and SEM analysis imply that the intrusives crystallized from distinct magma batches enriched in S, H_2O, Cu and W. Some elements of interpretation by Alliborne (2014) regarding some sodic plagioclase-rich cumulate rocks is that they may represent a hybrid link with spatially coincident calc-alkaline lamprophyre dykes. Furthermore, singular coarse-grained K-feldspar-biotite-rich rocks associated with the intrusive could have crystallized from particularly hot potassic hydrothermal fluids or small batches of cooler potassic melts, which might be a sign of hybridisation/mixing/mingling of diorite and lamprophyre melts during the arrival of magma, over the OKvau district.

Dykes

The diorite and sedimentary country rocks are intersected by dykes and sill of various styles. The most common types are massive mafic dykes. Chronologically, dykes intrusions postdate arsenopyrite mineralization, not found in structures deforming the dykes (King, 2010).

Regolith

The regolith is a key feature in geo-electric investigations, since it composes the first layer above the structures of interest, and the electrodes will be planted on top of it. It is through this layer of materials that the current will be injected and transmitted to the deeper parts of the subsurface.

The main characteristics of the regolith at OKvau are (Bolster, 2012) :

- Plenty outcrops (weathered to some extent - saprock), with skeletal soils and/or thin residual soils, several with stone lines/gravel horizons at 30-60 cm depth.
- Shallow depth of oxidation (less than 5 m deep in various cases).
- Few lateritic weathering products, occurring over Fe-rich lithologies, such as pisoliths and ferruginous saprolite.
- Well-developed dendritic drainage, with a lot of channels having outcrops. Amid the wet season, floods may be deep and extensive.
- Confined zones of depositional regime materials, such as colluvial and alluvial plains, but much limited compared to erosional/residual regimes.

In the OKvau area, the electrode planting was made easier since the zone has been gradually cleared of its vegetation for probably more than a decade, first by the artisanal miners and then by the industrials. This lack of vegetation and human activities favours erosion and deposition of layers of soft soil across the area, through which the electrodes are easily placed, especially thanks to the raining events that occurred.

In the ORman area, in the forest, bio-interferences such as tree roots or the presence of rock fragments sometimes posed problem. To counter those issues, the option was taken to dig small holes (15 cm deep) in order to plant the electrodes.

The regolith in the OKvau and ORman area was quite conductive, and presented fairly good contact resistances with the electrodes all along the investigation, which is an important parameter to take into account as noted by Zonge and Hughes (1985).

Structural setting

The defined gold mineralization is primarily hosted in the diorite intrusive. However, significant mineralization seems to be contained in the contact zones between the intrusive and the hornfelsed sediments, which are described by the structural setting.

King (2008b) depicted the local structural setting as follows :

- Regionally, the spatial distribution of Au mineralization gives the idea that it is firmly correlated with a 1 km wide, NE trending brittle deformation zone with unambiguous bounding structures. A collection of data leads to believe that the diorite intrusives were displaced by up to 1.5 km on faults linked to this zone.

- The mineralization is part of a NW trending zone which connects between the bounding structures and transfers displacement. Its location is heavily governed by the existence of the diorite contact (and the related lithological change).
- The ENE trending faults at OKvau are deciphered to be members of a second order Riedel fault zone crossing the NE zone to splay into the SE bounding fault at OKvau. This created a local bend in the bounding structure, which would produce an extensional jog in dextral shearing. Another Riedel shear is present 750 m to the North and displaces the intrusive by approximately 400 m in a dextral sense.
- The sulphidic shear veins are inferred as being extensional faults that assisted extension of the northerly trending diorite contact.

2.2.4 Mineralization

Several consultants tried to bring light on the genetic model of the OKvau deposit, and several interpretations have been realized, perfecting over the years (Franey, 2014). OKvau is fundamentally an As-Bi deposit with accessory associated Au. The abundance of bismuth and arsenic is emblematic of intrusion-related gold deposits (Alliborne, 2014).

Mineralization assemblage In the early phase of exploration, Ashley (2006) noted that the assemblage is constituted of arsenopyrite-pyrite and pyrrhotite. Substantial amount of the latter phase have been retrogressed to secondary pyrite. Chalcopyrite is also found, along with traces of Bi minerals.

Structure and geometry After several ascertainments, Alliborne (2013) claims that the gold is concentrated along a network of brittle shears and arsenopyrite-rich sulphide shears. These shears usually comprehend a 1-5 dm broad core of greatly altered, fractured and/or sheared rock locally with an unsteady planar fabric, encircled by a 0.5-2 m vast, less profoundly altered haloes retaining relict diorite texture. It is not uncommon to find in the heart of the brittle shears variably deformed pyrrhotite, arsenopyrite and/or pyrite-rich layers up to 1 dm wide. The arsenopyrite-rich sulphidic shears are typically a few millimeters to centimeters wide. They occupy the space along extensional fractures with few or no sign of any fabric development.

Gold origin Alliborne (2013) stated that the preeminent spatial amplitude of the alteration haloes around the shears, and textural evidence of undeniable motion along the shears entails that they were the main fluid canal within the deposit. Gold-enriched solutions seemingly reached the fracture mesh hosting the auriferous body through the heavily altered shears.

Type of lodes

The logging and interpretation of several drill holes allowed to recognize different types of structural and mineralization types in OKvau (Franey, 2014). They are summarized by King (2010). The principal types occurring are :

- **"Mylonitic" Faults** These structures present sheared quartz, carbonate and sometimes feldspar bands, with rock flour seams. The "mylonytic" term is only used as descriptive purposes, as the structures resemble the fabric of the true mylonite, the metamorphic rock. These fault zones are sometimes observed to include zones up to quite a few meters, or splay strands down to 50 mm wide, but with fine shear textures. They often occur with a halo of carbonate spotting or prevalent carbonate alteration. Gold-bearing arsenopyrite shears, veins and breccia infill are linked to these zones, even though some are not mineralized.
- **Laminated shears (quartz, feldspar, carbonate)** Those shears are often less than 10 cm wide, but possess well grown laminated structures with typically thin, black rock flour seams. They are associated with the main "mylonitic" shears. This style of shear is usually developed in well bedded sequences as bedding parallel shears, where shearing is firmly enclosed to a shear plane with no damage zone.
- **Mineralized laminated shear with 100 % arsenopyrite** In a few zones of the deposit, these structures represent the major type of alteration.
- **Massive arsenopyrite structures** Those systems bear the greatest grades within the deposit, and can be tracked for distance of more than 100 m, whilst conserving steady and substantial width and grade.
- **Replacement style arsenopyrite** Undeformed arsenopyrite marred by small particles of foreign material is found in two different contexts :
    1. Whilst replacing the borders of pre-existing massive pyrrhotite zones, usually accompanied by pyrite.
    2. Whilst replacing chloritic shears either interpreted as pyroxenite dykes or early chloritic shears. These possible dykes are commonly found with a substantial percentage of replacement pyrrhotite and can present an outstanding shear texture. Some suggested that the massive pyrrhotite veins has grown through extensive replacement of earlier pyroxenite dykes.
- **Low arsenic, gold bearing sulfide zones** Several of these zones exhibit substantial shearing. Illustrations of such zones are commonly massive pyrrhotite and more rarely massive pyrite.

- **Massive pyrrhotite zones** Occurring throughout the deposit but more commonly in the northern part, they fluctuate from heavily sheared to virtually untouched by this phenomenon. They can extend to zones up to 1.5 km wide. They are older than the introduction of the arsenopyrite hosted mineralization and may have been disturbed by later structures, making interpretation difficult.
- **Mineralised zones created by small scale arsenopyrite structures and veins** Small-scale mineralized structures are often established between hanging wall and footwall structures as millimetric to centimetric veins and petty shears. These generate a larger mineralized zone between the higher grade contact structures.
- **Cataclastic/breccia faults** These structures seem to postdate other structures and are rarely mineralized. During drilling, they are correlated with core loss.

Discussion

The geology in the OKvau area is dominated by igneous intrusions within variably hornfelsed, bedded sedimentary formations. The rocks present some alteration often in the form of carbonates minerals. The mineralization occurs in different size and shape. Its genetic history is still not clearly defined but it appears to be associated to fractures zones within the diorites and at the contact intrusion/sediments, linked to sulphides minerals, especially arsenopyrite.

- The source of the signals to expect from the mineralized zones will be discussed in Chapter 4 (Petrophysics).
- The intensity, shape and location of responses to expect from the different causative bodies will be explored in Chapter 7 (Geophysical context).
- Finally, the results from this study, in the light of the previous elements and the geological context, will be presented in Chapter 12.

Figure 2.5: Legend of the geological map (next page). The color legend adopted is the same as the one used by the geologists at Renaissance Minerals Ltd.

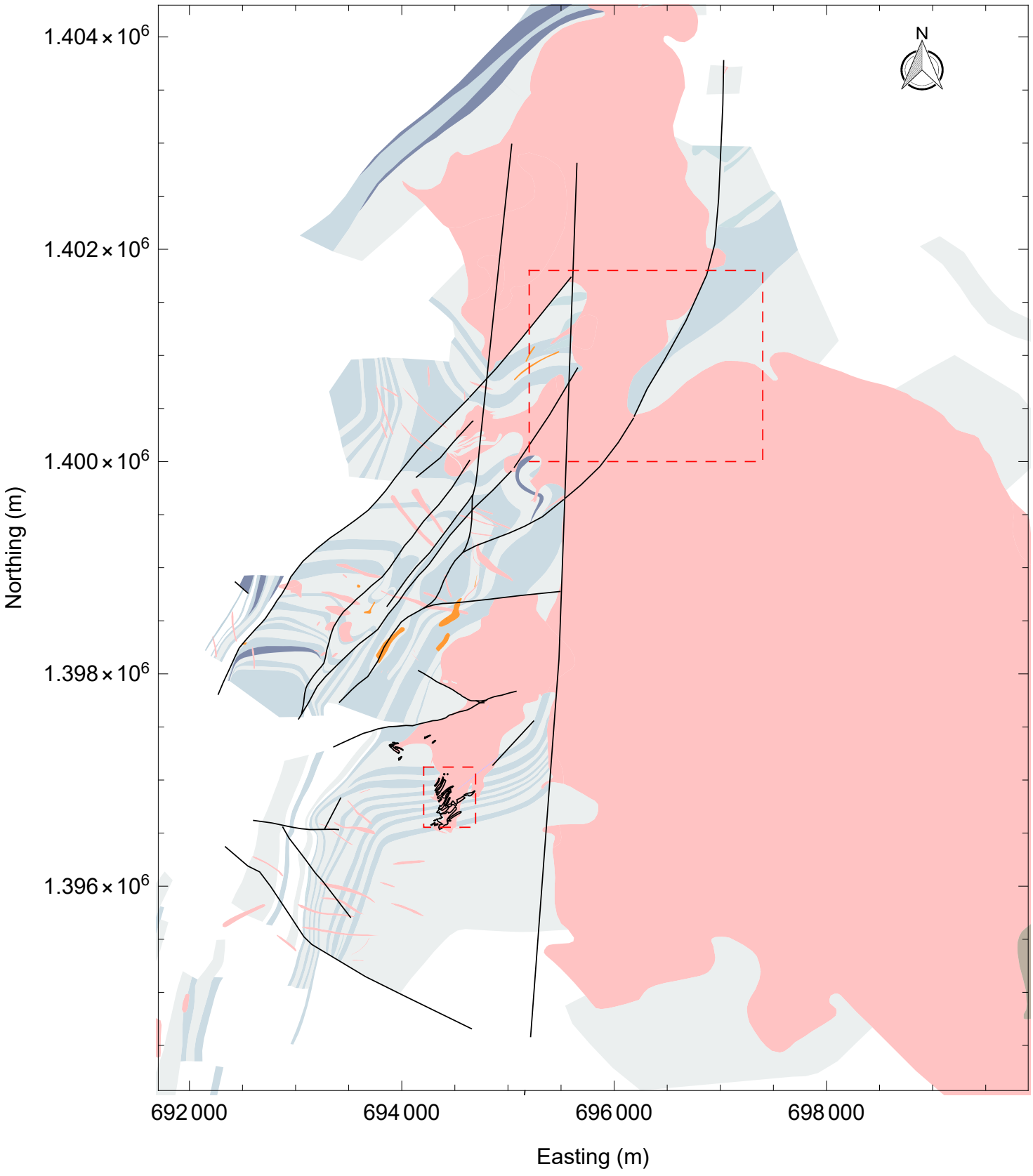

Figure 2.6: Local geological map. The investigations areas are framed by the dashed red lines. The OKvau Project is located within the smaller area in the South. The ORman prospect is the larger zone on the North, surrounding a sedimentary tongue in the intrusion.

Chapter 3

Theory : Electrical properties of the ground

Synopsis

Now that the different kinds of materials have been described, this topic presents an insight into the intrinsic electrical properties of the subsurface in order to understand how rocks react when imposed an electrical field and what parameters control charge transfer. The next chapter will describe the petrophysics of the local material in the light of the explanations below.

3.1 Introduction

The electrical properties of the ground describe how charge is vehicled throughout its constituents. Charge transport might be induced by an applied steady-state or time-varying electric field, generating a steady-state conductivity or a complex admittance or impedance (Glover, 2015). The charge carriers are electrons and/or ions.

Electrons relay charge and allow conduction in conductors and semi-conductors, whereas ions relay charge and allow conduction in the pore fluids, and in the electrical double layer present at the mineral/pore fluid interface.

3.2 Current transmission in the subsurface

3.2.1 Physical relationships

Ohm's law

Ohm's law describes the relationship between the current passing through a material with the potential difference across it (Parasnis, 1962).

In an electrical circuit, the current I, in amperes (A), flowing through a conductor between two points is directly proportional to the potential difference ΔV, in volts (V), and inversely proportional to the resistance R of the material, in ohms (Ω). The Ohm's law is written as

$$I = \frac{\Delta V}{R}. \tag{3.1}$$

The potential difference expresses the electrical force that generates a flow of charge carriers, which are either electrons in the case of electronic conductivity in solid materials, or ions in aqueous solutions. The resistance is the property that resists the passage of the current, and restricts its density proportionally to the electric potential difference (Halliday and Resnick, 2015).

Inside a continuous medium, Ohm's law can be written at any point as

$$\vec{J} = \sigma \vec{E}, \tag{3.2}$$

where

- $\vec{J}$ is the current density in $\mathrm{A \cdot m^{-2}}$,
- σ is the conductivity of the material in $\mathrm{S \cdot m^{-1}}$,
- $\vec{E}$ is the electric field in $\mathrm{V \cdot m^{-1}}$.

The conductivity σ is typically a scalar function that may fluctuate with angular frequency. It can also be a non-linear tensor function of temperature, pressure and deformation, at the same time as being a tensor due to anisotropy (Glover, 2015).

Resistance and resistivity

The resistance R is the aptitude of a substance to impede the flow of an electric current. It relies upon intrinsic property of the material and their geometry, respective to the two ends between which the electric potential is applied. For example, multiplying the length between those two ends by a factor m multiplies the resistance by the same factor. On the other hand, dividing by a factor d the cross-sectional area of material perpendicular to

the current flow direction divides the resistance by the value d (Halliday and Resnick, 2015).

The resistivity ρ does not depend upon the geometry of the sample. It defines exclusively the innate resistive properties of the substance to the stream of charge bearers (Glover, 2015). The resistivity of a material is defined as the resistance between the opposite faces of a unit cube of the substance (Kearey et al., 2002). The SI unit of resistivity is ohm-meters (Ω·m).

For a continuous current transient through a homogeneous and isotropic substance with length L and cross-sectional area A, the resistivity is defined as (Glover, 2015)

$$\rho = R\frac{A}{L}. \tag{3.3}$$

The resistivity of a substance is defined as (Halliday and Resnick, 2015)

$$\rho = R\frac{\vec{E}}{\vec{J}}, \tag{3.4}$$

where $\vec{E}$ is the magnitude of the electric field applied to the substance, and $\vec{J}$ is the magnitude of the resulting current density.

Conductance and conductivity

Conductance G, expressed in siemens (S) is the inverse of resistance. It expresses the aptitude of a substance to let a current passing through it (Glover, 2015)

$$G = \frac{1}{R}. \tag{3.5}$$

Hence, the conductivity σ is the inverse of resistivity

$$\sigma = \frac{1}{\rho}, \tag{3.6}$$

and for a particular substance

$$\sigma = G\frac{\vec{J}}{\vec{E}}. \tag{3.7}$$

3.2.2 Parameters controlling the ionic electrical conductivity

The electrical conductivity of subsurface materials relies upon how current is transmitted through its components. In the upper-crust, the prevailing way through which conduction occurs is by the migration of ions in pore fluids (partially or fully saturating the pore space of the rocks). Therefore, the bulk rock conductivity is controlled by how these pores are

connected (Kearey et al., 2002). The following parameters influence the bulk conductivity (Glover, 2015):

1. **Conductivity of the pore-occupying fluid** The more electrolytes it contains, the more the conductivity will increase. The expression for the electrical conductivity in pore fluid is (Glover, 2015)

$$\sigma_i = \frac{n_i Z_i^2 e^2}{6\pi\eta r}. \tag{3.8}$$

   Equation 3.8 reveals that the electrical conductivity in pore fluids is

   (a) Directly proportional to the number density of charge transporters i available for the transfer of charge n_i.

   (b) Directly proportional to the square of the transported charge $(Z_i e)^2$, where Z_i is the valence of charge carrier i and e is the elementary charge in coulombs.

   (c) Inversely proportional to the radius of hydrated ions r.

   (d) Inversely proportional to the fluid viscosity η (Pa·s).

2. **Material porosity** At the condition that the pores are somewhat connected to allow the transmission of current through their aqueous solution, an increasing porosity (ratio of the void volume to the total volume) will increase the bulk conductivity.

3. **Saturation degree of the pores** Defined as the ratio of the volume of fluid to the volume of void, varying between 0 and 100 %, it is clear that an elevated saturation will favour electric conductivity.

4. **Connectedness of the pores** Even if a material has large and many pores filled with an electrolytic fluid, its bulk conductivity will be negligible if the voids are not connected, so that the charge carriers may not flow through it.

5. **Temperature**; the bulk conductivity of porous rocks saturated to a certain degree by aqueous, conducting fluids increases with rising temperature, at about the rates (Sen and Goode, 1992) :

   - 4 % $°C^{-1}$ at low temperatures (around 5 °C),
   - 2 % $°C^{-1}$ at medium temperatures (around 15 °C),
   - 1 % $°C^{-1}$ as the temperature reaches 100 °C.

The mentioned parameters above will be described in the petrophysics chapter (Chapter 4). Regarding the temperature, it is quite elevated in the OKvau area. Water sampling data in the first 10 m of the subsurface indicated temperature between approximately 26 and 40 °C. This should influence the bulk conductivity and has to be taken into account when interpreting the petrophysics results.

3.2.3 Electronic conduction in rocks and minerals

Most of the crust-forming rocks are poor electronic conductors, as most of the naturally occurring minerals do not generally possess free electrons available to conduct electricity, at the exception of several examples such as metals, graphite, some sulphides... (Telford et al., 1990). A certain distribution of such minerals within a rock can improve its conductivity but it depends greatly on the nature and connectedness of the dissemination (Parasnis, 1962). Typical ranges for some sulphides minerals present within the OKvau deposit are :

Mineral	**$\mathbf{Log_{10}}$ resistivity (Ω·m)**
Pyrrhotite	$-4 \rightarrow -1$
Chalcopyrite	$-4 \rightarrow -1$
Pyrite	$-5 \rightarrow -3$
Arsenopyrite	$-4 \rightarrow -2$

Table 3.1: Typical electronic resistivity values for some sulphides, compiled from Telford et al. (1990) & Parasnis (1962).

3.2.4 Surface conduction and the electrical double layer

A third way through which charge carriers may flow in porous rocks when imposed an external electrical field is the phenomenon called *surface conduction*, occurring in the interfacial region at the junction between the solid grains and the pore fluid (Glover, 2015, Ruffet et al., 1995).

If an ionic solution comes into contact with a mineral having a net charge imbalance (positive or negative), then ions of opposite charge are drawn to its surface exposed in the pore following the electrostatic law. The outcome is an accumulation of anions or cations on the pore walls, referred to as the *double layer* (Ruffet et al., 1995).

Clays for example are commonly known to possess a negative charge, and attract cations close to them, forming a double layer composed of the fixed, negatively charged clay surface, and the adjacent positively charged ions (Ruffet et al., 1995).

This entity provides a new pathway for the transport of charge, generating the phenomenon known as surface conductivity. Is is more pronounced at low pore fluid salinities, where it can provide in this case more conduction than the deficient electrolytic solution, and when there is a substantial amount of clay minerals present, providing a large surface area facilitating surface conduction (Glover, 2015).

Conductivity - summary

The three channels of charge transport described above lead to the following questions :

- How conductive are the phases in the material ?
- How much of each phase is present ?
- What is the degree of connectedness of each phase ?

And ultimately :

- How do the different means of charge transport act together - what is the result on the bulk conductivity of the rock ?

Chapter 4 (Petrophysics) will try to answer these questions.

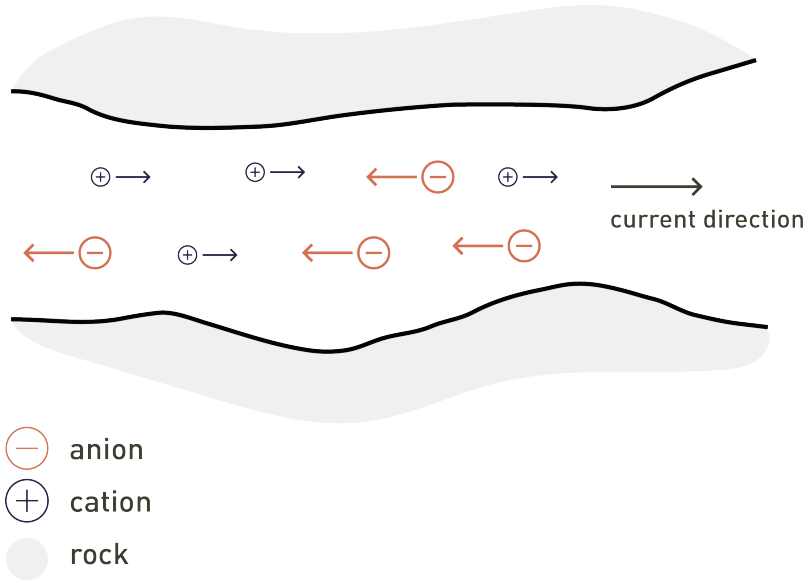

Figure 3.1: Charge transport in an electrolytic solution confined in the pore space of a rock.

3.3 Charge storage in the subsurface

When subject to an electric field, the ground behaves as a capacitor and accumulates electrical charge. This phenomenon causes the subsurface to impede the passage of direct currents, but to conduct alternating currents with increasing effectiveness as the frequency rises. It engenders two effects (Kearey et al., 2002):

1. The transient decay of a residual voltage.
2. The variation of apparent resistivity as a function of frequency.

These effects are consequences of the same event, in the time and frequency domains, respectively. The two are linked by Fourier transformation (Kemna, 2000).

Electrical energy is primarily stored in crust-materials by electrochemical phenomena (Kearey et al., 2002), by two different means: the *membrane polarization* and the *overvoltage effect*.

3.3.1 Membrane polarization

The majority of minerals occurring in the crust possess a net negative charge on their outer areas in junction with the pore fluids, and thus draw cations onto these surfaces (Lowrie, 2007). Depending on the ion concentration and the size of the pore throats, it happens that the extent of the double layer is in the same order of magnitude as the pore network conduits. The passage of ions in the solution is hindered when solicited by an electric field (Kearey et al., 2002; Glover, 2015). The outcome of this results in ions accumulation of opposite charge on each of the side of the obstruction (Lowrie, 2007).

When the enforced voltage is switched off, the charged particles slowly return to their "original" positions, inducing a gradually decaying voltage. This phenomenon is called *membrane polarization* and is observed to a greater extent when clay minerals coat a tight pore network (Kearey et al., 2002; Lowrie, 2007).

3.3.2 Overvoltage effect

If conductive minerals occur in a rock, an electronic pathway becomes accessible for the current flow. When such particles are disseminated into the rock matrix characterized by a certain porosity, saturation and connectedness, some conductive mineral grains happen to communicate with the pore network (Kearey et al., 2002; Lowrie, 2007).

When a voltage is imposed to either sides of the particles, negative and positive charges appear on each side of the grains. Ions are then drawn to the mineral side corresponding to their opposite charge, and are compelled to either release electrons to the grain, or gain electrons conducted through it. There is a discrepancy between the rate at which the charge carriers are conducted and the rate at which they are exchanged with the ions. Therefore, ions build-up occur on both sides of the grains and provoke an accumulation of charge (Kearey et al., 2002; Lowrie, 2007).

As the imposed voltage is switched off, similarly to the membrane polarization effect, the ions gradually diffuse back into the solution, generating a transient decaying voltage. This phenomenon is called *electrode polarization* or *overvoltage*. It is facilitated by an elevated degree of conductive mineral dissemination in the rock, since the area available for charge exchange would be optimized. It is also favored by a tight pore network, effectively restricting the number of ionic conduction pathways (Kearey et al., 2002).

When prospecting for sulphidic ores, the phenomenon of interest is evidently the overvoltage effect.

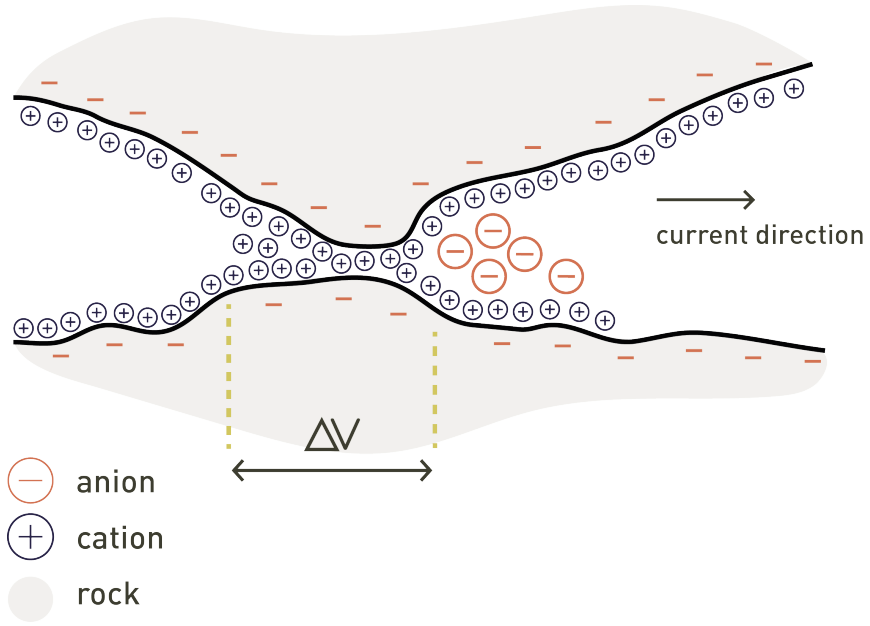

Figure 3.2: Membrane polarization phenomenon.

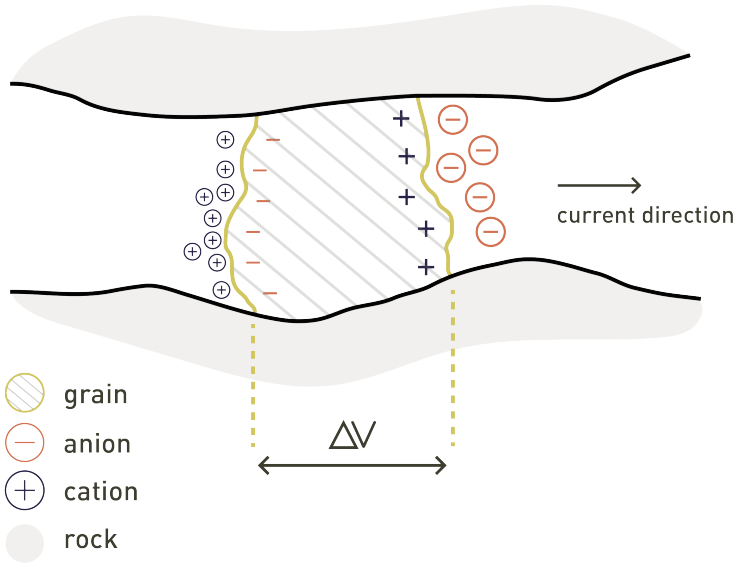

Figure 3.3: Overvoltage effect phenomenon.

3.3.3 Mathematical formulation of chargeability

Seigel (1959) proposed a mathematical formulation for the overvoltage phenomena. Considering the previously defined polarization effect, the operation of imposing an electric field to a three-dimensional body containing a finite volume density of dipolar sources, is to generate a volume distribution of current dipoles perpendicular to the field at each point in the medium. The volume current moment strength is then

$$\vec{M} = -m\vec{J}, \tag{3.9}$$

where $\vec{J}$ is the primary (imposed) current density. The scalar m is supposed to be a constant named *chargeability*. It is a characteristic of the medium and englobes all polarization phenomena (Seigel, 1959). However, it hinges on the length of action of the applied voltage.

Seigel (1959) demonstrated that in the presence of polarizable sources, the ultimate effect of chargeability is to reduce the effective conductivity σ of the medium by a factor $(1 - m)$. Thus, if the original imposed current density vector is $\vec{J} = \sigma\vec{E}$, then it becomes equal to $\sigma(1 - m)\vec{E}$ in the presence of dipoles.

The above conclusions are of uttermost importance in chargeability forward modeling and inversion.

Chapter 4

Petrophysics

Synopsis

This chapter describes petrophysics results obtained from rocks in the OKvau Project area, which will hopefully help recognizing the resistivity and IP signals of this study.

Summary

The following table summarizes the mesoscale petrophysics study data realized in the early phase of development by Systems Exploration (NSW) Pty Limited. (2008), for 14 drill core samples of diorite and hornfelsed sediments.

Category	**Minerals**	**WBD**	**Mag k**	**EM res.**	**R_{sat}**	**IP**
Units	-	g/cm^3	SI×10^{-5}	Ω.m	Ω.m	ms
Sediments						
Hornfels	As, Py, Po, banded	3.11	850	4.7×10^{-4}	4056	38
Altered Diorites						
Veined	As, Py, Po	3.55	92	0.2	3108	65
Veined	As, Py, **PO**	3.18	1438	1.7×10^{-3}	5638	128
Semi/Massive	As, Py, Po	5.29	23	0.083	0.1	194
Semi/Massive	As, Py, Cpy, **PO**	3.98	7601	1.9×10^{-4}	≈0.002	285

Table 4.1: Summary - Average values of inductive and galvanic properties.

Notation	Signification
Units	
WBD	Wet (saturated) Bulk Density
Mag k	Magnetic susceptibility
EM res.	Electromagnetic resistivity
R_{sat}	Galvanic resistivity in saturated state at 1kHz
IP	Induced polarization effect as equivalent chargeability
Minerals	
As	Arsenopyrite
Po	Pyrrhotite in minor concentration
PO	Pyrrhotite in major concentration
Py	Pyrite
Cpy	Chalcopyrite

Table 4.2: Notations for the petrophysics study.

Porosity and density

- The apparent porosities (water accessible voids volume with respect to total volume) are usually very low, but increasing when fractures are present. The densities range from moderate to high, generally rising with the arsenopyrite/pyrite content (Figure 4.1).

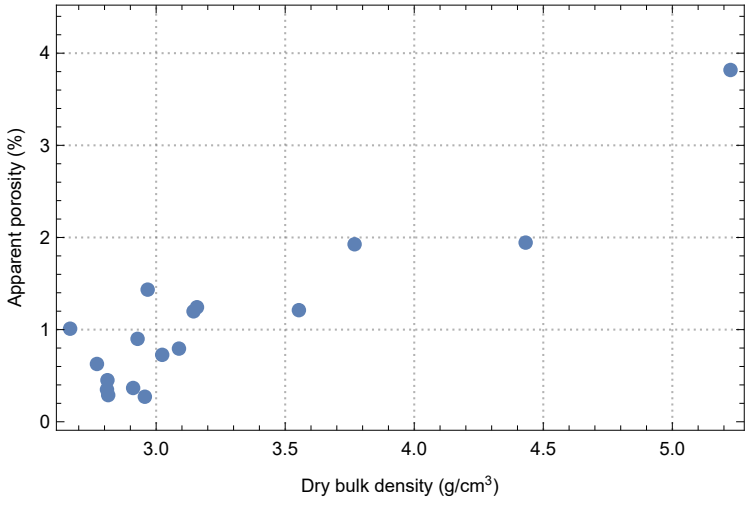

Figure 4.1: Apparent porosity versus dry bulk density.

Resistivity

- The saturated resistivities are very elevated at the exception of the altered diorites with semi/massive sulphides (see Table 4.1). Those are relatively low compared to the dry samples. In reality, this parameter will vary between those two extremes (wet/dry) according to the saturation state of the rocks. Furthermore, the study doesn't take into account the presence of fractures and other structures that would likely increase the conductivity on a macro-scale.

- The induced and galvanic resistivities can not be compared, due to the texture, aside from samples where semi/massive sulphide concentrations exist.

Induced polarization

- The induced polarization responses seem to indicate that well distributed pyrrhotite produces a greater effect than banded or semi/massive pyrrhotite bearing sulphides, which in turn seem more responsive than the sulphides poorer in pyrrhotite (Figure 4.2).

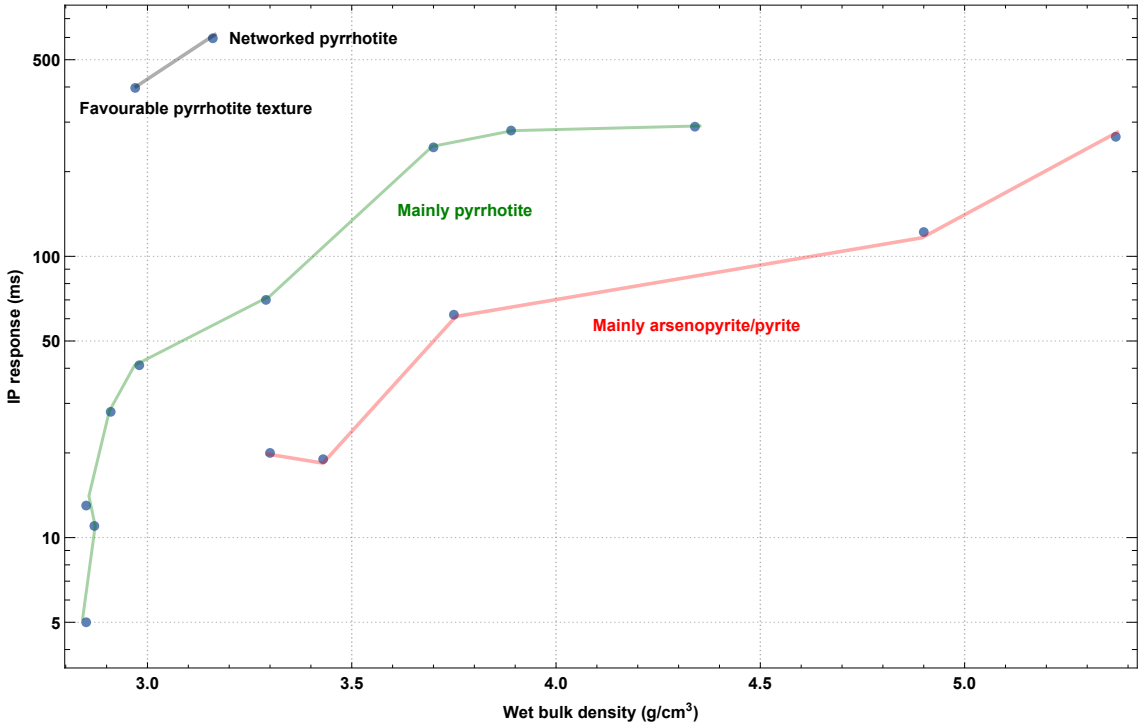

Figure 4.2: IP response versus wet bulk density.

- The induced polarization responses plotted in a log-log scale versus the galvanic resistivities in saturated state (Figure 4.3) show that promising zones in terms of sulphides mineralization exhibit an elevated IP response associated to a relatively low resistivity, in fractured zones or in case of well connected mineralization network (sample 13, Figure 4.3). On the other hand, more resistive materials present a lower IP response and there is a wide gap almost covering four orders of magnitude in terms of resistivity separating high/low IP responses.

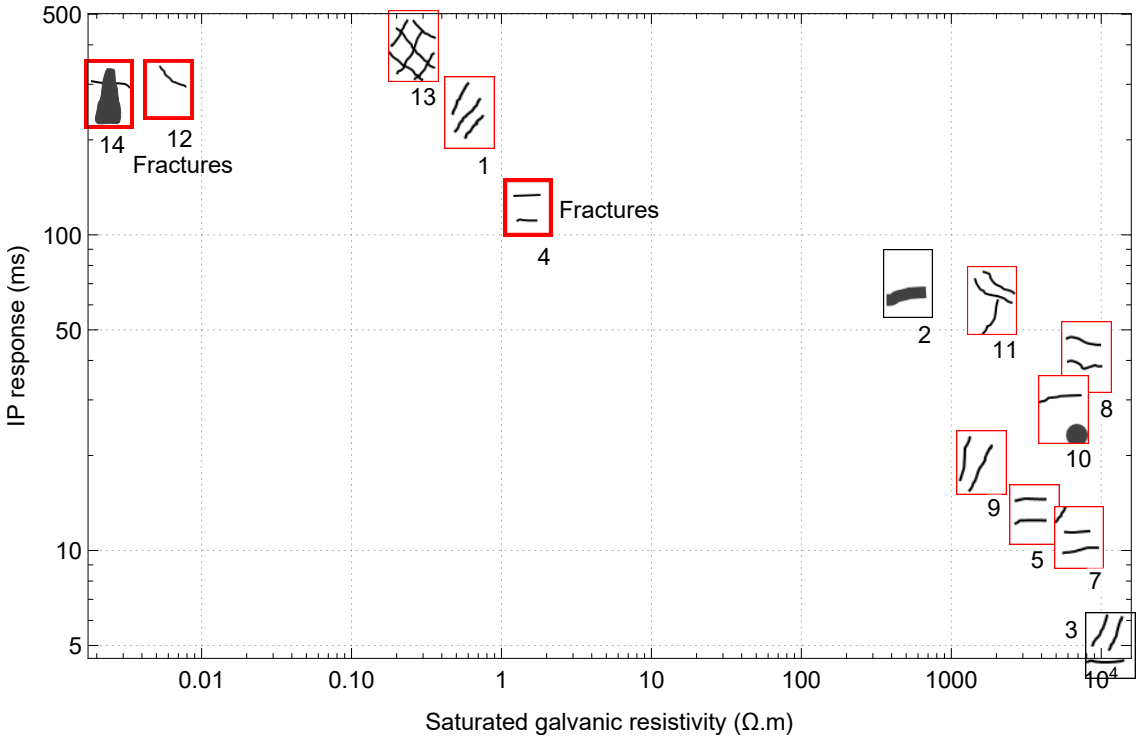

Figure 4.3: IP response versus saturated resistivity. The plot markers are illustrations of the general texture of each sample. The red frames indicate a diorite sample and a gray frame a sedimentary one. Thick borders correspond to semi/massive sulphide mineralizations whereas a thin border represents veined/banded mineralizations.

Magnetic susceptibility

- The magnetic susceptibility appears to be controlled by the pyrrhotite concentration, which also seems linked to the inductive (EM) conductivity. The plot representing the galvanic saturated resistivity versus the magnetic susceptibility is similar to Figure 4.3, which may indicate a correlation between chargeability and magnetic susceptibility, although there are not enough samples to confirm this.

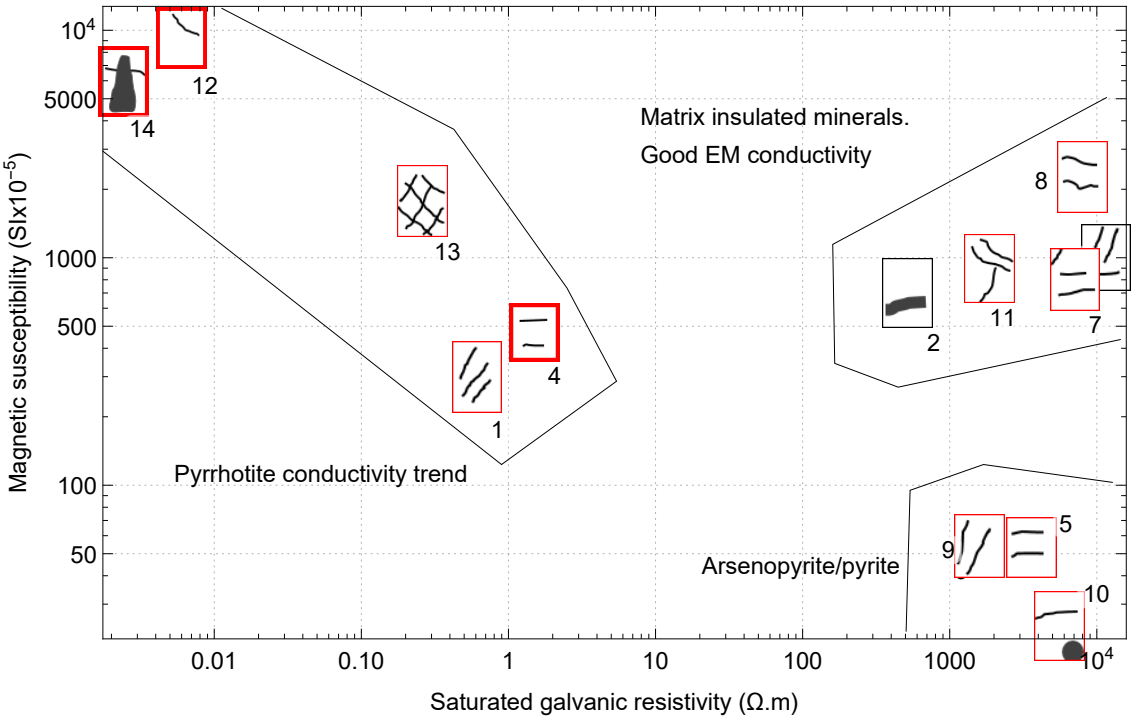

Figure 4.4: Magnetic susceptibility versus saturated resistivity. The plot markers are illustrations of the general texture of each sample. The red frames indicate a diorite sample and a gray frame a sedimentary one. Thick borders correspond to semi/massive sulphide mineralizations whereas a thin border represents veined/banded mineralizations.

Discussion

If the petrophysics are considered representative on a macro-scale of the bulk properties of the entire deposit, it can help in recognizing anomalies on the IP profiles. It appears that the main IP signals are dominated by massive sulphides and well connected pyrrhotite mineralization, in altered, low-resistivity diorites.

From this study, it would seem that the rocks at OKvau have a poor porosity, with an associated low conductivity, except in the case of fracturation/mineralizations. However, it doesn't take into account the possible faults/fractures in the subsurface, nor the pression and temperature conditions, which may influence the electrical properties of the underground, with most of the samples being extracted from depth superior to a hundred meters.

Chapter 5

Theory : Electrical methods

Synopsis

Before presenting the survey design in the next chapter, the general theory behind the data acquisition in resistivity/IP investigation and the sources of errors are explained.

5.1 Introduction

Electrical methods are field investigative techniques used for characterizing electrical properties of the subsurface. More specifically, they are used to define low frequency (< 1 kHz) resistive and capacitive properties. The methods used in the aim of this work belong to the *active* methods family, based on the injection of a direct current into the ground (Binley, 2015). Passive source electrical method (self-potential) was not considered.

5.2 Measurement principles

5.2.1 DC resistivity

Current flow in a homogeneous ground

The basic approach to determine the resistivity of the subsurface involves injecting current between two electrodes acting as a point source/sink, and measuring the voltage difference between two other electrodes (Binley, 2015; Loke, 1999).

For a 3-D isotropic resistivity distribution $\rho(x)$, the electrical potential $V(x)$, due to a single point current electrode at a point at distance x, with I coulombs per second, is given by the Poisson equation

$$\nabla \cdot (\frac{1}{\rho}\nabla V) = -I\delta(x), \tag{5.1}$$

where $\nabla = \frac{\partial}{\partial x} + \frac{\partial}{\partial y} + \frac{\partial}{\partial z}$ is the gradient operator and δ is the Dirac delta function. Equation (5.1) is subject to the boundary condition

$$\frac{1}{\rho}\frac{\partial V}{\partial n} + \beta V = 0, \tag{5.2}$$

where n is the outward normal and β defines the type of boundary condition ($\beta = 0$: Neumann; $\beta \neq 0$: mixed) (Binley, 2015; Kemna, 2000; Oldenburg and Li, 1994).

Let $\mathcal{S}$ be a surface of uniform conductivity in which a current is injected between two electrodes positioned on its upper edge, one of which being far away from $\mathcal{S}$, acting as an infinite electrode. Assuming the current sink positioned infinitely far, the voltage at some distance r from the current source resulting from (5.1) is given by (Binley, 2015; Kearey et al., 2002)

$$V = \frac{I\rho}{2\pi r}. \tag{5.3}$$

The current electrode configuration is referred to as a dipole, and the potential electrode pair as a measurement dipole. Let (**A**, **B**) be the dipole and (**M**, **N**) the measurement dipole. Using equation (5.3), applying the superposition method, an expression for the voltage at any point can be written as

$$\Delta V = \frac{I\rho_a}{2\pi r}\left[d(A,M)^{-1} - d(B,M)^{-1} - d(A,N)^{-1} + d(B,N)^{-1}\right], \tag{5.4}$$

where ρ_a designates the apparent resistivity and the function d is simply the Euclidean distance between two specified points. In terms of resistivity:

$$\rho_a = k\frac{\Delta V}{I}, \tag{5.5}$$

where k is defined as the geometric factor

$$k = 2\pi\left[\frac{1}{d(A,M)} - \frac{1}{d(B,M)} - \frac{1}{d(A,N)} + \frac{1}{d(B,N)}\right]^{-1}. \tag{5.6}$$

The apparent resistivity, labelled as ρ_a and expressed by (5.5), is the value that is apparent from the measurement. This value would be the true resistivity of the subsurface for a

homogeneous flat earth (which is far from reality). In order to estimate the "true" resistivity structure of the ground, inverse methods must be applied to the apparent resistivities (Loke, 1999). Those methods will be presented in Chapter 8.

5.2.2 Induced polarization

As stated in section 3.3, the ground can act as a capacitor and store electric charge as an external current is applied to it. When the imposed voltage is switched off, the measured voltage does not fall immediately to zero. It first drops to an intermediate voltage and then gradually decays. The measure of this voltage gradient over time allows to reveal the polarization characteristics of the subsurface. Practically speaking, it is possible to measure the IP effect both in time-domain and in the frequency domain. But in the aim of this work, the time-domain technique was used and shall further be described. Spectral IP measurements consist in measuring the variations in apparent resistivity values from low to high frequencies (in the order of 1 to 10 Hz), or by measuring the phase shift between the voltage signal and the input voltage, to deduce the IP effect. More information on spectral IP can be found in Kemna (2000), Kemna et al. (2012), Binley (2015).

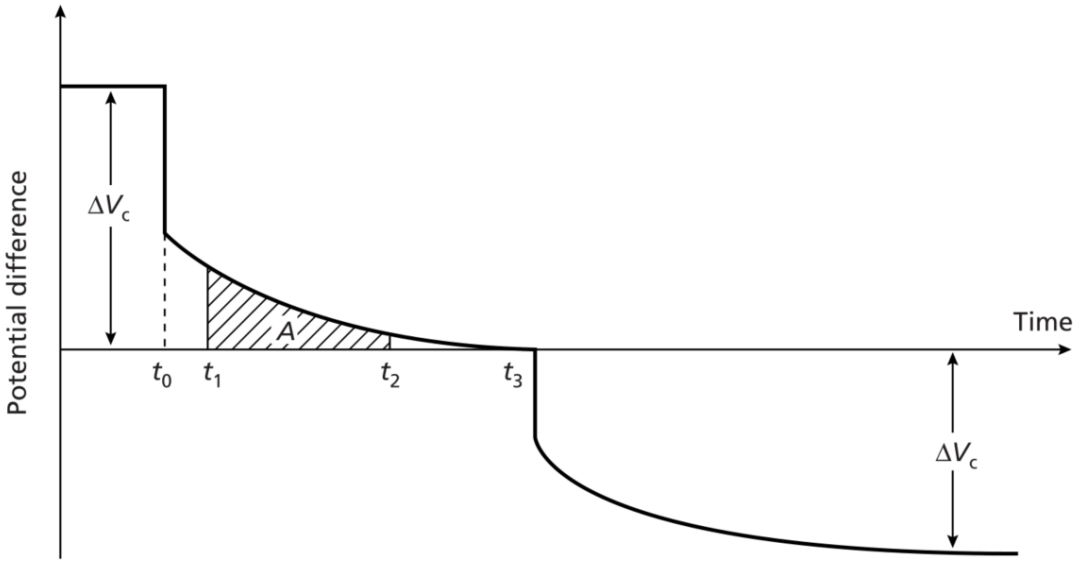

Figure 5.1: Expression of the phenomenon of induced polarization in time-domain. The primary voltage difference ΔV_c is switched off at the time t_0. After an initial relatively strong fall, the measured potential difference in the ordinate-axis gradually decays over time. At time t_3, a similar sequence is realized with opposite voltage $-\Delta V_c$ to avoid polarization of the electrodes. A represents the area below the curve between t_1 and t_2 (Kearey et al., 2002).

A common measure of the IP effect in time-domain is the *integral chargeability* M_a :

$$M_a = \frac{1}{t_2 - t_1} \frac{1}{V_c} \int_{t_1}^{t_2} V(t) dt, \tag{5.7}$$

where t_1 to t_2 is the time interval over which the measurement is performed. Observing (5.7), it appears that M_a is dimensionless. However, it is often expressed for convention as millivolts per volts (mV/V) or in milliseconds (ms).

Practically, (5.7) is integrated by means of sampling the potential at discrete times (usually 10 to 20) over the user-defined time interval $[t_1\ t_2]$. Those values are user-implemented within the measure instrument (Binley, 2015).

IP investigations are more time costing than classic DC surveys, because they generally require injecting a current with much greater input (since the overvoltage effect has a much lower magnitude than the primary voltage), and more stacking of measurements. The choice of the electrode configuration should take this parameter into account, and a multichannel-compatible array can be chosen in order to optimize the speed of the investigation (Binley, 2015).

5.2.3 Measurement errors

Electric investigations can be affected by several sources of noise and errors. Here is a non-exhaustive list englobing the main sources of noise. For more details, see Sumner (1976).

- **Telluric noise.** Low-amplitude and gently evolving currents flow continuously through the Earth (Sumner, 1976). Their direction may vary but is typically parallel to the ground surface. However, their effects are easily suppressed when using alternating current, which cancels their effects. Indeed, at each direction change of current, the telluric current alternately increments or decrements the measured potential difference by identical magnitude; summing the output over various cycles removes the detrimental effect (Kearey et al., 2002).

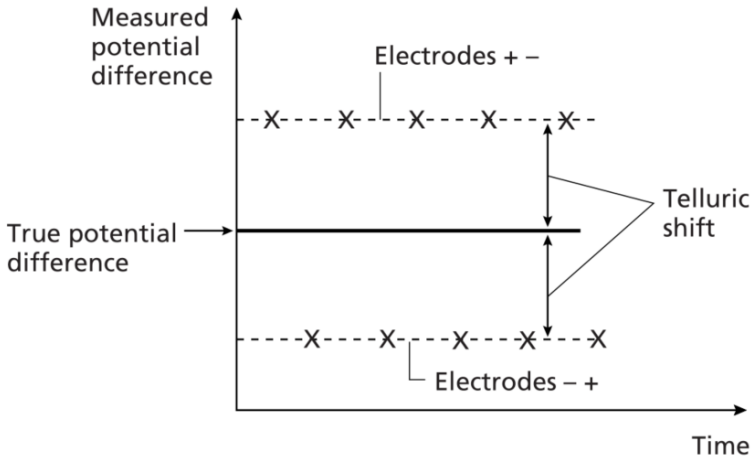

Figure 5.2: Illustration of the telluric current effect and its suppression by the use of alternating current (Kearey et al., 2002).

- **Man-made electrical noise.** Luckily, hardly any man-made electrical instruments operate in the IP frequency band of interest (Sumner, 1976). Utilizing filters to diminish undesirable noise is an appropriate way of augmenting the signal to noise ratio of the IP receiver. For example, low-pass filtering may be used to reject power-line frequencies and radio station interference, at the threshold of 10 Hz, since there are usually no IP frequencies of interest above that value.

- **Sferics.** They are electrical phenomena originating from the atmosphere. They essentially consist of electromagnetic pulses due to thunder bolts. Their frequency band is normally higher than that of the IP, but can be troublesome. If the data become affected by this event, a thunderstorm could be too close (Sumner, 1976). This somewhat anecdotal source of noise is only mentioned here because thunderstorms forced the crew to flee the field at several occasions during the investigations of this study. Although, detrimental aspects of sferics have not been observed on the data, or its aspects could not have been differentiated from other sources.

- **Self-potential noise.** Self-potential voltages results from electrochemical reactions within the subsurface, in the neighbourhood of the profile. They typically have very low amplitudes and are incoherent in their frequencies (Sumner, 1976).

- **Contact resistance.** As mentioned in subsubsection 2.2.3 and subsubsection 5.3, the contact resistance between the ground and the electrodes can lead to bad readings. However, the measure instrument compute those resistance beforehand, allowing the user to improve this issue, for example by hammering the electrodes deeper and/or

by adding some electrolytic fluid in a relatively small zone around the concerned electrodes (Binley, 2015).

- **Measured potentials magnitude.** During the data acquisition, it is important to check if the measured voltages are high enough, i.e. not too close to the instrument resolution. This can occur in practice when the input voltage is too weak and/or when associated with big geometric factors. This can be problematic in IP investigations where a secondary, decaying voltage is measured, whose magnitude is largely below the primary voltage. This is why the input current needs to be more intense and applied longer (a few seconds) than a DC survey (Binley, 2015).

- **Electrode polarization.** Already mentioned in subsubsection 5.3, this phenomenon can lead to spurious readings in IP investigations when intense current is injected for a prolonged time. An ingenuous attempt to reduce electrode polarization is to regularly switch the polarity of the current electrodes (Binley, 2015).

- **Coupling of electrical circuits.** This phenomenon can cause errors during IP investigations, it refers to the resistive and capacitive coupling between an IP transmitter and receiver (Sumner, 1976). The capacitive coupling is a voltage variation owing to:

  – Electrical leakage from transmitter or receiver electrodes to receiver or transmitter wires. This effect can change the charge distributions stirring capacitance.
  – Displacement currents from wire to wire or wire to the ground.

  To lessen capacitive coupling, the receiver and transmitter should be at a sufficiently large distance between each other (Sumner, 1976). This is why the Dipole-Dipole configuration has originally been favored, due to the large distance between the transmitter and receiver (Binley, 2015).

- **Cultural coupling effect.** This detrimental effect appears when a man-made metallic (conductive) object is in the neighbourhood of the electrode layout. It can lead into spurious IP anomalies readings, mainly due to leakage currents between the transmitter and receiver circuits. If detected, some ways to overcome the effects are to somehow insulate the object, by using lower frequencies or simply removing it if possible (Sumner, 1976).

- **Electromagnetic coupling.** In some circumstances, the IP transmitter and receiver act like the primary and secondary coil windings of an usual electrical transformer - the primary circuit induces a current in the secondary circuit, phenomenon aggravating with higher frequencies (Sumner, 1976). This electromagnetic induction provokes deceptive IP-similar effects. The effect is more pronounced in conductive environments and long-array geometries chosen to investigate deeper bodies, but is more

bothersome in frequency-domain acquisition, where Routh and Oldenburg (2001) propose ways to remove the detrimental effects.

The quality of resistivity and induced polarization data is usually assessed through repeatability, i.e. by estimating the variability of signals from multiple injected cycles (Binley, 1995). Although these are helpful and immediate *in the field* hints on data quality, the origin of noise can be random and could be repeated. Another interesting and quantitative measure of data quality is *reciprocity* - measurements realized after inverting transmitter and receiver pair should be equal. A constraint of this method is the time factor, since it doubles the tasks to realize (Binley, 2015).

5.3 Measurement practicalities

Measurement from the ground surface

Usually, for ground-based near-surface investigations, electrodes are stainless steel, non-polarizing rods, typically 1 cm in diameter and 30 cm long, hammered into the ground to 10 cm or so. The stainless steel is supposed to prevent the corrosion of the electrodes and electrode polarization effect. Indeed, chemical reactions on the potential electrodes can lead to electrochemical signals that could influence the readings (Binley, 2015). Furthermore, the contact between the stakes and the ground has to be optimal in order to transmit the current. If a coating such as rust existed at the electrodes surface, the contact resistance with the soil would be compromised (Zonge and Hughes, 1985). A successful attempt to oppose electrode polarization is to regularly switch the polarity of the current electrodes A and B. It is important in IP investigation, when current is injected for a relatively long time in the ground (Binley, 2015).

Various electrodes geometries exist (Loke, 1999; Loke et al., 2013), that is, there are several ways to position the electrodes in order to inject current and measure potentials. This affects the parameter k in (5.6) and thus influences the potential readings. The different geometries have assets and detriments, and the selection of an optimal configuration must be based on the intended application and expected signal strength. Some parameters to consider while making that choice are (Binley, 2015; Loke, 1999):

- The **sensitivity**, defined in the case of resistivity measurements as

$$\frac{\partial \Delta V}{\partial R}. \tag{5.8}$$

  It is basically a measure of *how* the measured voltage differences are sensitive to variations in resistance of the subsurface. Obviously, the more sensitive is a configuration, the more interesting it becomes. However, the sensitivity distribution varies

from configuration to configuration. For example, some are better at detecting lateral or vertical variations in resistivity.

- The **depth of investigation (DOI)**, which represents the deepest level at which a measure can be made. It depends on the longest distance between electrodes, and is basically the 1-dimensional horizontal median of the sensitivity values.
- The **signal strength** or signal-to-noise ratio (S/N), depends on the spacing between the transmitters and the receivers. A large spacing can result in weak voltage gradients at the measurement dipole location, and stronger signals are related to shorter spacings.

5.3.1 Electrodes configurations

Some commonly used electrode array configuration include:

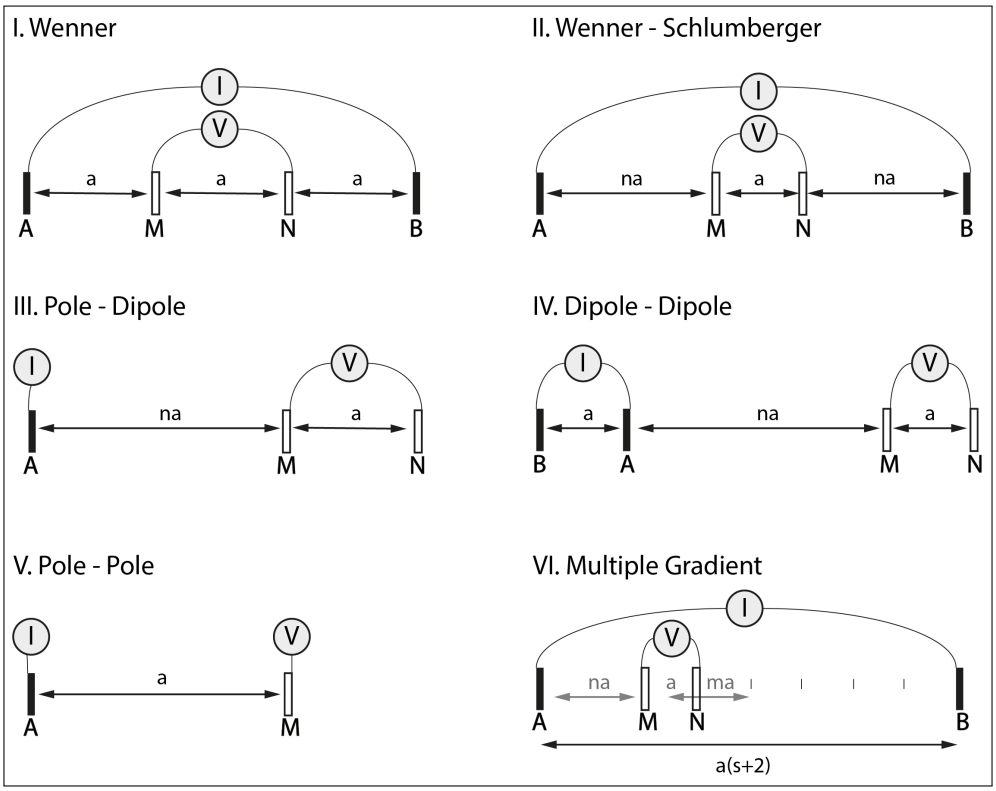

Figure 5.3: Some commonly used electrode configuration arrays. a is the distance between electrodes, and the factors m, n and s are scalars. Combined from Loke (1999) and Dahlin and Zhou (2006).

A short summary of each mentioned configuration in Figure 5.3 will be realized, regarding the three parameters (sensitivity, DOI, S/N) in order to explain and understand the choice for this study, as well as to get a grasp on what is at stake when choosing a particular array.

I. Wenner Array

- **Comment.** Robust and traditional array.
- **Sensitivity.** This array is more sensitive to vertical variations in the subsurface. As it can be seen on Figure 5.4, the contours are aligned horizontally. Obviously, it is weaker in detecting horizontal gradients.

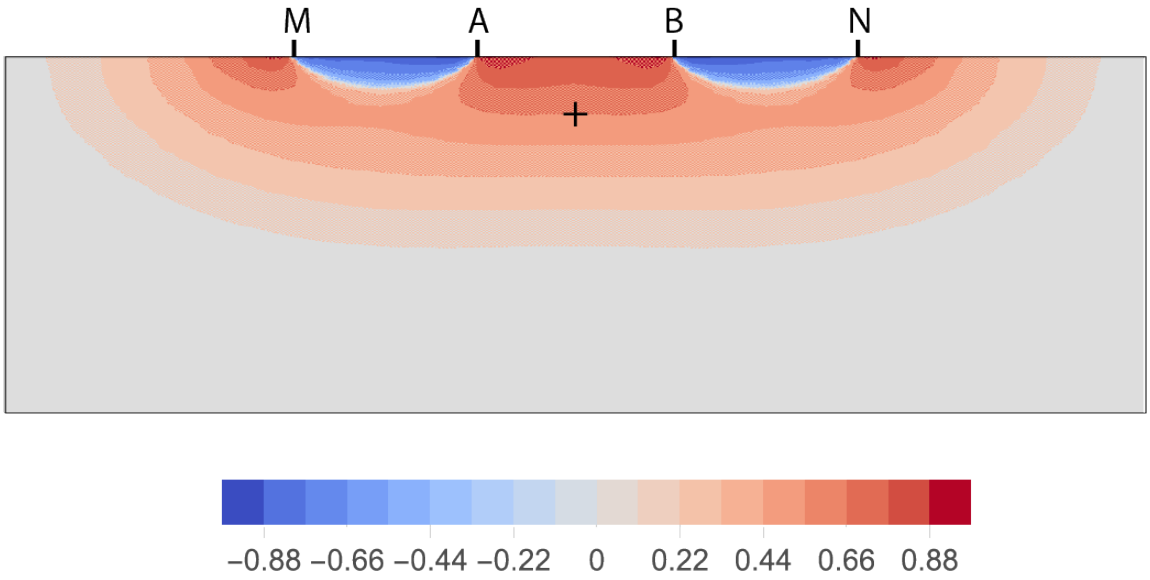

Figure 5.4: Wenner Array sensitivity plot scaled from -1 to 1 on homogeneous ground. Array parameters : $a = 1$ m. Modified from Loke (1999).

- **DOI.** The median depth of investigation is about $a/2$, where a is the electrode spacing. It thus has a moderate DOI compared to other configurations.
- **S/N.** This ratio is inversely proportional to the geometric factor k, and the Wenner array has one of the smallest value among the different arrays ($2\pi a$), conferring it the highest signal strength.

II. Wenner-Schlumberger Array

- **Comment.** Hybrid between the Wenner and Schlumberger array (not described here).
- **Sensitivity.** Compared to the Wenner array sensitivity figure, there is a slim vertical curvature beneath the middle of the array, and lower sensitivity values in the zones between M and A, and symmetrically, B and N. According to the n factor, the configuration will be moderately sensitive to horizontal (low n) and vertical (higher n) variations.

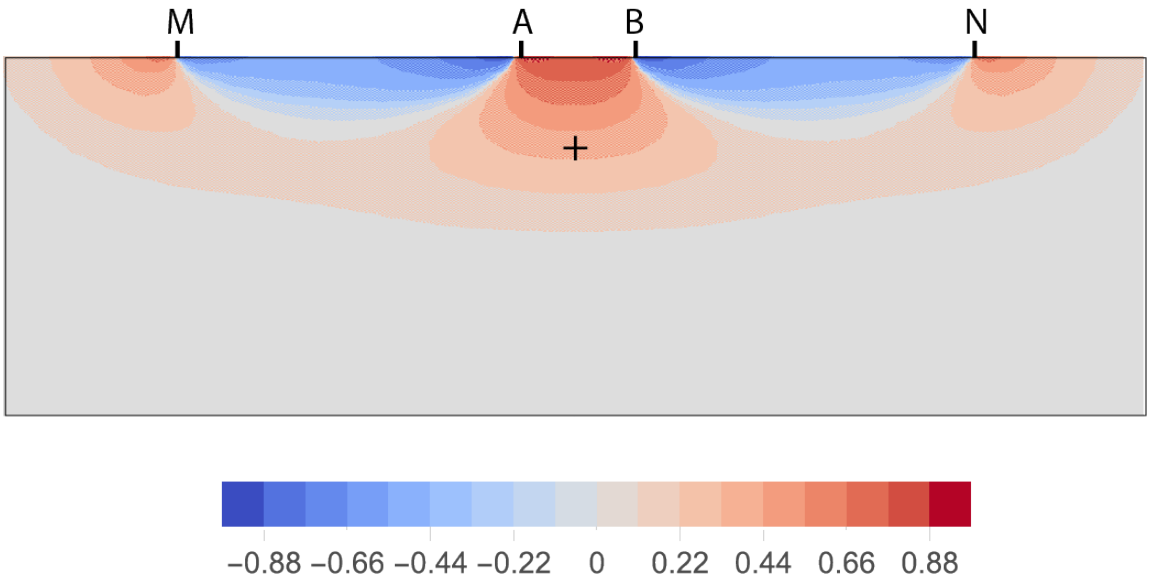

Figure 5.5: Wenner-Schlumberger Array sensitivity plot scaled from -1 to 1 on homogeneous ground. Array parameters : $a = 1$ m and $n = 3$. Modified from Loke (1999).

- **DOI.** The median DOI is about 10 % deeper than for the Wenner array, for an equal distance between electrodes A and B.
- **S/N.** The S/N ratio is smaller than for the Wenner array, but better than the Dipole-Dipole array.

III. Pole-Dipole Array

- **Comment.** Appealing alternate option for IP investigations, compared to the Dipole-Dipole array (increased signal strength) and to the Wenner/Wenner-Schlumberger arrays (lower electromagnetic coupling).
- **Sensitivity.** The best sensitivity values lie below the potential electrodes M and N. For an increasing n factor, the elevated sensitivity zone below the potential electrodes becomes more and more aligned with the vertical axis, it becomes adequate for detecting vertical gradients.

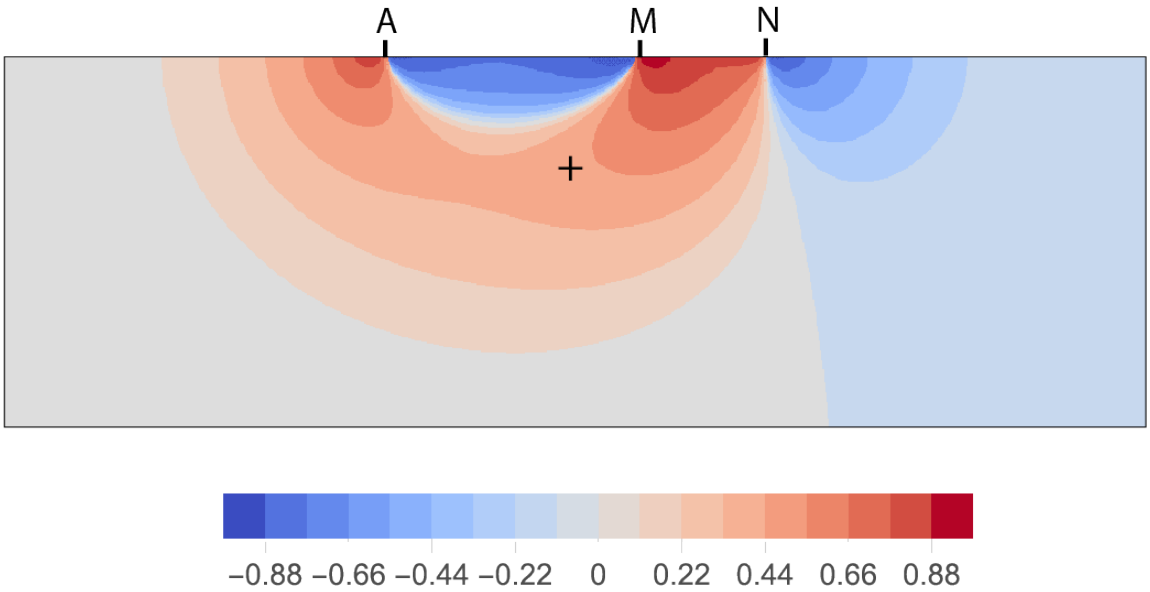

Figure 5.6: Pole-Dipole Array sensitivity plot scaled from -1 to 1 on homogeneous ground. $n = 2$. Modified from Loke (2015).

- **DOI.** It goes slightly deeper than the Dipole-Dipole array, and it is possible to increase it by augmenting the parameter a.
- **S/N.** It has a substantially bigger S/N ratio than that of the Dipole-Dipole array, and is not as susceptible to pick telluric noise as the Pole-Pole array.

IV. Dipole-Dipole Array

- **Comment.** Extensively used in resistivity and IP investigations on account of the small electromagnetic coupling between the circuits.
- **Sensitivity.** The zones containing best sensitivities are located beneath the two electrodes couples (Figure 5.7). The two lodes formed by these high sensitivities converge towards the middle of the array. The contour patterns tend come closer to verticality as the factor n increases. It results in a highly adequate configuration for picking horizontal resistivity gradients in the subsurface. As a trade-off, its capacity to detect vertical gradient is weaker.

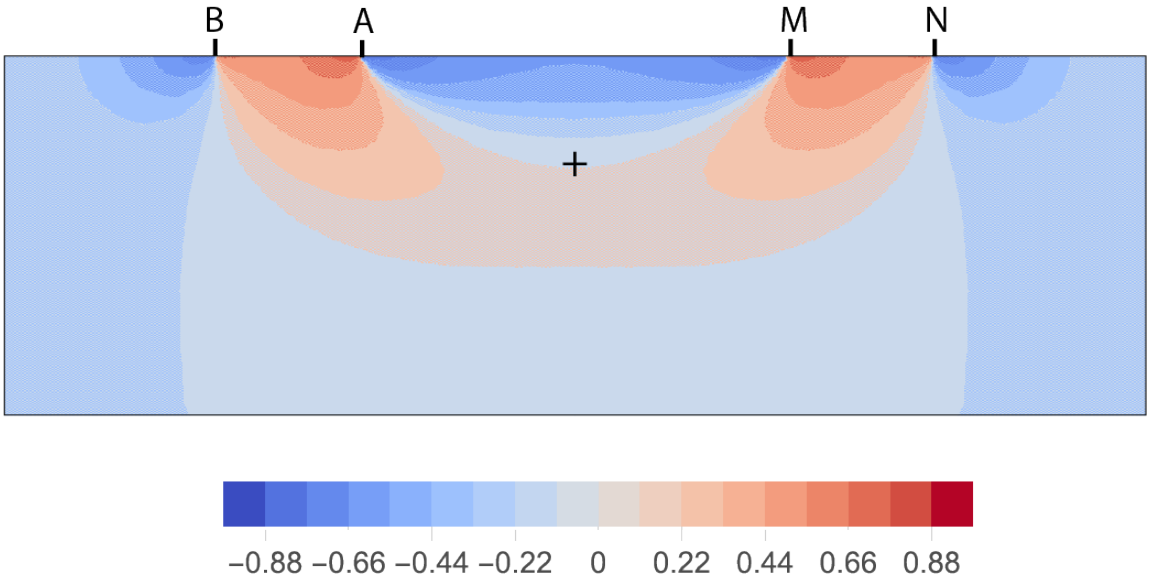

Figure 5.7: Dipole-Dipole array sensitivity plot scaled from -1 to 1 on homogeneous ground. Array parameters : $a = 1$ m and $n = 3$. Modified from Loke (1999).

- **DOI.** Its penetration depth depends on the n factor. It usually has a lower DOI compared to the Wenner array.
- **S/N.** A particular weakness of this configuration is the terrible signal strength for large n factor values, since the potential and current couples are then so far from each other.

V. Pole-Pole Array

- **Comment.** Prominent in specific applications such as archaeological investigations, where relatively short electrode spacings are used.
- **Sensitivity.** The large spacings between the contours of the 2D sensitivity plot indicate that this method has a poor resolution.

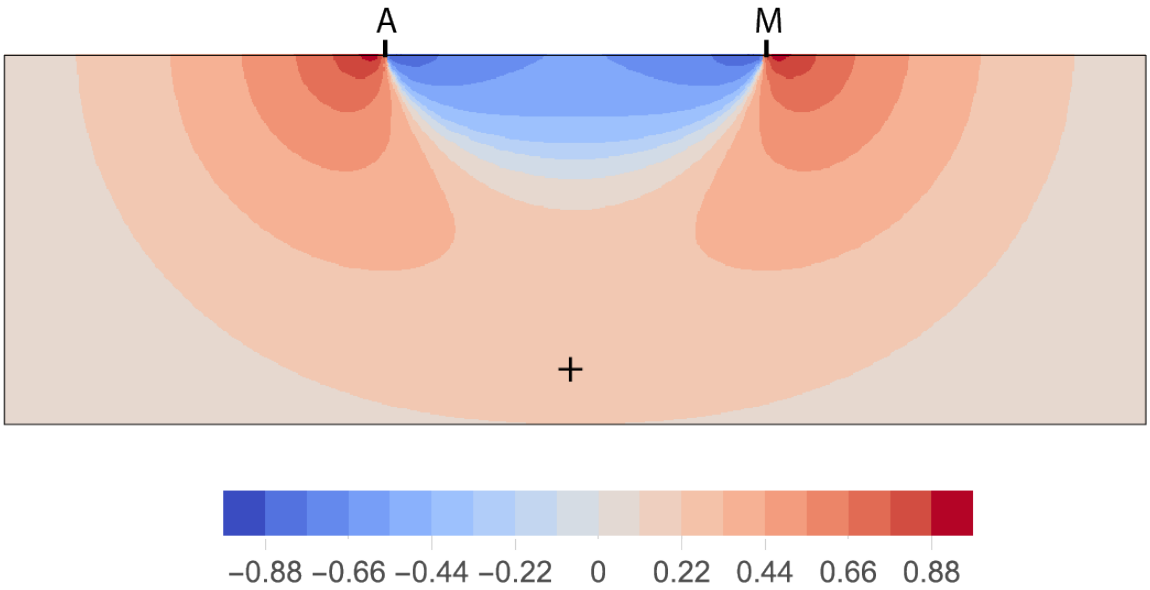

Figure 5.8: Pole-Pole array sensitivity plot scaled from -1 to 1 on homogeneous ground. Modified from Loke (2015).

- **DOI.** It has the deepest depth of investigation of all the arrays.
- **S/N.** The second current and potential electrodes B and M are actually located at great distance from A and M. Because of this considerable separation, this configuration is susceptible to collect generous amounts of telluric noise, altering the data quality.

VI. Multiple Gradient Array

- **Comment.** Designed in 2006 by Dahlin and Zhou. Several series of voltage gradient measures are realized with the current electrodes at diverse points. It can be envisioned as englobing the attributes of the Pole-Dipole and the Wenner-Schlumberger.
- **Sensitivity.** For fixed A and B potential electrodes, and moving potential electrodes M and N, the sensitivity pattern will evolve from a Wenner-Schlumberger array type for M, N far from A and B, to a Pole-Dipole array type when the potential couple comes close to either A or B. Figure 5.9 is an intermediate between those two situations, when M and N approach B.

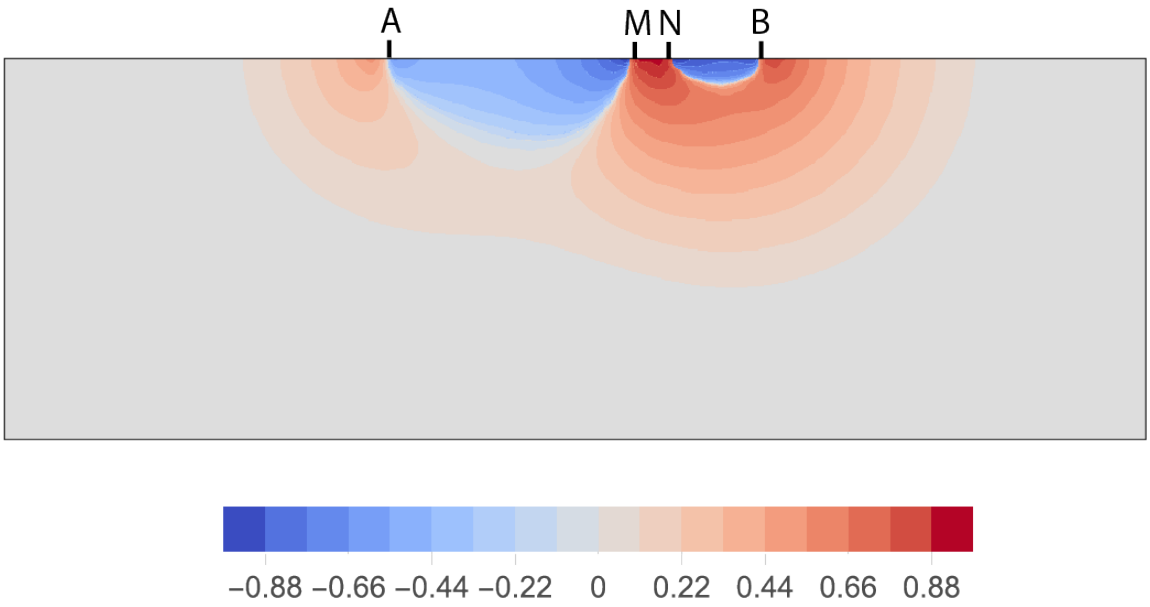

Figure 5.9: Multiple Gradient array sensitivity plot scaled from -1 to 1 on homogeneous ground. Modified from Loke (2015).

- **DOI.** It is comparable to the Pole-Dipole and Wenner-Schlumberger arrays.
- **S/N.** The S/N ratio is more favorable than in the case of the Dipole-Dipole or Pole-Dipole arrays (Dahlin and Zhou, 2006).

Conclusion

From these outlooks, it should have become obvious that the choice of an appropriate configuration beforehand is primordial. One has to consider the different strengths and weaknesses of the various methods in order to choose the array that is optimal in his investigation. It is thus helpful to know ahead of time what kind of causative bodies to look for, what is their shape, etc. The choice of the electrode configuration in the aim of this study will be explained in Chapter 6 - survey design.

Array	a	s	n	Median depth	k	S/N
Wenner	0.3333	-	-	0.173	2.09	1
Gradient	0.0909	9	1	0.0481	1.12	1.874
Gradient	0.0909	9	2	0.0897	3.16	0.662
Gradient	0.0909	9	3	0.1347	5.64	0.371
Gradient	0.0909	9	4	0.1743	7.74	0.271
Gradient	0.0909	9	5	0.1902	8.57	0.244
Gradient	0.05	18	1	0.0261	0.62	3.353
Gradient	0.05	18	2	0.0471	1.85	1.133
Gradient	0.05	18	3	0.0683	3.61	0.58
Gradient	0.05	18	4	0.0909	5.8	0.361
Gradient	0.05	18	5	0.115	8.25	0.254
Gradient	0.05	18	6	0.1397	10.72	0.195
Gradient	0.05	18	7	0.1626	12.95	0.162
Gradient	0.05	18	8	0.1804	14.64	0.143
Gradient	0.05	18	9	0.19	15.55	0.135
Dipole-Dipole	0.3333		1	0.1386	6.28	0.333
Dipole-Dipole	0.25		2	0.1743	18.85	0.111
Dipole-Dipole	0.2		3	0.1923	37.7	0.056
Dipole-Dipole	0.1667		4	0.2034	62.83	0.033
Dipole-Dipole	0.1429		5	0.2108	94.18	0.022
Dipole-Dipole	0.125		6	0.2162	131.95	0.016
Dipole-Dipole	0.1111		7	0.2204	175.97	0.012
Dipole-Dipole	0.1		8	0.2236	226.19	0.009

Table 5.1: Median depth of investigation, geometric factor k, and S/N ratio relative to the Wenner array, for varying a, n and s in the Multiple Gradient case. The total profile length is 1 in all cases. Modified from Dahlin and Zhou (2006).

Chapter 6

Survey design

Synopsis

The choice of the profiles position will be explained, as well as the electrode configuration and the induced polarization acquisition parameters in light of the last chapters.

6.1 Profiles location

The main objective of this study is to characterize contact zones between the diorite intrusive and the host sedimentary sequence in the ORman prospect, about 5 km North of the OKvau Project area (see Chapter 2). The positioning of the profiles was elaborated with C. Johnson, the Exploration Manager / Chief Geologist at Emerald Resources NL.

Five profiles were designed:

1. **OKvau calibration.** 475 m layout perpendicular to the main mineralization strike. Designed to get signals to calibrate our results on the well studied deposit, and extrapolate those results onto the following ORman prospect profiles (Figure 6.1).
2. **ORman 1.** 955 m layout spanning diorite to get a clear signature of this rock in the ORman intrusive, and compare the IP signals with the sedimentary sequence (Figure 6.2).
3. **ORman 2.** 1115 m layout crossing the contact zone in its middle (Figure 6.2).
4. **ORman 3.** 1115 m layout crossing two contact zones on both sides of the sedimentary tongue (Figure 6.2).

5. **ORman 4.** 1115 m layout crossing two contact zones on both sides of the southern tip of the sedimentary tongue (Figure 6.2).

The ORman profiles are oriented in the east-west direction, positioned parallel to each other from the North to the South. Their positioning was controlled by drilling surveys that occurred recently in the area. It was practical to design them parallel to the drill holes to thereafter compare the logs with the DC/IP signals.

As mentioned in subsection 2.1.1, the gently undulating topography would not constraint too much the investigations. However, vegetation was problematic. A field crew was appointed to clear the profile lines beforehand in order to ease the transportation of material, electrode planting, etc.

6.2 Electrode configuration

Considering all the points mentioned in Chapter 5, it was decided to use the **multiple gradient array** configuration. Indeed, its favorable sensitivity and S/N ratio (see table 5.1) combined with its robustness and multi-channel compatibility made it the most appealing choice. Its superiority compared to the classical Wenner array or Dipole-Dipole array has been tested and proven by Dahlin and Zhou (2006) for resistivity cases. Aizebeokhai and Oyeyemi (2014) successfully applied it to a time-domain IP problem, and mentioned that "the multiple-gradient array is a fast and cost effective electrode configuration that is easy to use for rapid 2D electrical resistivity and IP surveys".

The maximum electrode spacing, or a factor, was chosen (5 m) in order to maximize the depth of penetration.

In order to cover the effective length of the profiles, the roll-along technique was used.

Owing to the length of the profiles, the amount of time available and the climatic conditions, it was unfortunately deemed impossible to realize reciprocals on any profile.

6.3 DC/IP acquisition parameters

Below is a list of some relevant acquisition settings during the investigation. Some of them were modified according to the conditions, such as the electrode contact resistance threshold and the injection time. Furthermore, the maximum number of stack had to be reduced to 2, because the survey cost too much time.

- **Injected current properties**
  - Current higher limit (A) : 0.2
  - Current lower limit (A) : 0.02
  - Voltage limit (V) : 600
  - Base frequency (Hz) : 50
- **Electrode testing**
  - Contact resistance limit (ohm) : 5000
- **IP measurement**
  - Delay between current turn-on and start of measure (s) : 0.5
  - Integration time (s) : 3
  - Delay before measure after the current is switched-off (s) : 0.06
  - Stack number min. : 1
  - Stack number max. : 3
  - Error limit (%) : 3
  - Number of IP windows : 17

6.4 Equipment list

Terrameter device - The ABEM Terrameter LS is a resistivity/IP instrument.

- Brand : ABEM[1]
- Name : Terrameter LS 12-064-250 (Type 33 3000 12)
- Precision : 0.1 %
- Accuracy : 0.2 %
- Theoretical resolution : 3 nV

Its rugged aluminium case, meeting IEC IP66, allows it to be utilized in harsh environments.

[1] http://www.guidelinegeo.com/product/abem-terrameter-ls-2/

Electric cables coils - Four cable coils of 80 m each.

Connectors - More than 64 connectors to connect the electrodes to the cables.

Electrodes - Eighty-one 40 cm-long sharpened stainless steel electrodes.

Batteries and charger - Two 12 V car batteries (70 A·h and 90 A·h respectively) and their charger.

Electrode preparation

The electrodes were specially manufactured in the aim of this study. Stainless-steel bars were cut into 40 cm long rods and mechanically sharpened at one end, which greatly helped the planting in all conditions. However, some rusting appearing over time had to be frequently removed with sandpaper. This might either be due to the quality of the steel, the intense current injection, the composition of the soil or more likely a combination of these effects.

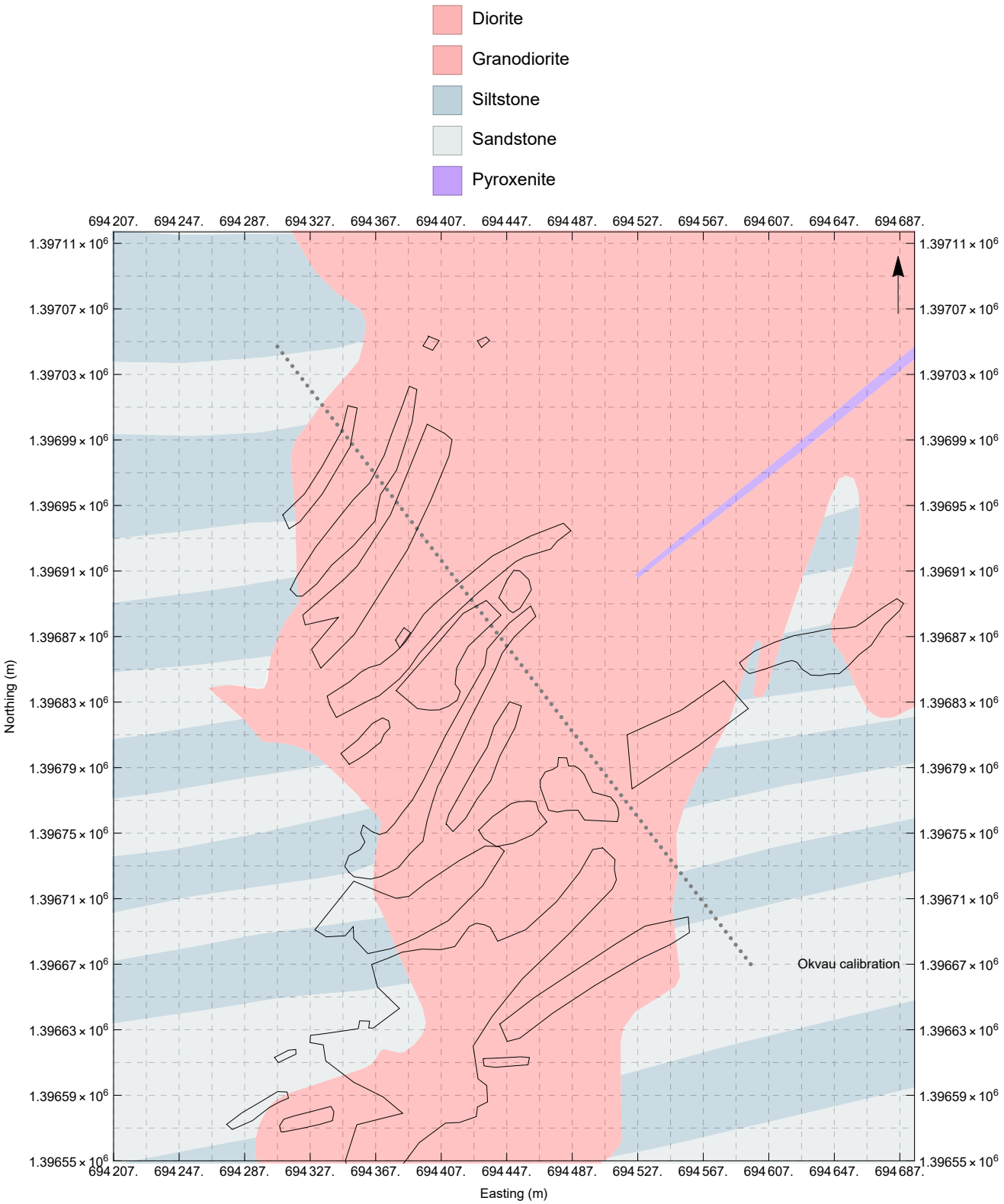

Figure 6.1: Profile location (gray dotted line) over the geological map in the OKvau area. The mineralization outline is delineated in black.

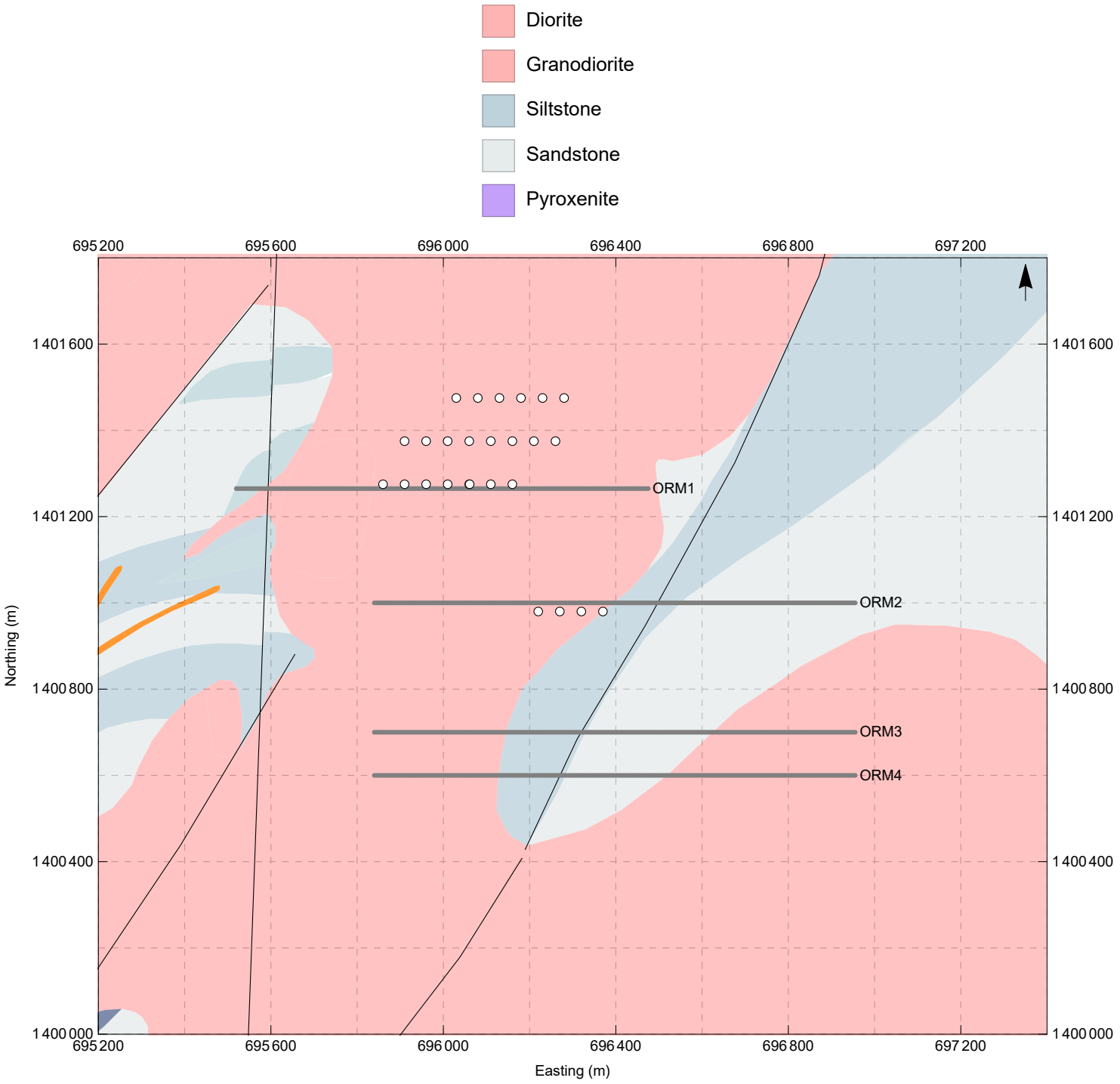

Figure 6.2: Profiles location (gray lines) over the geological map in the ORman area. Faults are represented in black and the drill holes as dark circled white dots.

Chapter 7

Geophysical context

Synopsis

Before presenting the inversion results of this study, in order to provide some context, selected previous geophysical studies conducted in the investigation area are summarized. The aim is to find out which physical parameters are linked together and what kind of signal to expect.

Introduction

Since the early development of the project, several geophysical studies performed by consultants have been conducted in the OKvau area to characterize the main feature of the deposit and discover new potential reserves. The main methods used during that period are airborne/ground magnetics, resistivity and induced polarization techniques. The latter has proven to be a powerful technique to target features or exploring in intrusive bodies. Furthermore, the mineralizations at OKvau have displayed high chargeabilities (Bourne, 2015).

7.1 Magnetics

7.1.1 Aeromagnetics

In 2014, a regional scale aeromagnetic interpretation was realized over the OKvau surroundings utilizing high-resolution aeromagnetic data (Bourne and Beinke, 2015). It brought significant geological understanding of the region and led into defining new targets for gold investigation.

The Reduced To Pole (RTP) data, illustrated in the OKvau and ORman areas in Figure 7.1 and Figure 7.2 respectively, presupposes that local magnetisation is controlled by induced fields. In this case, it seems that the magnetic signals near the mineralizations possess a remanent component due to the deep low in magnetic values (Bourne and Beinke, 2015).

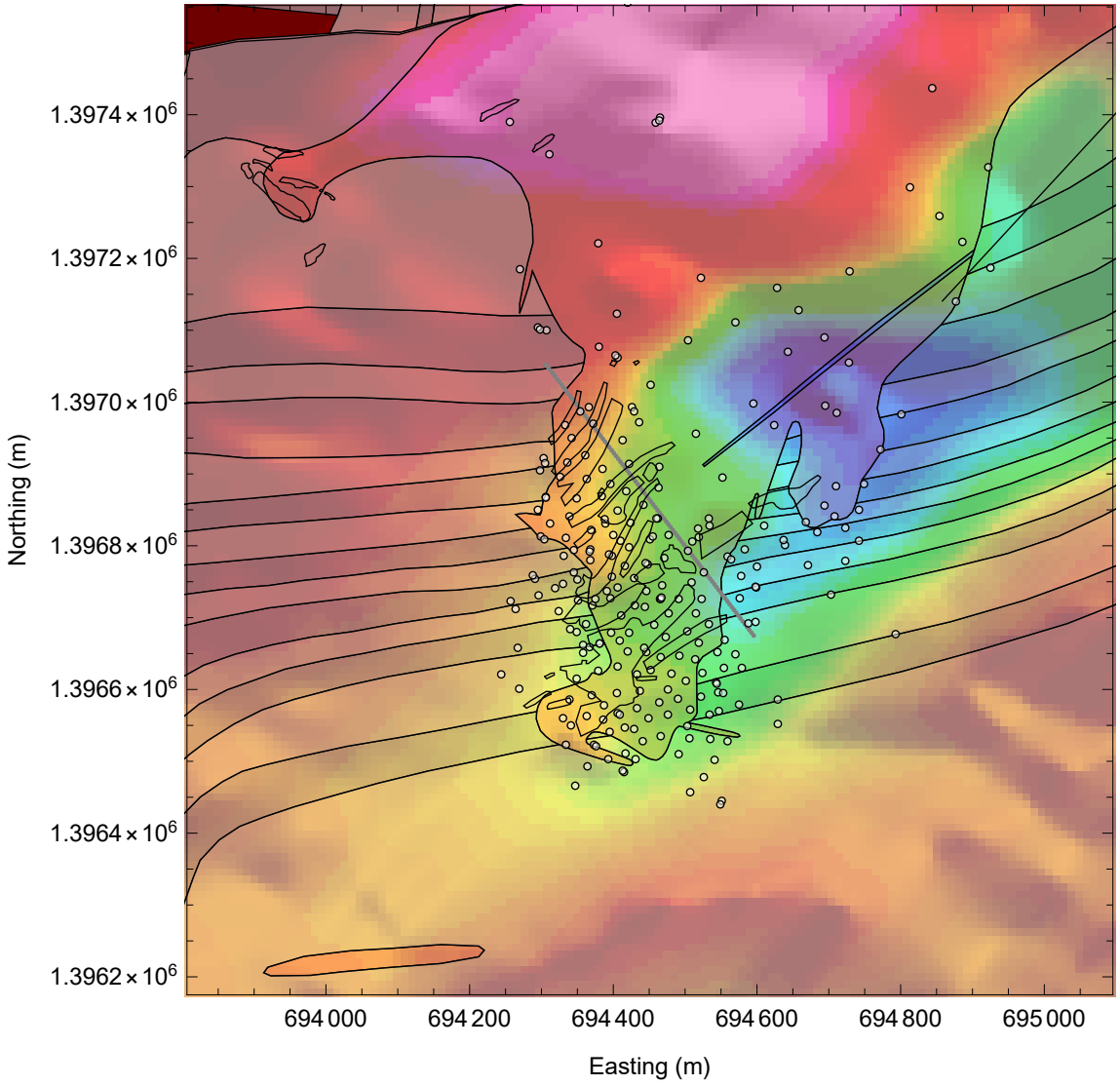

Figure 7.1: Reduced To Pole magnetic field data at OKvau. The lithologies, mineralization outlines, drill holes and the calibration line are outlined.

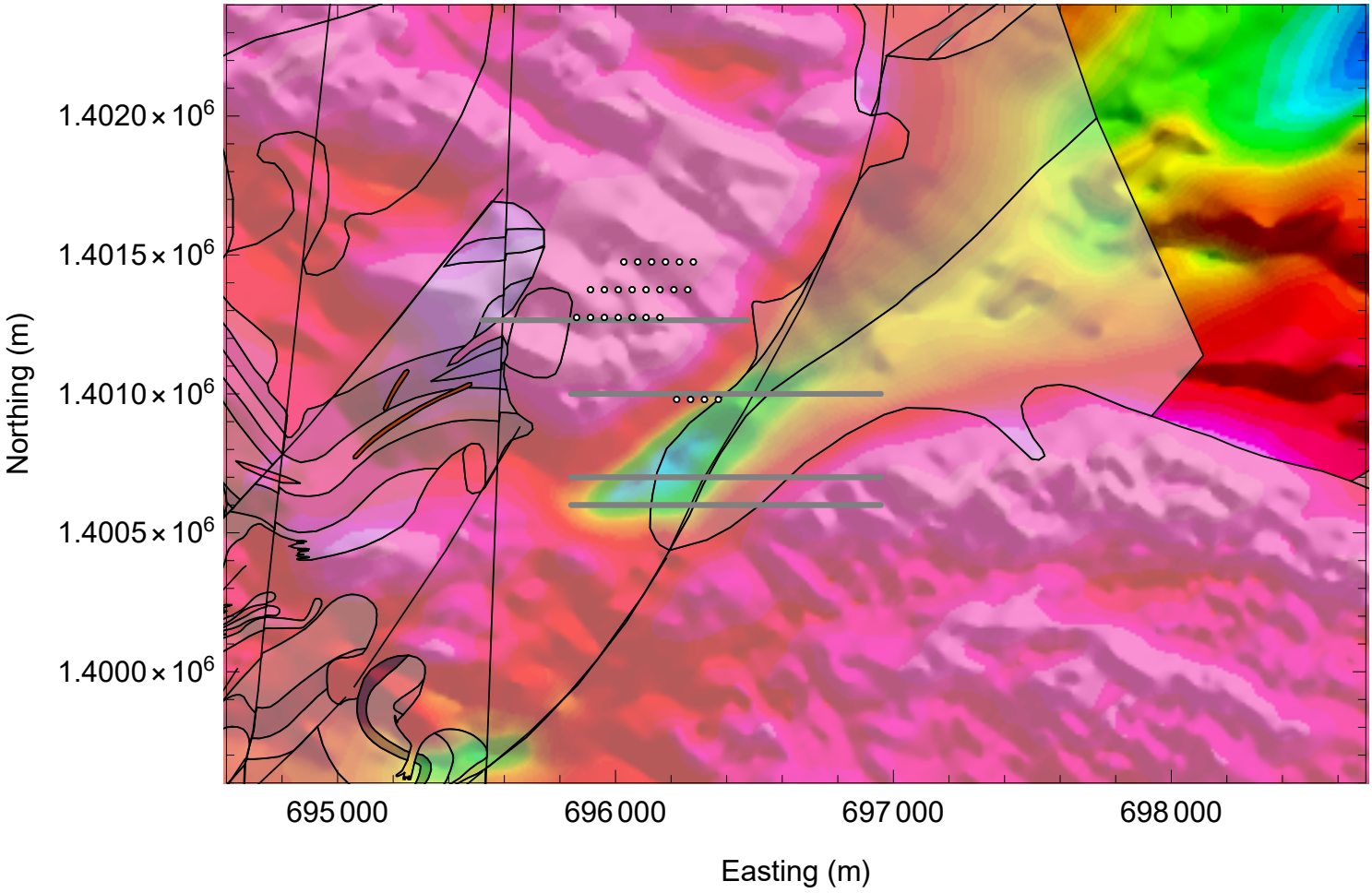

Figure 7.2: Reduced To Pole magnetic field data at ORman. The lithologies, mineralization outlines, drill holes and the calibration line are outlined.

7.1.2 Ground magnetic

An array of ground magnetic surveys were realized on small portions of areas. The aim was to perform Magnetic Vector Inversions (MVI) to model underground features containing a combination of remanent magnetization, demagnetization, anisotropy of magnetic minerals (e.g. magnetite, pyrrhotite, ilmenite). However, the ORman area was not covered by this survey. The conclusion in the OKvau neighbourhood is similar to that of the aeromagnetics survey: mineralization gives the impression to happen near areas of high magnetic susceptibility, in areas of magnetite elimination or low magnetic response.

7.2 Resistivity and induced polarization

In 2016, an IP/resistivity and 3D magnetic inversion survey took place in the OKvau area (Bourne, 2016). The aim was :

- to determine what zones of mineralizations look like, by targeting specific confirmed mineralized areas within sections,
- to differentiate between the several types of mineralization, in terms of chargeability, resistivity (and magnetic susceptibility),
- targeting new potential zones of interest for further exploration.

This work is particularly helpful as part of this thesis since it poses a sort of reference through which the results can be compared. Unfortunately, the ORman prospect was not part of their investigation, but since the context is similar to that of OKvau, their product can be still be used. Some of the study conclusions are cited below.

Prime mineralization at OKvau is usually linked to (Bourne, 2016) :

- Medium to high chargeability,
- Low to medium resistivity ($\leq$ 300 Ω·m),
- Adjacent to elevated magnetic susceptibility features.

According to Bourne (2016), the resistivity factor is quite penalizing. If a target presents an elevated chargeability but is located within a highly resistive zone, the interest for the area drops. However, the magnetic susceptibility can significantly help to decide whether or not to exclude the area. Unfortunately, magnetic modelisation has only been realized on few portions of the deposit area.

Discussion

The magnetic studies have been interesting in a first phase to refine the geological map and define new targets. The MVI realized on some portions of the map was helpful in determining what kind of magnetic susceptibility feature to expect when mineralized zones are present, but are not available for the majority of the area, they are restricted to the local OKvau prospect area.

Regarding the IP/resistivity studies, most of them were realized on a large scale, detecting global trends in the different targeted features, thus producing broad and smoothed chargeability bodies, that helped figuring out the general shape and trend of the mineralization

and its relation with magnetic susceptibility.

The difference with the field work realized in the aim of this thesis is that in this case the zone of investigation is more concise, applied on a limited number of targeted zones of interest, in order to detect smaller features than the previous studies. Furthermore, significant inversion methodology research has been carried out to produce sharp images of the subsurface, which might bring some insights into the geology of mineralization.

Chapter 8

Theory : Inversion

Synopsis

In this chapter, general principles of parameter estimation and inverse problem will be covered with a focus on the ERT and IP, and will lead to the explanation of the need of a stabilizing functional such as the MGS.

8.1 Introduction

The goal is to reveal physical parameters that constitute an unknown model m, from gathered observations making up the dataset, d. Expecting that the fundamental physics are acceptably understood, the model and the dataset are related by a function G, such that

$$G(m) = d. \tag{8.1}$$

In this case, d is a collection of discrete observations of *apparent resistivities* ($\Omega\cdot$.m) for the ERT, as displayed on figure 8.2, and of *apparent chargeabilities* (no units or mV/V) for the IP. The observations always contain some amount of *noise* (whose origins are discussed in subsection 5.2.3), frequently originating from unmodeled influences on instrument readings and numerical round-off (Aster et al., 2013a). The dataset can thus be conceptualized as observations from an ideal survey, d_{true}, contaminated by a noise component η, such that

$$d = d_{true} + \eta = G(m_{true}) + \eta. \tag{8.2}$$

In the last expression, m_{true} is the *true* model, it thus exactly satisfies $G(m_{true}) = d_{true}$, i.e. it is the real resistivity/chargeability distribution of the subsurface. It should be noted that an infinite number of models, aside from m_{true}, satisfies the system $G(m) = d$ (Aster et al., 2013a). G is called the *forward operator*. In ERT/IP, there is no explicit analytical

formula to relate the model parameters to the observations, so G relies on a finite difference or finite element scheme (Kemna, 2000), that will reproduce the observations d given a user-specified or estimated model m. The latter operation is called forward modeling and the problem of finding d given m is called a *forward problem*. The point at issue of finding m given d is called an *inverse problem*.

In this case, the aim is to determine a finite number of parameters, to define a model m that will be considered to be the closest to reality given the observations vector d and the geological, geophysical and petrophysical information at disposal. The parameters of interest are the resistivity ρ (Ω·m) (or its inverse, the conductivity σ in S·m^{-1}) and the chargeability ς, which has no units. Those physical entities will be computed in each block of a mesh such as the one represented in figure 8.3.

The parameters of interest (ρ, ς) have a naturally non-linear dependency to the observed data, which means that the system $G(m) = d$ does **not** obey the following properties (Aster et al., 2013a) :

- Superposition
$$G(m_1 + m_2) = G(m_1) + G(m_2). \tag{8.3}$$
- Scaling
$$G(\alpha m) = \alpha G(m). \tag{8.4}$$

This is important because there is no general theory for the solution of non-linear parameter estimation and inverse problems. Iterative methods integrating linear approaches have to be applied to solve them (Aster et al., 2013c).

To compute a solution of an inverse problem, it is necessary to figuring out if the estimated model m_{est} is consistent with the observations d. That is, given an acceptable threshold $\varepsilon \in \mathbb{R}^+$, by checking if the residuals $||G(m_{est}) - d||_p$ satisfy (Zhdanov, 2009)

$$||G(m_{est}) - d||_p \leq \varepsilon, \tag{8.5}$$

where p designates the type of norm used (sort of *misfit measure*). The residuals are the differences between the actual observations and the theoretical predictions of the forward modeling. The traditional strategy is to resort to the use of the *2-norm*

$$||G(m_{est}) - d||_2 = \sqrt{\sum_{i=1}^{m} (G(m_{est,i}) - d_i)^2}, \tag{8.6}$$

where m in the last expression corresponds to the number of observations (that is, d is a $[m \times 1]$ vector). An alternative misfit measure is the *1-norm*

$$||G(m_{est}) - d||_1 = \sum_{i=1}^{m} |G(m_{est,i}) - d_i|. \tag{8.7}$$

The 1-norm residual measure is less sensitive to data outliers, points that are not in harmony with the mathematical model. Such techniques that are resistant to data outliers are called robust estimation procedures (Aster et al., 2013a).

In geo-electrical field practices, the inverse problem is said to be **ill-conditioned**. Inversely, a problem is said to be well-conditioned if it meets the following requirements (Aster et al., 2013a; Zhdanov, 2009; Kirsch, 2011) :

1. The solution m of $G(m) = d$ exists over the entire data space.
2. The solution m is unique.
3. The solution is stable, i.e. a small perturbation of d only causes small variations to the solution m.

An inverse problem is said to be ill-conditioned if it fails at least one of the above requirements. To counter the detrimental aspects of ill-conditioning, **regularization** techniques have to be implemented in the inversion procedure in order to produce an existing, stable and unique solution.

8.2 Correctness set

An easy way to surmount the difficulties of ill-conditioning is to limit the class of models which are used in the inversion process (Zhdanov, 2009). Rather than considering the entire model space $\mathcal{M}$, it is possible to target on models m from some subspace of $\mathcal{M}$ that contains relevant models for the given inverse problem, by adding some $information$ regarding the solution. Tikhonov and Arsenin (1977) introduce the concept of the *correctness set*, $\mathcal{C}$, enclosing the solutions with the property that there exists an inverse operator G^{-1}, defined on $G\mathcal{C} \subset \mathcal{D}$, $\mathcal{D}$ being the data space, and that G is continuous. Its typical feature is that the inverse problem becomes well-conditioned if it is determined on $\mathcal{C}$ only.

Definition 8.2.1. *The subset $\mathcal{C}$ of a metric space $\mathcal{M}$ is compact if any sequence $m_l \in \mathcal{C}$ of elements in $\mathcal{C}$ contains a convergent subsequence $m_{l_j} \in \mathcal{C}$, which converges to an element m in $\mathcal{C}$ (Zhdanov, 2009).*

Tikhonov and Arsenin (1977) proved that any compact subset of the metric space $\mathcal{M}$ can be adopted as a correctness set for an ill-conditioned inverse problem. This approach is

adequate if the user knows *a priori* the class of the models ($\mathcal{C}$) where to look for a solution (Zhdanov, 2015).

8.3 Regularizing operators

The regularization theory brings help toward the unstable, unrealistic solutions of ill-conditioned inverse problems. Let's consider the geo-electrical inverse problem described by equation 8.1. The fundamental concept of any regularization algorithm is the approximation of the non-continuous inverse forward operator G^{-1} by a family of continuous operators $R(d, \alpha)$. The parameter $\alpha \ \epsilon \ \mathbb{R}^+$ in the last expression is termed the regularization parameter. The regularization must be such that as $\alpha \to 0$, the operators should approach the exact inverse forward operator G^{-1} (Zhdanov, 1993). For the sake of rigour, here are the formal definitions from the work of Tikhonov and Arsenin (1977):

Definition 8.3.1. *The operator $R(d_t, \alpha)$ is called the regularizing operator in some vicinity of the element $d_t = G(m_t)$, where d_t is the true vector of observations and m_t the exact solution of $G(m_t) = d_t$, if :*

1. *The real positive numbers α_0 and δ_0 are such that the operator $R(d_t, \alpha)$ is determined for any α and d_t satisfying the conditions*

$$0 < \alpha < \alpha_0 \text{ and } \rho_{\mathcal{D}}(d_\alpha, d_t) < \delta_0,$$

   where d_α is the reproduced data vector and $\rho_{\mathcal{D}}(d_\alpha, d_t)$ is the distance between d_α and d_t in the metric of $\mathcal{D}$.

2. *There is a function $\alpha(\delta)$ such that for any $\varepsilon > 0$ a positive number $\delta(\varepsilon)$ can be found such that*

$$\rho_{\mathcal{D}}(d_\alpha, d_t) < \delta(\varepsilon),$$

   for

$$\rho_{\mathcal{M}}(m_\alpha, m_t) < \varepsilon.$$

   Here

$$m_\alpha = R(d_t, \alpha(\delta)).$$

Definition 8.3.2. *The operator R(d, α) is called the regularizing operator for $G(m) = d$ on some subset $\mathcal{D}_1 \subset \mathcal{D}$ if it is regularizing in the vicinity of any point $d \ \epsilon \ \mathcal{D}_1$. Regularizing operators can be constructed by approximating the ill-conditioned system of equations $G(m) = d$ by the system of well-conditioned equations :*

$$G_\alpha(m) = d,$$

where corresponding inverse forward operator G_α^{-1} are continuous.

To select the appropriate family of regularizing operators, Tikhonov and Arsenin (1977) proposed the following strategy for constructing regularizing operators, based on the introduction of special stabilizing and parametric functionals (Zhdanov, 2009).

8.4 Stabilizing functionals

Stabilizing functionals are used to pick from the space $\mathcal{M}$ of all possible models the subset $\mathcal{C}$ (correctness set).

Definition 8.4.1. *A non-negative functional $s(m)$ in some metric space $\mathcal{M}$ is called a stabilizing functional if, for any real number $c > 0$ from the domain of functional values, the subset $\mathcal{M}_c$ of the elements $m \in \mathcal{M}$, for which $s(m) \leqslant c$, is compact (Zhdanov, 2009).*

Definition 8.4.2. *Let $\mathcal{X}$ be a non-empty set and d a real-valued function defined on $\mathcal{X} \times \mathcal{X}$ such that for $a, b \in \mathcal{X}$:*

1. *$d(a,b) \geq 0$ and $d(a,b) = 0$ if and only if $a = b$*
2. *$d(a,b) = d(b,a)$, and*
3. *$d(a,c) \leq d(a,b) + d(b,c)$, for all a, b and c in $\mathcal{X}$.*

*Then d is said to be a **metric** on $\mathcal{X}$. $(\mathcal{X}, d)$ is called a **metric space** and $d(a,b)$ is referred to as the distance between a and b (Morris, 2017).*

There are many typical stabilizers available (Zhdanov, 2009). In this work, the stabilizing functional of interest is the **Minimum Gradient Support functional**, described in Chapter 9.

Zhdanov (2015) explains how to use a stabilizer to select a suitable class of models. Presuming that the data d_δ is observed with some level of noise, $d_\delta = d_{true} + \delta d$ is the same as assuming that the misfit between d_δ and d_{true} is inferior to the level of the errors in the observed data, $\delta = ||\delta d||$,

$$\rho_{\mathcal{D}}(d_\delta, d_t) \leq \delta. \tag{8.8}$$

In this position, it is logic to look for a close solution in the set $\mathcal{Q}_\delta$ of the models m such that

$$\rho_{\mathcal{D}}(G(m), d_\delta) \leq \delta, \tag{8.9}$$

where $\mathcal{Q}_\delta$ is a set of possible, acceptable solutions.

The primary purpose of a stabilizer is to select from $\mathcal{Q}_\delta$ the solutions m that continuously depend on d and which are endowed with a specific property depending on the choice

of the stabilizing functional (e.g. for the MGS stabilizer; models with sharp boundaries). Such models can be singled out by the condition of the minimum of the stabilizer :

$$s(m \mid m \, \epsilon \, \mathcal{Q}_\delta) = min. \tag{8.10}$$

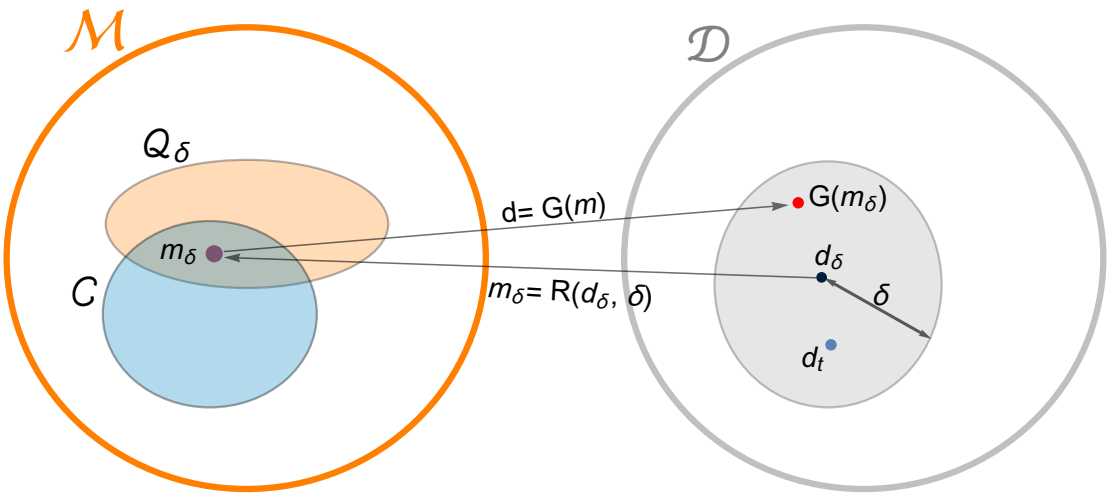

Figure 8.1: Stabilizing functionals help selecting solution m_δ, belonging at the same time to the correctness subset $\mathcal{C}$ that they define, and to the subset of the acceptable solutions regarding the misfit, $\mathcal{Q}_\delta$. Modified from Zhdanov (2015).

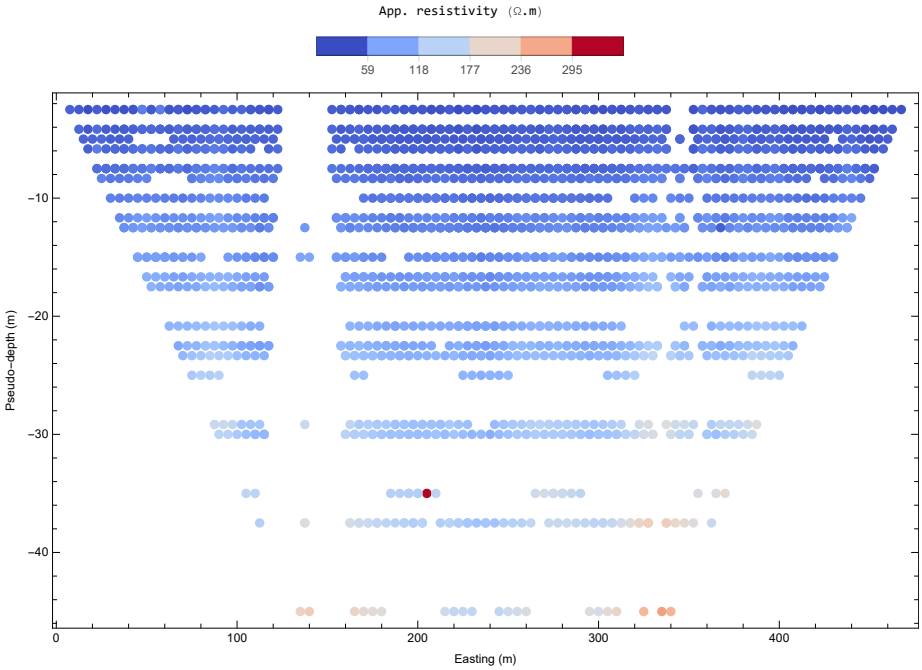

Figure 8.2: Collected apparent resistivity data for the calibration line.

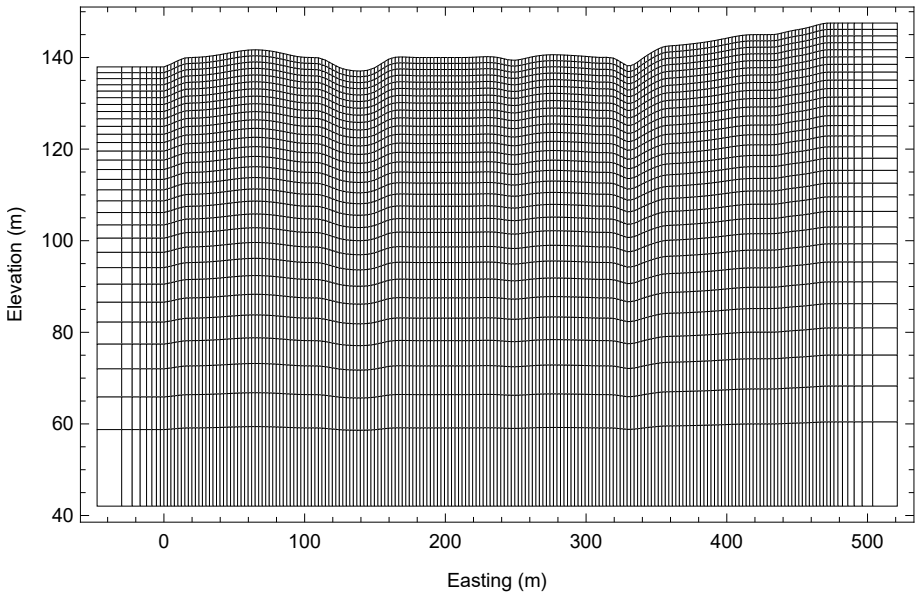

Figure 8.3: Discretized subsurface forming the model parameters for the OKvau calibration line.

8.5 Non-linear regression

It was specified in the last sections that the final solution to the inverse problem should be chosen from the intersection of a correctness set defined by the stabilizing functional, containing models with specific properties, and a set of possible solutions based on the misfit function (Figure 8.1). For a regularized non-linear least-square inverse problem, this can be formulated as (Aster et al., 2013b) :

$$\begin{aligned} &min||Rm||_2 \\ &||W_d(G(m) - d)||_2 \leq \delta, \end{aligned} \tag{8.11}$$

where W_d and R are the data weighting and the stabilizing matrices, respectively.

Applying the method of *Lagrange Multipliers* to the system (8.11) gives the following parametric functional (Zhdanov, 2015) :

$$P^{\alpha}(m, d) = ||W_d G(m) - W_d d||_2^2 + \alpha^2 ||Rm - Rm_{apr}||_2^2. \tag{8.12}$$

Where α is the regularization parameter and m_{apr} is some user-specified *a priori* model. $P^{\alpha}(m, d)$ is the objective function and commonly called the *damped least-square problem* (Aster et al., 2013b),

The problem in (8.11) can now be simply written as :

$$min(P^{\alpha}(m, d)). \tag{8.13}$$

Since the resistivity inverse problem is not linear, the objective function has to be minimized in an iterative fashion, starting from a user-specified model m_0, solving a linear system of equation for a model update until an acceptable data misfit target is reached.

Using a classical Gauss-Newton scheme :

$$min(P^{\alpha}(m, d)) = min \left\| \begin{matrix} G(m) - d \\ \alpha Rm \end{matrix} \right\|_2^2. \tag{8.14}$$

The Jacobian of the last expression for the k_{th} iteration is

$$K(m^k) = \begin{bmatrix} J(m^k) \\ \alpha R \end{bmatrix} \tag{8.15}$$

where $J(m^k)$ is the Jacobian of $G(m^k)$, and m^k is the model as computed at iteration k ($k = 1, 2...$).

A Gauss-Newton model step is computed by solving for Δm the following expression (Aster et al., 2013b) :

$$[J(m^k)^T J(m^k) + \alpha^2 R^T R]\Delta m = -J(m^k)^T [G(m^k) - d] - \alpha^2 R^T R m^k. \tag{8.16}$$

The model is updated by : $m^{k+1} = m^k + \Delta m$. At each iteration k, before the model is refreshed, a line-search is realized to pick the optimal regularization parameter α, i.e. the one that minimizes the most the data misfit.

The end of the iterative process is controlled by the value of the *root mean square* (RMS) :

$$\begin{aligned} RMS(m^k) &= \sqrt{\frac{||W_d(G(m^k) - d)||_2}{N}} \\ &= \sqrt{\frac{||W_d(d^k - d)||_2}{N}}. \end{aligned} \tag{8.17}$$

From statistical theory, the stopping criterion should correspond to a RMS value of 1 (Kemna, 2000).

Algorithm 1 The Gauss-Newton inversion

Select the appropriate stabilizer and start with a user-specified initial model m_0. Repeat the following steps to produce a succession of solutions m^k (k = iteration number). Stop the procedure when the RMS (eq. 8.17) is such that RMS$(m^k) \leq 1$.

1: Realize the forward modeling $d^k = G(m^k)$.
2: Compute the Jacobian $J(m^k)$ and $R^T R$.
3: Compute updated models corresponding to an array of regularization parameters α's by

$$m^{k+1} = m^k - [J(m^k)^T J(m^k) + \alpha^2 R^T R]^{-1} [J(m^k)^T [G(m^k) - d] - \alpha^2 R^T R m^k].$$

4: Pick the m^{k+1} with the largest value of α that minimizes the RMS (8.17).
5: Let $k = k + 1$.

8.6 Forward modeling

Forward modeling is the operation of computing what would be the instrument readings for a given model parameters distribution, either user-defined, or at each iteration in an iterative inversion scheme such as in the Gauss-Newton algorithm.

A brief outline of the techniques used to realize such essential operations in resistivity

and IP investigations is described in what follows.

The adopted code CRTomo works with complex conductivity and complex chargeability. It uses a finite element scheme to solve the forward problem (Kemna, 2000).

8.6.1 Resistivity

Let Φ be the hypothetical potential that is measured in the absence of any chargeability phenomena. If G is the forward DC resistivity operator, then :

$$\Phi = G(\sigma), \tag{8.18}$$

where σ is the conductivity distribution giving rise to Φ. The forward operator linking those two parameters is determined by the Poisson equation (Oldenburg and Li, 1994):

$$\nabla \cdot (\sigma \nabla \Phi) = -I\delta(r - r_s) \tag{8.19}$$

where $(\nabla\cdot)$ and (∇) respectively designate the divergence operator and the gradient operator, I is the amount of injected current in amperes, δ is the Dirac delta function and r_s designates the location of the current electrode. The boundary conditions of the problem (8.19) are :

- $\dfrac{\partial \Phi}{\partial n} = 0$ at the Earth's surface, where n denotes the outward normal.
- Mixed boundary condition : $\sigma \dfrac{\partial \Phi}{\partial n} + \beta\phi = 0$, where β is a parameter defining the type of boundary condition (e.g. $\beta = 0$ at the Earth's surface).

8.6.2 Induced polarization

Using the formulation of Seigel (1959), presented in subsection 3.3.3, the apparent chargeability can be expressed as (Oldenburg and Li, 1994; Kemna, 2000):

$$M_a = \frac{G(\rho_{IP}) - G(\rho_{DC})}{G(\rho_{IP})}, \tag{8.20}$$

where G is the resistivity forward operator, ρ_{DC} is the DC resistivity and ρ_{IP} is the perturbed resistivity (Seigel, 1959) :

$$\rho_{IP} = \frac{\rho_{DC}}{1 - m}, \tag{8.21}$$

where m is the intrinsic chargeability. Ultimately, the apparent chargeability can be computed from the solution of two DC resistivity forward operations (Binley, 2015).

Chapter 9

Theory : Minimum Gradient Support

Synopsis

The Minimum Gradient Support stabilizing functional and its predecessor, the Minimum Support functional will be presented in this chapter.

9.1 Introduction and motivation

The idea of the Minimum Gradient Support was developed by Portniaguine and Zhdanov (1999), based on the previous work on the Minimum Support by Last and Kubik (1983). Their motivation was to develop a stable inverse problem solution that would resolve complex, focused geological features, contrarily to the traditional least-square approach which produces smoothed images of causative bodies which might in reality have a specific shape, whose borders would be blurred. If the object of investigation is the contact between two different lithologies or the depth of the water table, there is a clear interest in looking for the resolution of sharp contrast instead of a smooth image (Blaschek et al., 2008).

9.2 Formulation

The MS and MGS belong to the class of focusing stabilizing functionals.

Stabilizing functional are used in ill-posed inverse problems to select from the space $\mathcal{M}$ of all possible models the subset $\mathcal{M}_{\mathbf{c}}$, which is a correctness set Zhdanov (2009). Before introducing the MGS functional, its predecessor, the MS functional, will be presented. It was developed in 1983 by Last and Kubik (1983).

To maximize the compactness of the model, if d and h are the block dimensions, a definition of the area in a two-dimensional model is :

$$area = dh \lim_{\beta \to 0} \sum_{j=1}^{N} \frac{m_j^2}{m_j^2 + \beta}. \tag{9.1}$$

The MS functional thus provides a model with a minimum area of the distribution of anomalous parameters (Last and Kubik, 1983; Zhdanov, 2009). Let us observe the property of the function of m in (9.1) :

$$\lim_{\beta \to 0} \frac{m_j^2}{m_j^2 + \beta} = 0 \quad \text{for m} = 0$$

$$= 0 \quad \text{for m} \neq 0.$$

Zhdanov (2009) presents a formalization of Last and Kubik's idea, and denotes the support of m as **spt** $\boldsymbol{m}$, a model parameter support, corresponding to the combined closed sub-domains of V where $m \neq 0$. By considering the following functional of the model parameters and focusing parameter β :

$$\begin{aligned} s_\beta(m) &= \int_{\mathbf{V}} \frac{m(r)^2}{m(r)^2 + \beta^2} dv \\ &= \int_{\mathbf{spt}\ \boldsymbol{m}} 1 - \frac{\beta^2}{m(r)^2 + \beta^2} dv \\ &= \text{spt}\ m - \beta^2 \int_{\mathbf{spt}\ \boldsymbol{m}} \frac{1}{m(r)^2 + \beta^2} dv \end{aligned} \tag{9.2}$$

From equation (9.2), it is obvious that $s_\beta(m) \to \text{spt}\ m$ when $\beta \to 0$.

s_β can thus be treated as a functional proportional to the model parameter support spt m, for small β's. A minimum support stabilizing functional $s_{MS}(m)$ can be elaborated from this latter functional as :

$$s_{MS}(m) = s_\beta(m - m_{apr}) = \int_{\mathbf{V}} \frac{(m - m_{apr})^2}{(m - m_{apr})^2 + \beta^2} dv \tag{9.3}$$

The functional (9.3) has the property to minimize the total area with non-zero departure of the model parameters from the given *a priori* model.

- A dispersed, smooth distribution of the model parameters with values distant from the *a priori* model m_{apr} will result in a considerable penalty function.

- Contrarily, well-focused parameter distributions not far from m_{apr} will get a small penalty function.

To boost the resolution of compact structures, Portniaguine and Zhdanov (1999) used the properties of the minimum support functional $s_{MS}(m)$ and introduced a minimum gradient support functional $s_{MGS}(m)$:

$$s_{MGS}(m) = s_{\beta}[\nabla m] = \int_{\mathbf{V}} \frac{\nabla m \cdot \nabla m}{\nabla m \cdot \nabla m + \beta^2} dv \tag{9.4}$$

The *gradient support* is denoted by $\mathbf{spt}\ \nabla \boldsymbol{m}$. It corresponds to the combined closed subdomains of V where $\nabla m \neq 0$. Then, similarly to the development in (9.2), the expression (9.4) can be modified as :

$$s_{MGS}(m) = \text{spt}\ \nabla m - \beta^2 \int_{\mathbf{spt}\nabla \boldsymbol{m}} \frac{1}{\nabla m \cdot \nabla m + \beta^2} dv \tag{9.5}$$

From the last equation, let's observe that $s_{MGS}(m) \rightarrow \text{spt}\ \nabla m$, when $\beta \rightarrow 0$.

The functional $s_{MGS}(m)$ can be treated as a functional proportional to the gradient support, for small β's.

Discussion

Portniaguine and Zhdanov (1999) proposed a way to unfold the physical meaning of mathematical expressions such as (9.4)

- Terms with gradient nearing 0 (or much less than β) have zero contribution.
- Terms where any gradient is present (greater than β) have contributions equal to 1, even with a colossal gradient.

Solutions with sharp boundaries are thus promoted. However, the penalty for considerable gradients (discontinuous solutions) is not disproportionate.

Those stabilizers select the inverse models from a class of models with the minimum volume (or area) of the domain with a causative body of interest (Minimum Support), or with a minimum volume (or area) where the gradient of the model parameters differ from 0 (Minimum Gradient Support).

The straightforward interest of this class of stabilizers is their ability to resolve features that are compact or have sharp boundaries, quintessential objects in geology.

Chapter 10

Trials on synthetic models and methodology establishment

Synopsis

The properties of the Minimum Gradient Support will be tested on synthetic models to assess the ability of the functional to resolve features, and the influence of noise will be tested on simple models. Finally, a methodology will be developed for the inversion of field data.

10.1 Introduction

The synthetic models presented hereafter have been added 3% Gaussian noise. The resistivity values for those models are representative of those in the field. They are meant to represent different situations occurring in the OKvau area.

The final goal of this chapter is to develop a methodology for the application of sharp inversions to the actual field data.

- Firstly, simple models are implemented and the influence of noise is tested.
- Secondly, more complex resistivity structures are considered and a-priori information is used.
- Finally, an synthetic investigation with DC/IP data is solved and the chosen methodology is justified.

10.2 Simple models

First, simple resistivity structures with at most one contrast are considered. The only kind of a-priori information considered here are the weighting factors in the horizontal or vertical axis, respectively favouring vertical or horizontal parameter variations. It is not uncommon in field investigations to have at least some information regarding the rock layers configuration, e.g. based on some outcrops nearby, geological map or drill holes if available. If a geophysicist is looking for the water table level, he might be tuning the inversion parameters for vertical gradients detection.

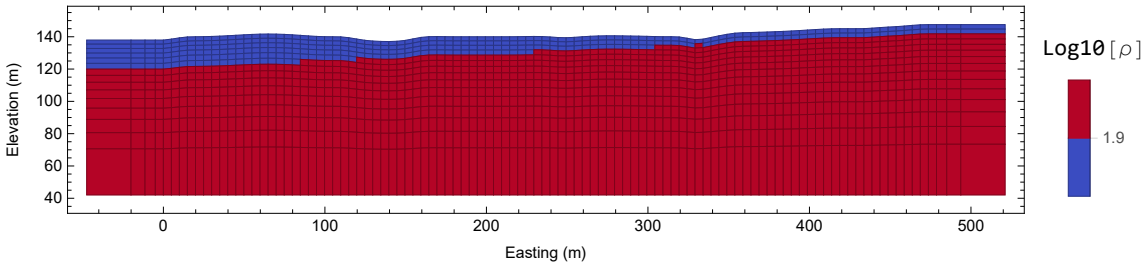

Figure 10.1: **Model I** - represents a conductive soil ($\approx 16\ \Omega$·m) covering a resistive bedrock ($\approx 1260\ \Omega$·m).

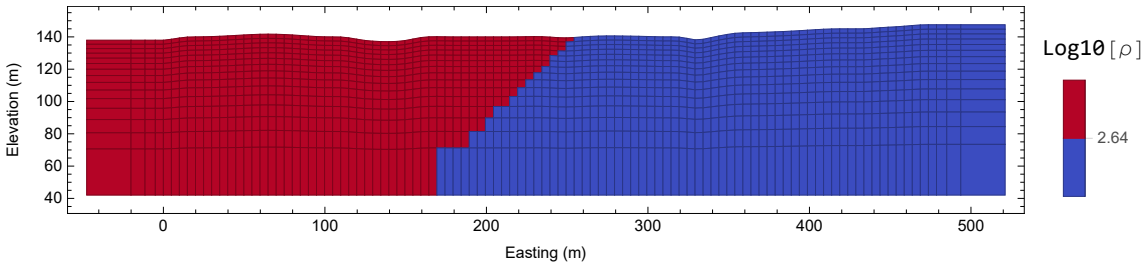

Figure 10.2: **Model II** - represents an oblique contact between two lithologies of different resistivities ($\approx 160\ \Omega$·m and $\approx 1260\ \Omega$·m).

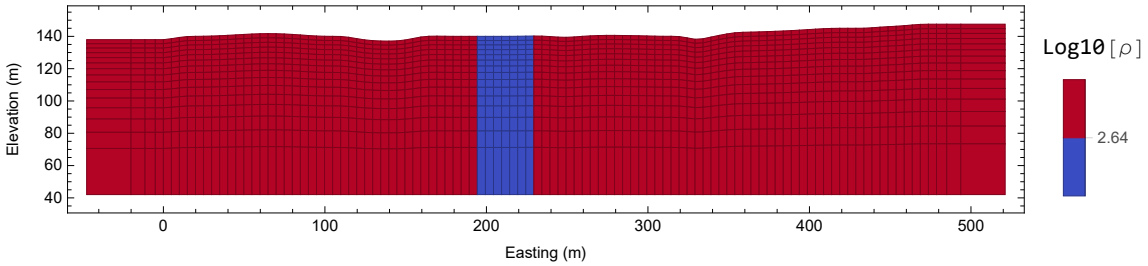

Figure 10.3: **Model III** - represents a vertical fault zone (≈ 160 Ω·m) within a resistive rock (≈ 1260 Ω·m).

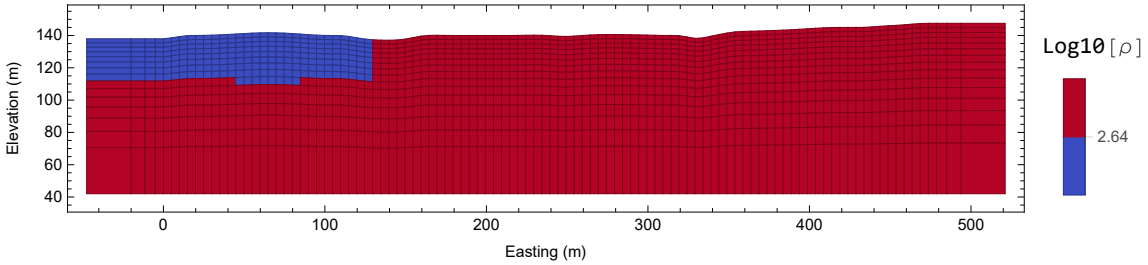

Figure 10.4: **Model IV** - a slab of rock (≈ 160 Ω·m) lies within the top part of a more resistive formation (≈ 1260 Ω·m).

10.2.1 Smooth solutions

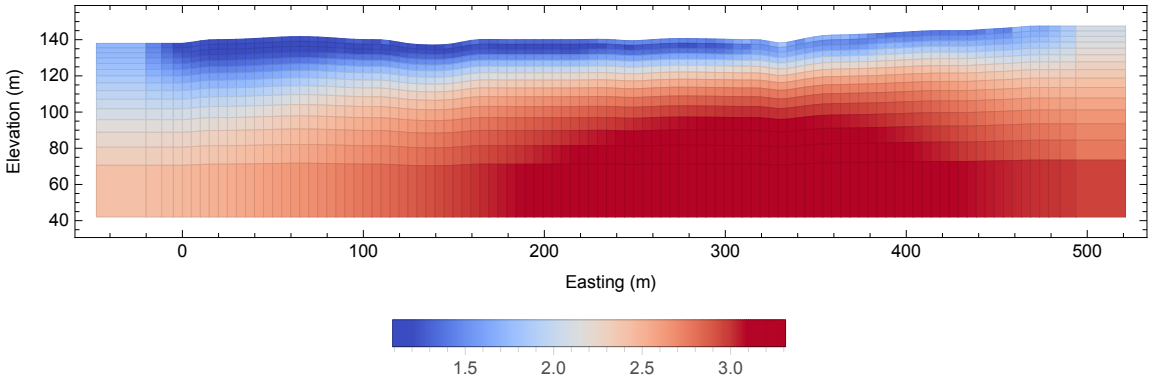

Figure 10.5: **Model I** - Smooth solution when the correct level of noise is picked. H/V anisotropy 3/1.

Comment. The vertical contrast is over-smoothed and could give the impression that an elliptically shaped anomaly is located at depth.

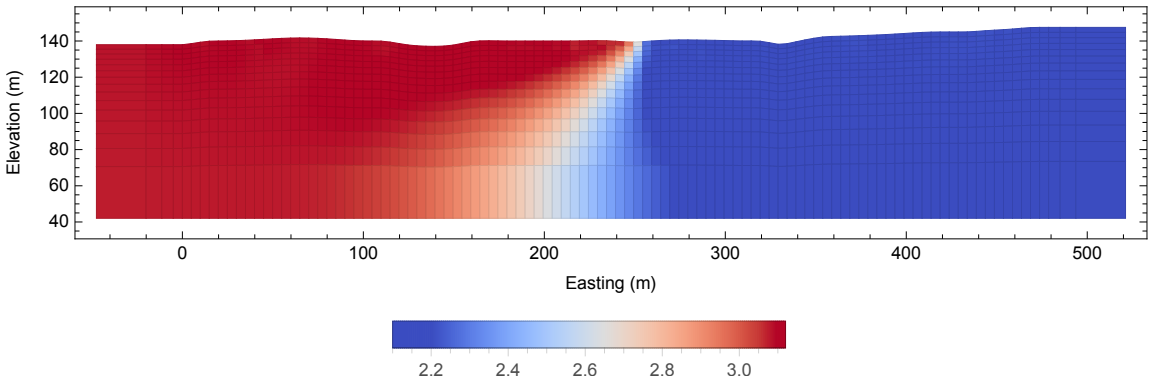

Figure 10.6: **Model II** - Smooth solution when the correct level of noise is picked. The contact zone position is well recovered but is, as expected, spread out due to the smoothing effects. H/V anisotropy 1/1.

Comment. The contact zone is fairly well resolved and the solution is easily interpretable.

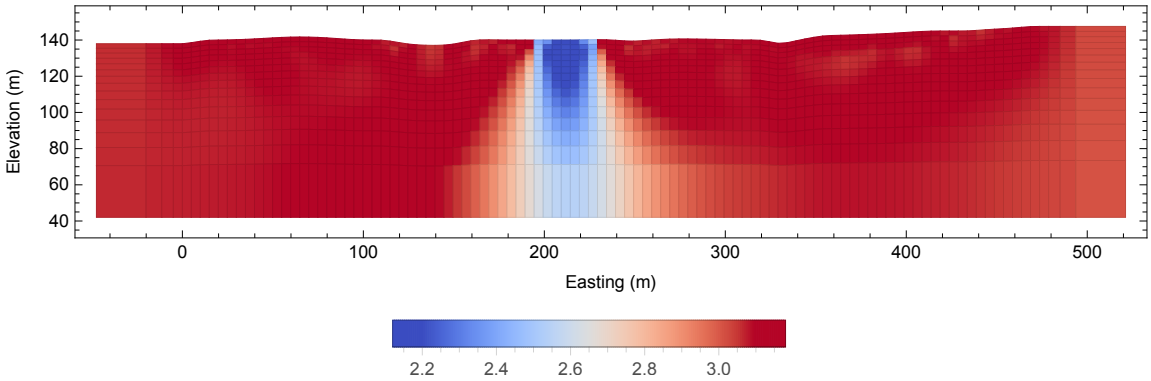

Figure 10.7: **Model III** Smooth solution when the correct level of noise is picked. H/V anisotropy 1/2.

Comment. The contrasts defining the faults zone are obscured at depth.

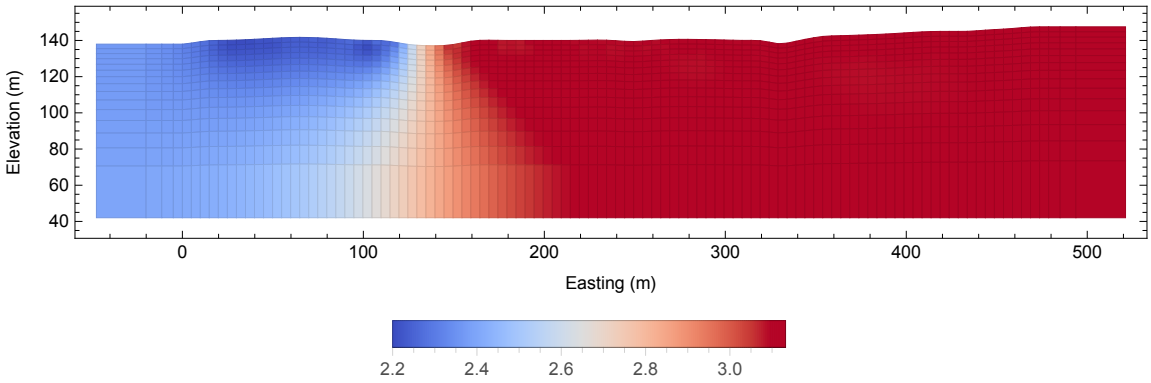

Figure 10.8: **Model IV** Smooth solution when the correct level of noise is picked. H/V anisotropy 1/1.

Comment. The smooth solution can not reproduce the reality in such situations, the resistivity is smoothed out between the less resistive rock slab and the more resistive rock formation.

10.2.2 Sharp inversion : influence of the estimation relative noise level

As mentioned in Chapter 6, no error model could be computed due to time constraint. However, as demonstrated by Binley (1995) and Binley (2015), selecting a correct error level is primordial to recover important features during an inversion. Furthermore, Binley suggests to use the L1-norm which is less sensitive to large data outliers when no error model is available.

Correct estimation

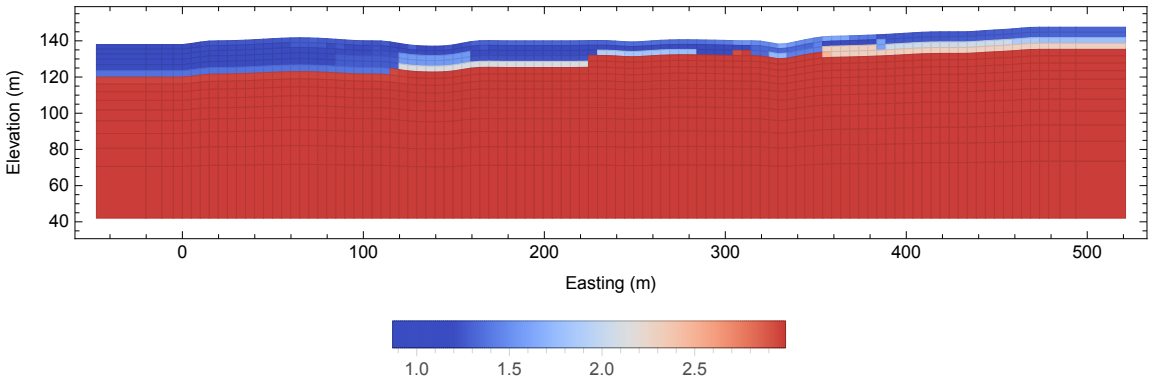

Figure 10.9: **Model I** - Solution for $\beta = 55{\times}10^{-4}$ with H/V anisotropy 3/1. Noise level correctly estimated at 3 %.

Comment. Model I was recovered using different weight for the horizontal and vertical contrast, respectively 3 and 1. This means that the solution should converge towards a "flat" model. This is the same as adding a-priori information, as the user pre-supposes that the contrast will be vertical. The solution then converges towards an good replica of the true model. Inversely, the smooth solution fails to reproduce the reality, even when implemented with the same horizontal to vertical ratio. When no a-priori information is provided, the MGS approach still converges towards a model with a vertical contrast more or less correctly located in the surface, but without the anisotropy, several horizontal resistivity gradients occur over the region. This model exhibits the importance of the prior knowledge during the inversion process.

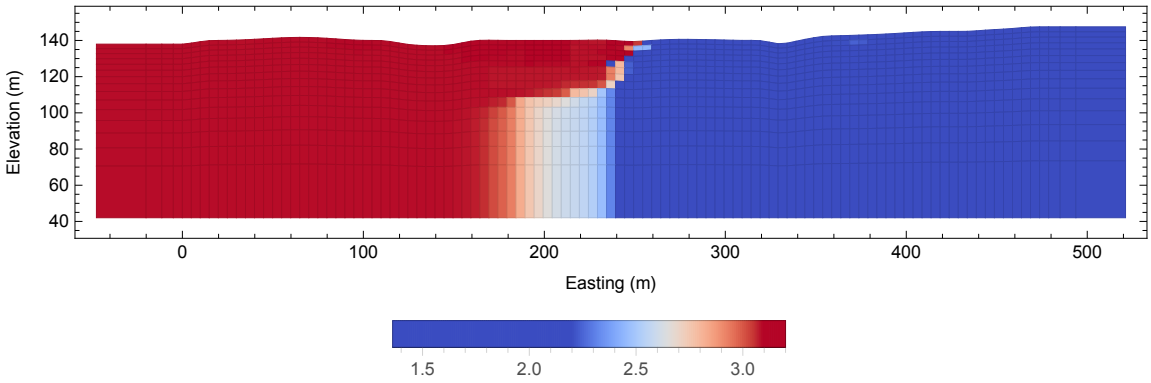

Figure 10.10: **Model II** - Solution for $\beta = 8{\times}10^{-4}$ with H/V anisotropy 1/1. Noise level correctly estimated at 3 %.

Comment. The resistivity gradient is well recovered until some depth where the effect of sensitivity and increasing cell size begin to express itself.

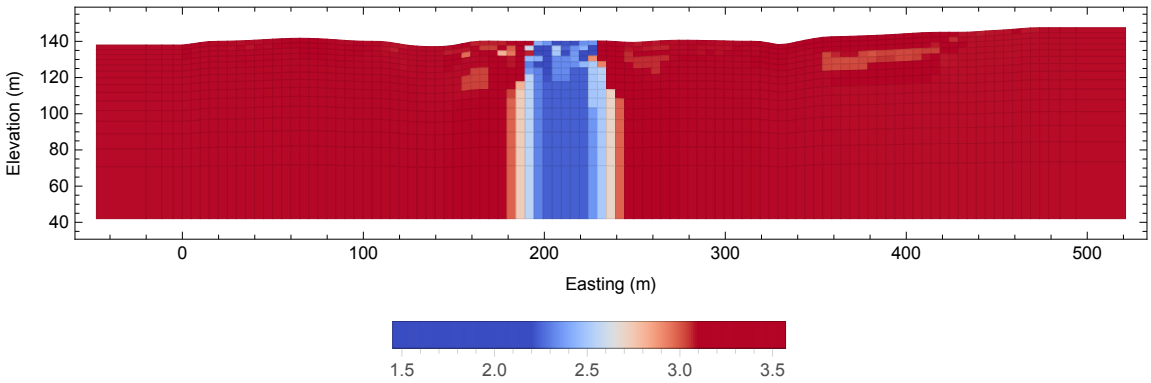

Figure 10.11: **Model III** - Solution for $\beta = 8{\times}10^{-4}$ with H/V anisotropy 1/2. Noise level correctly estimated at 3 %.

Comment. The solution of this model presents small artefacts near the surface, close to the contrasts zones. Contrarily to the smooth solution, the MGS model only has vertical gradient around the fault zone and the correct resistivity value is resolved for the complete depth - making the fault interpretation easier. Adding anisotropy favouring vertical structures, the horizontal contrast along the borders of the fault zone are sharply resolved and the solution becomes even more alike to the true model.

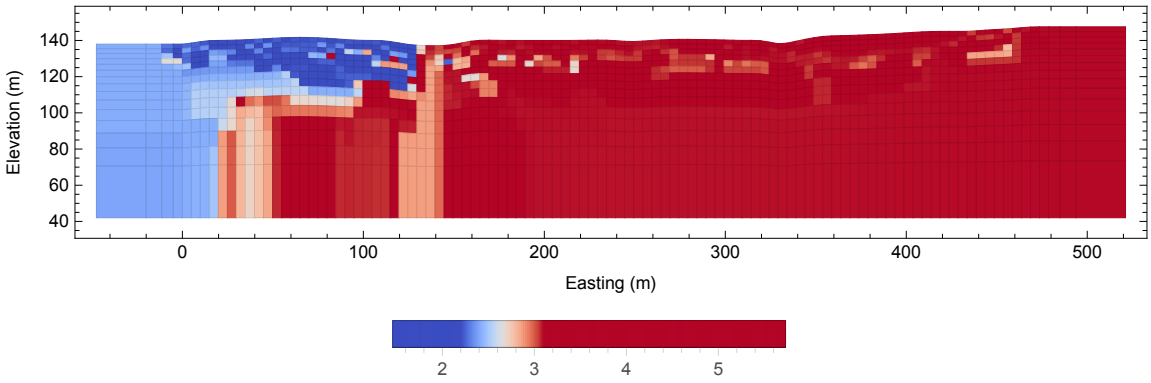

Figure 10.12: **Model IV** - Solution for $\beta = 1\times10^{-4}$ with H/V anisotropy 1/1. Noise level correctly estimated at 3 %.

Comment. The small value of the focusing parameter provoked the apparition of numerous small artefacts in the region of the slab. It also fails to resolve the vertical contrast at the bottom of the less resistive object, but this issue can be resolved by using a higher H/V anisotropy ratio. Contrarily to the smooth solution, it allows the interpreter to guess that the less resistive zone in the west is due to some kind of rock slab.

Under-estimation effect

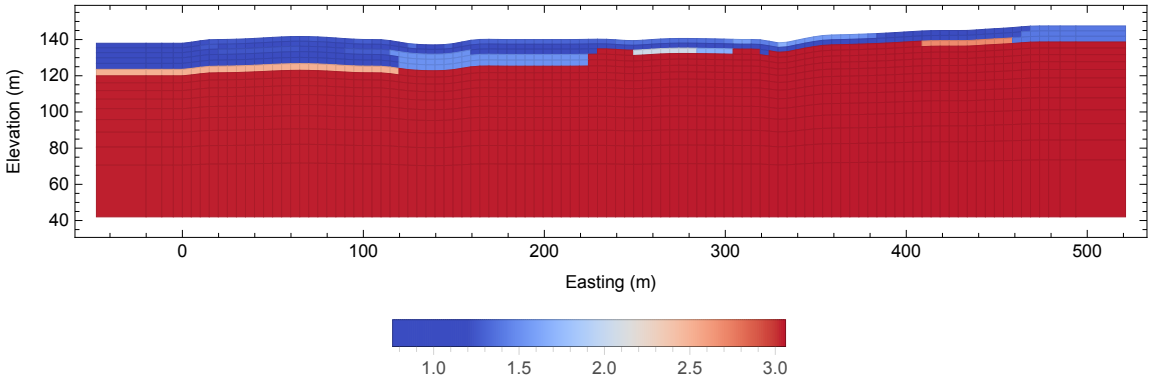

Figure 10.13: **Model I** - Solution for $\beta = 55\times10^{-4}$ with H/V anisotropy 3/1. Noise level under-estimated at 1 %.

Comment. In this specific case, under-estimating the error level does not have detrimental effects.

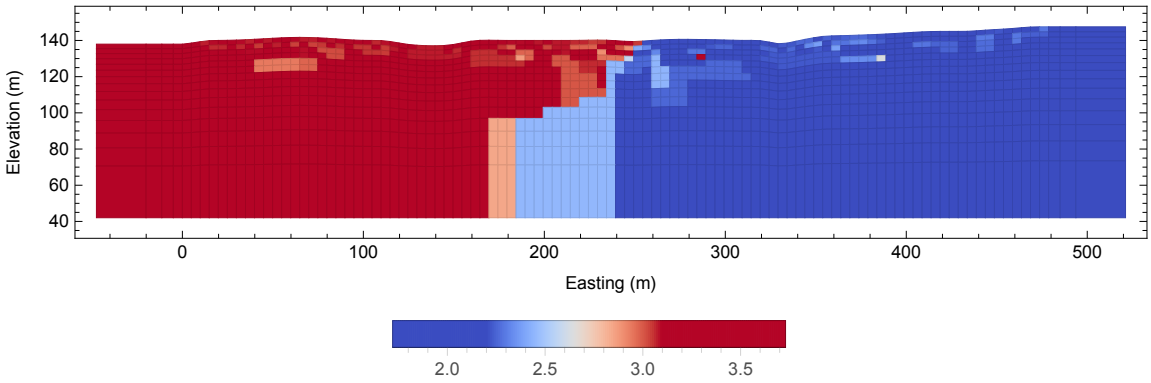

Figure 10.14: **Model II** - Solution for $\beta = 8{\times}10^{-4}$ with H/V anisotropy 1/1. Noise level under-estimated at 1 %

Comment. Numerous sharp artefacts appear near the surface and some model parameters have an elevated resistivity value.

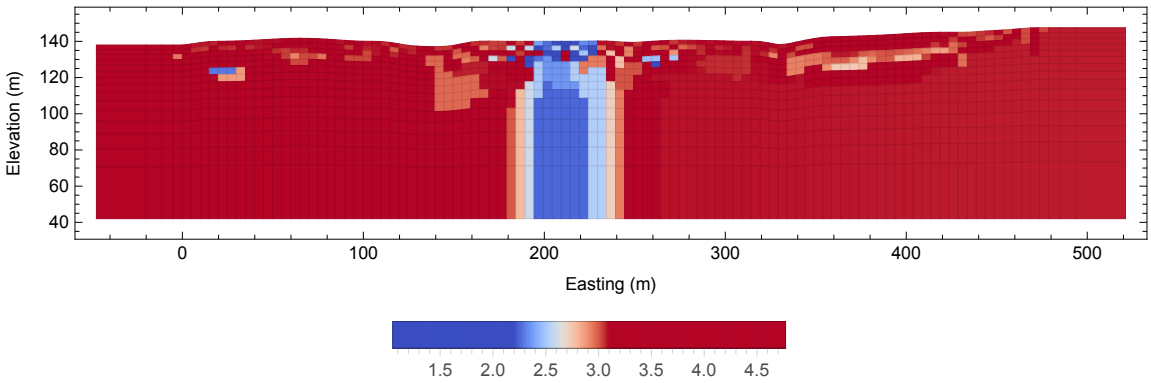

Figure 10.15: **Model III** - Solution for $\beta = 8{\times}10^{-4}$ with H/V anisotropy 1/2. Noise level under-estimated at 1 %.

Comment. The observations are similar to that of the Model II (Figure 10.14).

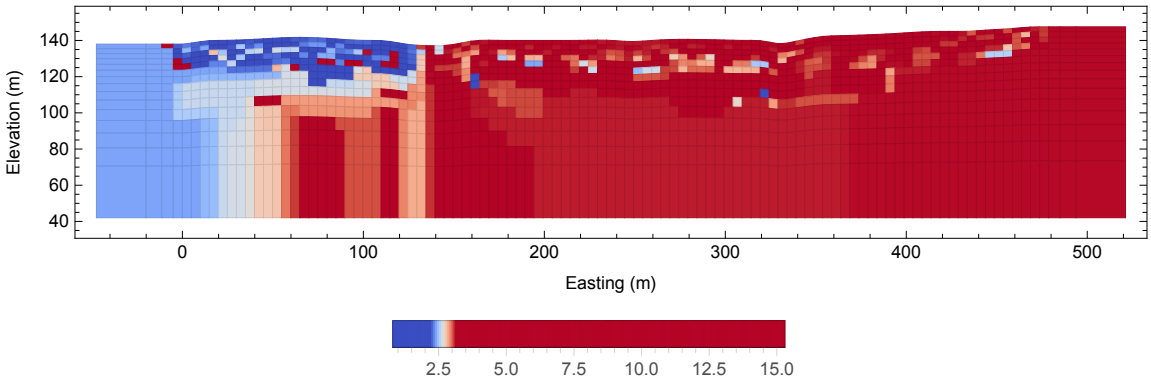

Figure 10.16: **Model IV** - Solution for $\beta = 1{\times}10^{-4}$ with H/V anisotropy 1/1. Noise level under-estimated at 1.5 %.

Comment. Similarly to the last two models, artefacts and elevated resistivity values are computed. It seems that the effect is exacerbated for small β values.

Over-estimation effect

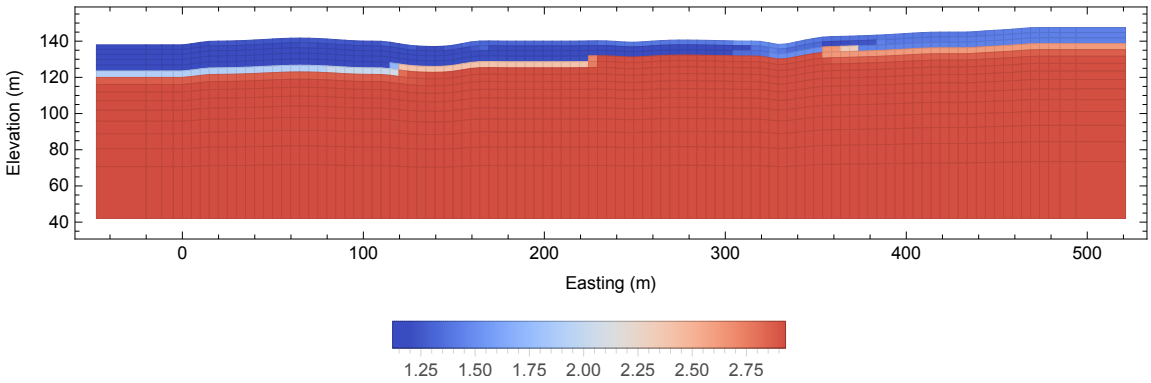

Figure 10.17: **Model I** - Solution for $\beta = 55{\times}10^{-4}$ with H/V anisotropy 3/1. Noise level over-estimated at 5 %.

Comment. The solution is faithful to the original model, although the resistivity values of the underlying rock are smaller than what they really are.

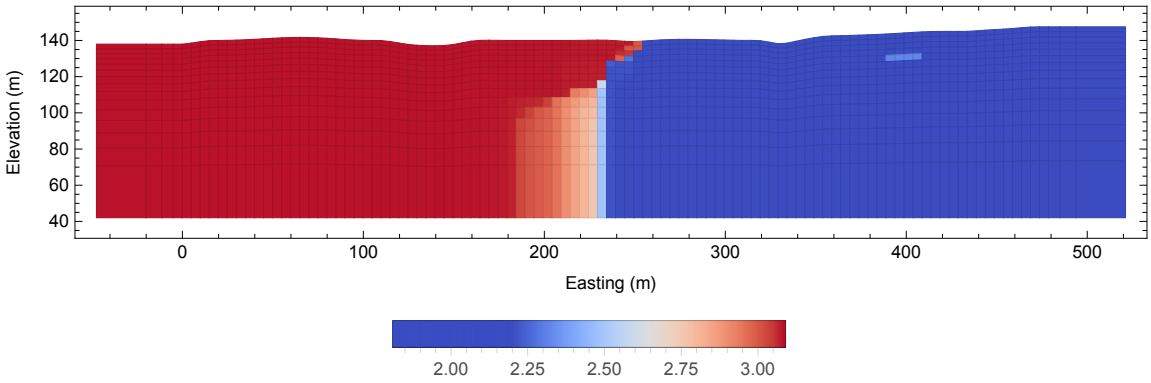

Figure 10.18: **Model II** - Solution for $\beta = 8{\times}10^{-4}$ with H/V anisotropy 1/1. Noise level over-estimated at 5 %.

Comment. The contrast fade out with depth rapidly. The maximum resistivity value is once again diminished.

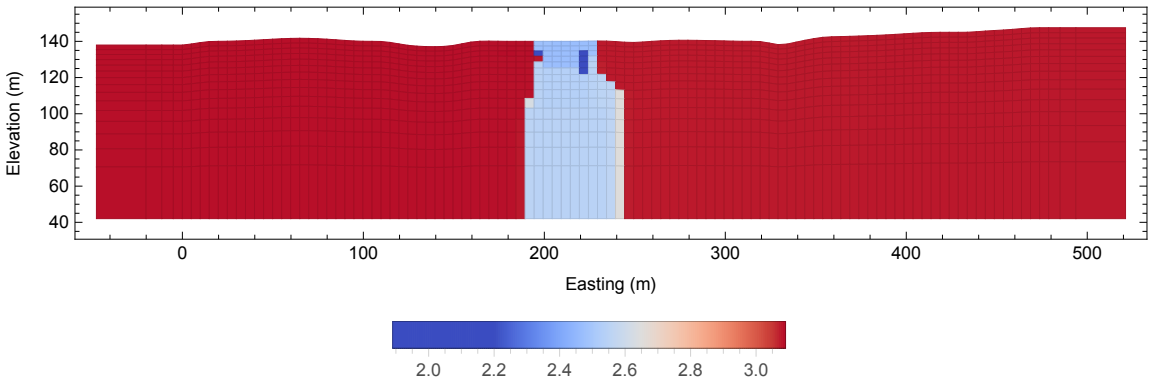

Figure 10.19: **Model III** - Solution for $\beta = 8{\times}10^{-4}$ with H/V anisotropy 1/2. Noise level over-estimated at 5 %.

Comment. The conductive rock slab horizontal contrasts are well resolved and small conductive artefacts are accounted for in the subsurface.

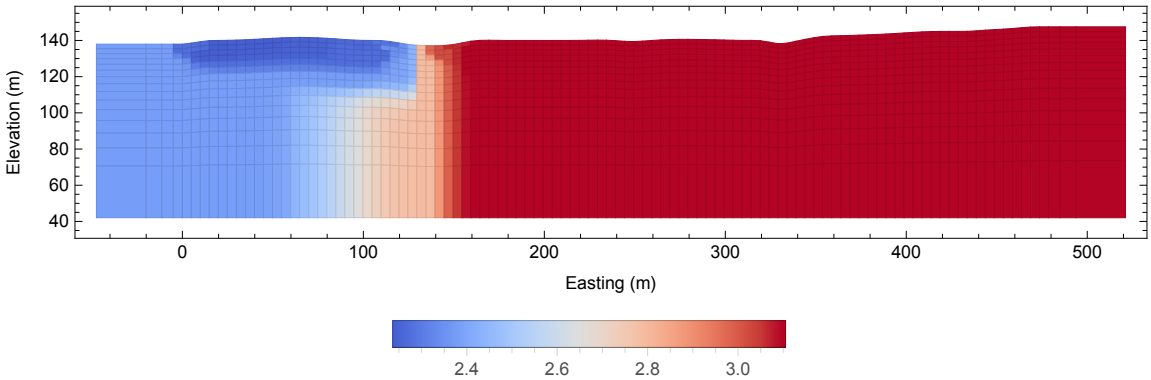

Figure 10.20: **Model IV** - Solution for $\beta = 1{\times}10^{-4}$ with H/V anisotropy 1/1. Noise level over-estimated at 5 %.

Comment. This solution does not present any detrimental artefacts at the cost of having the high resistivity smoothed out below the conductive rock slab.

Discussion

Those four first models are quite simple and not truly realistic. During field investigations, geophysicists are more likely to encounter more complex subsurface structures. The interest here was only to test the behaviour of the MGS approach when facing different situations.

For those examples, the focusing parameter was chosen over a vast array of magnitudes ($< 10^0$) based on the reproduction of the models - it is thus close to the approach of Last and Kubik and Ajo-Franklin et al.. It appears that β values in the order of magnitude 10^{-4} or 10^{-3} are the most adapted. Below this magnitude, inversions tend to become more sensible toward small gradients leading to the formations of small artefacts. It can also fail to converge towards a realistic solution or to reach an acceptable RMS. Larger values tend to produce smoothed features, and are more robust when the contrasts are very sharp.

When the error level is under-estimated, the solution becomes more sensible to small artefacts and there can be a departure in the resistivity values. For an over-estimation, the artefacts disappear but the solution is smoothed and information can be missed. As in the under-estimation effects, resistivity values can be incorrectly computed.

These computations stress out the importance of the choice of the error level and the focusing parameter, to which the sharp inversion is highly sensible. Furthermore, as it will be discussed in the next section the a-priori information greatly helps the model to converge towards an acceptable solution, even when the only information available is the relative orientation of the features.

10.3 Complex models

Resistivity structures with more than one contrasts are now implemented to test the ability of sharp inversions to reproduce the models.

The forward modeling dataset has artificially been contaminated with 3% Gaussian noise.

The MGS inversion for the profile presented in Figure 10.21 fails to resolve interesting features apart from the resistive block in the East. It appears that the regularization fails when there are too many objects to resolve, and this is the situation where a-priori information must intervene.

The smooth solution (Figure 10.22) gives important clues on how different kind of features are resolved. It manages to detect the intermediate resistivity rock slab in the western part of the section, even if the parameter distribution does not correspond with the reality.

The fault zone in the eastern part can be guessed from the resistivity values. However, the magnitude of the two resistive blocks does not match with the true model. The cell enlargement at the left and right borders causes big departures and should only be considered during interpretation under great precautions. Indeed, the subsurface is not covered by the measures since no electrodes are positioned above it. The pointy appearance of the rock formation in the far East of the section is probably due to the smoothing effect of two conductive zones located on its left and top, and to its closeness to the boundaries. Because of this, the global resistivity value for this block is inferior to that of the left block, oppositely to the true model.

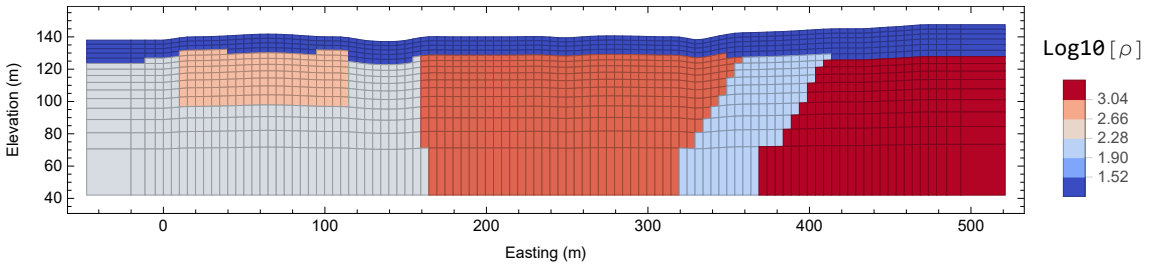

Figure 10.21: **Model V** - Combination of the features of the last 4 models.

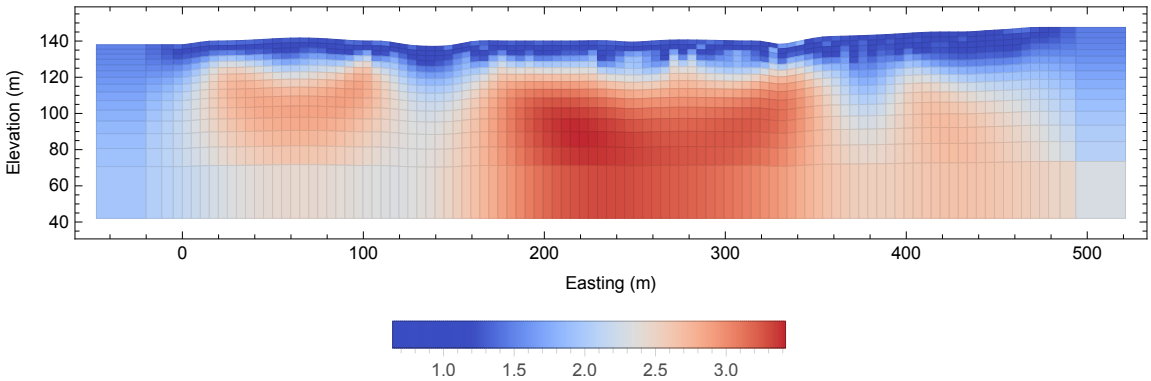

Figure 10.22: **Model V** - Smooth solution (L2-norm) when the noise level is correctly estimated.

This smooth solution will be used as a starting model in a sharp inversion. The assumptions made are :

- The true resistivity distribution of the subsurface occur with sharp contrast.
- The smooth solution is not too far from the reality, and can be trusted in positioning the different causative bodies.

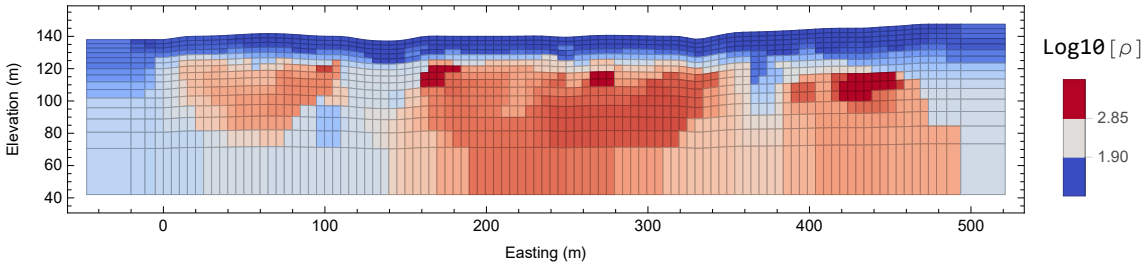

Figure 10.23: **Model V** - Sharp inversion with $\beta = 0.75 \times 10^{-4}$. The noise level was correctly estimated. The smooth solution (Figure 10.22) was used as the starting model. H/V ratio of 3/1 for the first 20 m.

The above solution is closer to the true model than the smooth solution. It is now clear that a rock formation of equal if not superior resistivity is located on the right of a fault separating it from another large resistive block. Furthermore, the obliqueness of the fault is more precisely defined. The MGS inversion has effectively improved the classic smooth model. If a-priori information is available, as drilling logs, the starting model based on the smooth solution can be tuned to further improve the solution.

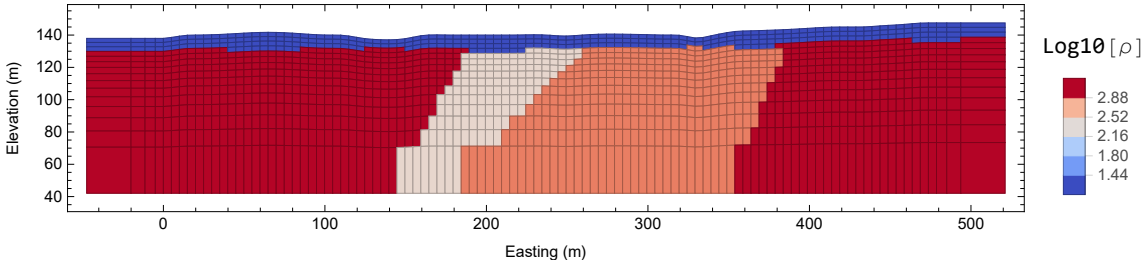

Figure 10.24: **Model VI** - Contacts between lithologies of different resistivities.

In order to further test the influence of the smooth solution as a starting model, it will be applied to Model VI (Figure 10.24). In order to compute the smooth solution, the H/V ratio was set to 3 on the first 10 meters, and to 1/4 below, because for example, near-vertical contact geometries have been observed on surface outcrops and allows the user to infer vertical contacts extending at depth.

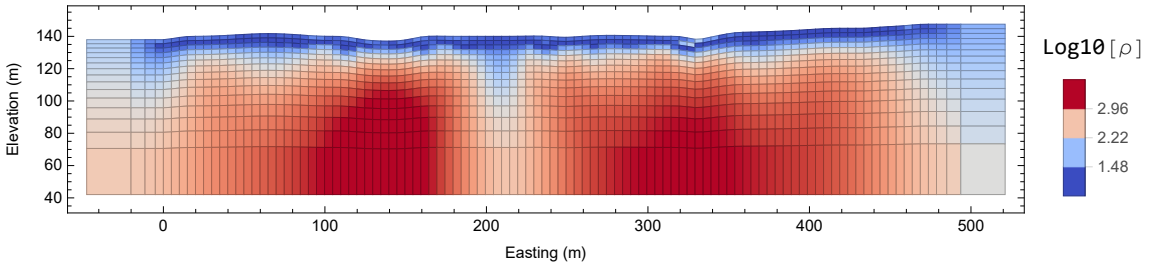

Figure 10.25: **Model VI** - Smooth solution (L2-norm) when the noise level is correctly estimated.

The solutions suffer from the same issues as for Model V. Highly resistive blocks are not interpolated towards the edge and some contacts can not be interpreted. The first issue is not a real problem *per se*, since as mentioned before, it should not be looked upon as representative. The contact along the two lithologies imbricated in the middle of the section is not well resolved. Depending on the aim of the investigation, it can be problematic.

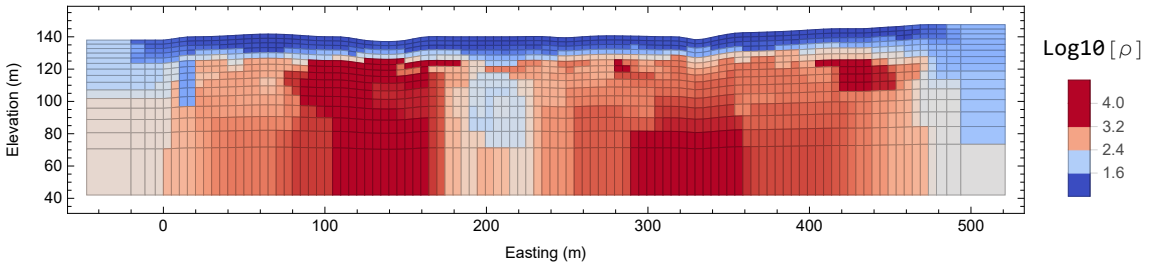

Figure 10.26: **Model VI** - Sharp inversion with $\beta = 0.8 \times 10^{-4}$. The noise level was correctly estimated. Averaged values of the smooth solution (Figure 10.25) was used as the starting model. H/V ratio of 3 for the first 20 m and 1/1 below.

The sharp inversion is a slight improvement since it is more close to the geometry of the true model, but is still hard to interpret. The obliqueness of the contacts is not resolved. Since the MGS approach is conditioned by the smooth solution, and the latter fails, it is logical that some features can not be resolved. However, if alternative a-priori information is available, the starting model could be improved and the sharp inversion could produce a different output.

Discussion

Those two models aimed to reproduce some of the geological features found in the OKvau area. To ensure convergence when using a sharp inversion in complex models, a-priori information must be used. When none is available, Occam's solution becomes useful. The MGS approach can then improve the image obtained, but is conditioned by the a-priori information. A simple type of constraint to apply to the inversion when few information is available is the anisotropy. The geometry of the subsurface is often pre-determined based on the geological map or direct outcrops observations, and it can help the solution to converge towards more realistic models.

Those experiments also demonstrate that the value of borders cells should not be interpreted, and that sometimes the inversion can not resolve all the features of the subsurface. It must be stressed out that the inversion is merely a mathematical procedure producing an array of values that satisfies an algebraic criterion.

The β value was chosen over the reproduction of the true model features, since in this special case, the user *knows* what is the true resistivity distribution. This approach conciliates with Blaschek et al. suggestion : scanning through an array of values and selecting the one that produces a model corresponding with the a-priori information.

However, for real-life cases, the true model is obviously *not known* and a-priori information can be limited or of low value. Those two synthetic cases, also demonstrate that the solution can be far from the reality, especially for Model VI, whatever the inversion scheme.

10.4 Induced polarization investigation scenario

10.4.1 Smooth solution and starting model construction

To bring to a conclusion the trials on synthetic models, a "real-life" scenario must be tested. The final methodology developed will then be applied to the field data. A synthetic induced polarization investigation, realized with the design explained in Chapter 6 is considered. Some drill logs and geological map are available for the area. Furthermore, a petrophysics study of the gathered drill samples was realized and provided several galvanic parameters of the rock. During the choice of the focusing parameter, it will be considered that the true model is unknown.

The aim of this imaginary investigation is the same as this thesis, characterizing a gold deposit linked to chargeable sulfide minerals at some diorite/hornfels contact. As can be seen on Figure 10.27 and Figure 10.28, the main chargeability features are located within a low

resistivity contact zone between a dioritic apophysis and a hosting sedimentary sequence. At the right end of the profile, a resistive siltstone formation is present and minor mineralization occurs at the contact sandstone/siltstone. Furthermore, a small chargeability feature is located near the surface, to test the influence of such bodies during the inversion process. As before, the data was contaminated by a 3% Gaussian noise component.

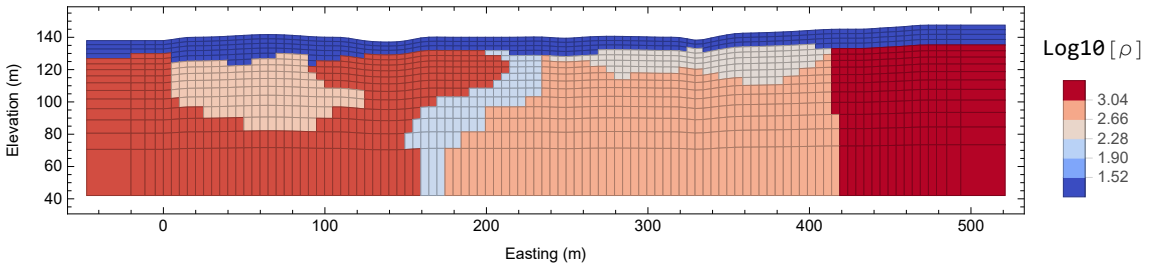

Figure 10.27: Resistivity model for the scenario.

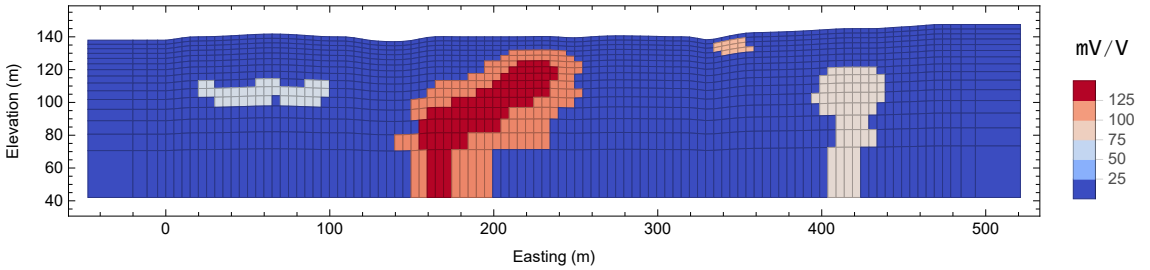

Figure 10.28: Chargeability model for the scenario.

From the previous trials on synthetic models, it was made clear that the a-priori information was the most preponderant parameter to implement in the MGS approach. The aim is then to construct a starting model for the sharp inversion based on the smooth one. Taking into account the dependency of the chargeability towards the resistivity model, the smooth resistivity solution is first computed and used to build the chargeability model.

The methodology to obtain the final results is subdivided into 6 operations:

1. Computation of the resistivity smooth solution.
2. From point 1, interpretation of the results based on the a-priori information and construction of a resistivity starting model.
3. Using the starting model of point 2, computation of the chargeability solution.

4. Based on the results of point 3 and the a-priori information, interpretation of the chargeability distribution and eventual adjustment of the resistivity model computed in point 2.

5. The model established in points 2 or the one adjusted from point 4 is used as a reference model during the computation of the DC final smooth solution. Different weights can be attributed to the model parameters according to the boreholes position.

6. The resistivity solution of point 5 is finally used as the starting model for the MGS inversion for a range of β values.

Operation 1 - smooth solution. For starters, the smooth resistivity solution is computed. Since the IP model is dependent on the resistivity distribution, the latter will be first inverted and a starting resistivity model will be defined based on the smooth solution and the a-priori information. The simplest solution is looked for. The L2-norm is used and no anisotropy is implemented. If the error model was not estimated during the investigation, a common mistake would be to under-estimate the error level of the data. For this synthetic case, the noise level was slightly under-estimated at 2.5%. The result is displayed in Figure 10.29

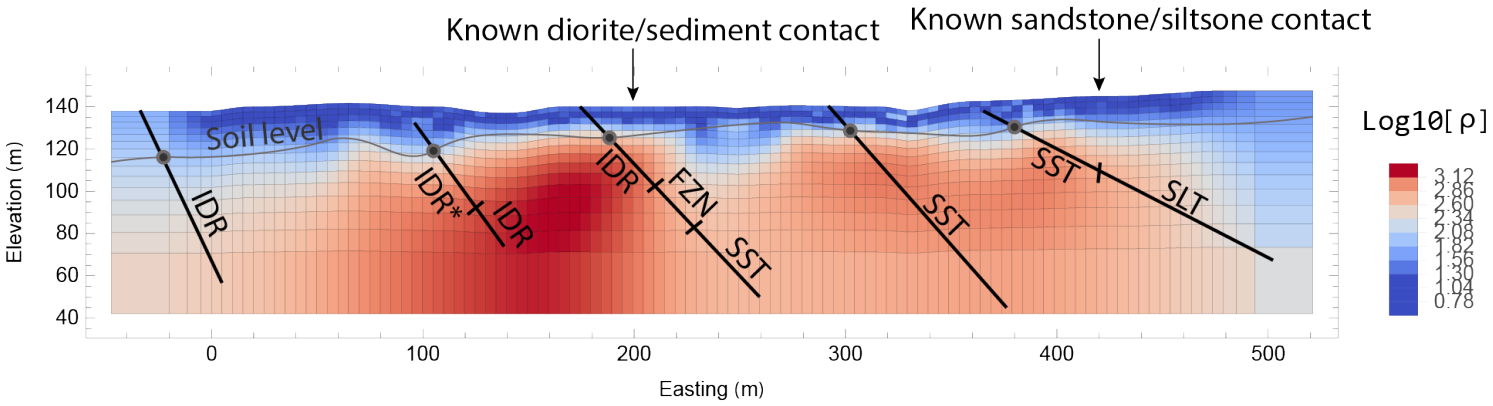

Figure 10.29: Scenario's resistivity smooth solution with superimposed drill logs data and geological knowledge. IDR = diorite, IDR* = altered diorite, FZN = fault zone, SST = sandstone, SLT = siltsone.

Operation 2 - first interpretation. The smooth resistivity solution will now be used in combination with the drill logs data to construct a starting model to then invert the IP data.

- **Soil** - The soil level can easily be interpolated on the profile based on the resistivity values and the drill logs data.
- **Borders resistivities** - Knowing that inversions tend to hide resistive features at the borders, and having direct observations of rock formations at those places, one can safely implement resistivity values corresponding to those formations in the starting model.
- **Fault zone** - based on the computed low-resistivity zone at 240m, the drill hole data and some dip information, the fault zone between the diorite and the sandstone is interpolated deeper in the same direction. Furthermore, drill logs revealed the presence of massive sulphides in this zone.
- The diorite and sandstone geometries can be interpolated from the drill logs.

The inferred model relies upon the interpreter skills and the data quality. This is a relatively easy case, where lots of geological information is available.

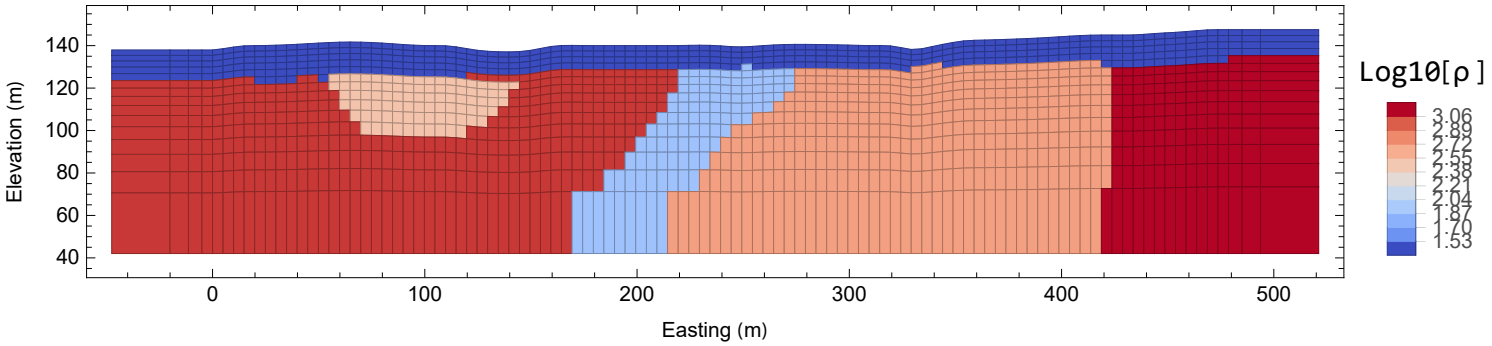

Figure 10.30: Hypothetical resistivity starting model that could have been made by a geophysicist for the considered scenario. It is based on the smooth solution and a-priori information.

Operation 3 - chargeability smooth solution. From this model (Figure 10.30), the IP data will now be inverted. The noise level will slightly be under-estimated at 2.5%. The L1-norm was used to counter the effects of data outliers, and no anisotropy was implemented.

The results are displayed on Figure 10.31.

Chargeability solution. The tip of the chargeable body in the near subsurface is especially well resolved, and its amplitude is not far from reality. The simple interpretation

would be that the main chargeable body is probably linked to the fracture zone between the diorite and the sandstone. The small chargeable feature in the soil layer is well defined. However, there is no trace of the chargeable zones within the diorite alteration zone and at the sandstone/siltstone contacts. It indicates that the inversion process is more sensitive to near-surface chargeability features. Smooth intermediate chargeability artefacts appear all along the section and should not be accounted for.

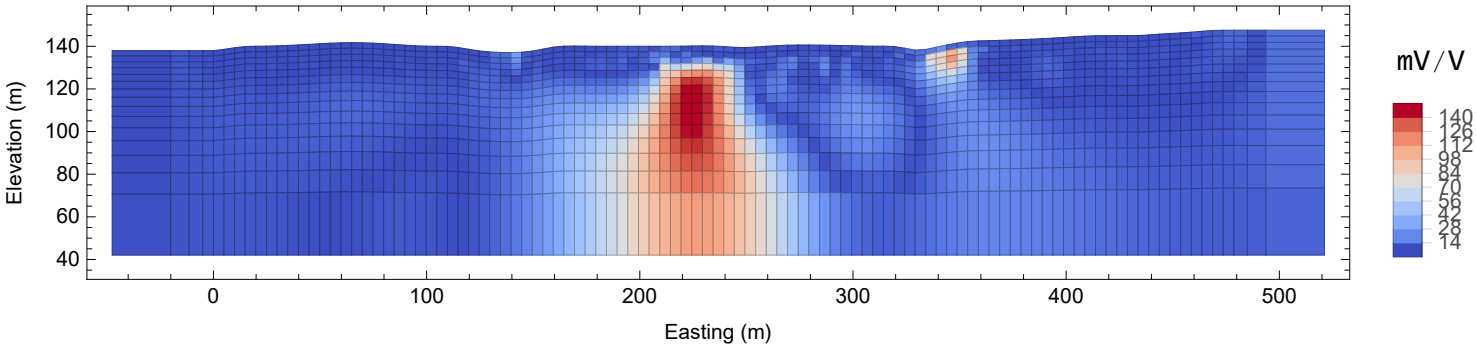

Figure 10.31: Scenario's chargeability smooth solution when Figure 10.30 is used as starting model.

Operation 4 - eventual model adjustment. The IP solution of this inversion will provide information on the causative body. According to petrophysical data, the chargeable minerals are located in the fault zone and are highly conductive. The smooth chargeability solution confirms that the main anomaly is located in this zone. This is why the chargeability model will place the main causative body within the inferred fault zone. A simple interpretation of the geology based on the smooth solution can be sketched (Figure 10.32). The interpreted resistivity is deemed good enough and is not modified.

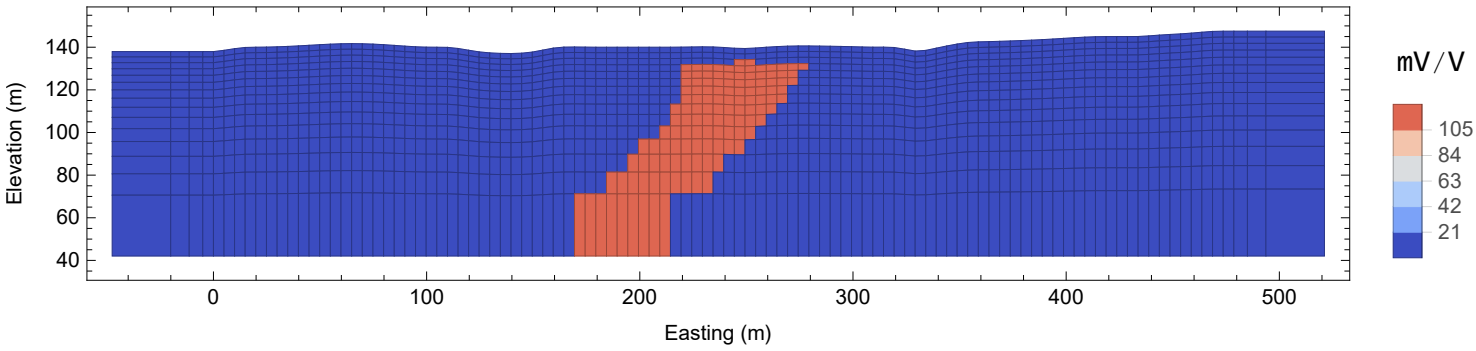

Figure 10.32: Hypothetical chargeability model that could have been made by a geophysicist for the considered scenario. It is based on the resistivity solution and a-priori information.

Operation 5 - final smooth inversion with a reference model. Now that the resistivity and chargeability model are defined, the resistivity one will be used as the reference model for the final resistivity smooth inversion. The point of operations 1 to 5 is to establish a resistivity smooth solution that is the closest to reality, based on all the information available. This smooth solution will then be used as the starting point of the MGS inversion. The result is displayed in Figure 10.34.

It is obvious that the resistivity and chargeability models are over-simplified representation of more complex parameter distribution. Furthermore, there are based on personal interpretation on the geology that can vary from one individual to another. It is thus necessary to allow the final model to evolve from this starting point, while preserving some parameters deemed trusted, i.e. model parameters that are adjacent to boreholes.

In order to do this, a weighting model can be constructed. Each cell of the mesh will be assigned a *weight* proportional to the confidence the user has in the a-priori information his model provides.

Practically, based on the boreholes position, a simple function can be established to attribute decreasing weights to the model parameters as they stray away from the drill line. Based on the a-priori information, the fault zone is a key feature that should be preserved during the inversion. Accordingly, superior weights are attributed to model parameters within that zone. Furthermore, as the mesh borders tend to "fade away" during the inversion, one way to maintain their roughness is to attribute elevated weight on those borders.

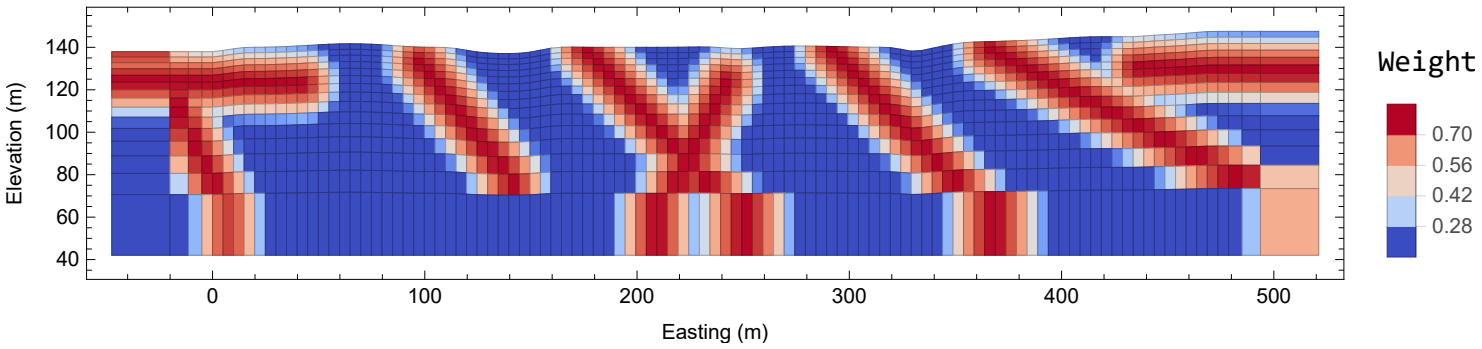

Figure 10.33: Weight distribution used for the smooth inversion of the resistivity using a reference model.

Operation 6 - sharp inversion with a starting model. The resistivity starting model used for the sharp inversion corresponds to the smooth inversion using the reference model. The chargeability starting model is null.

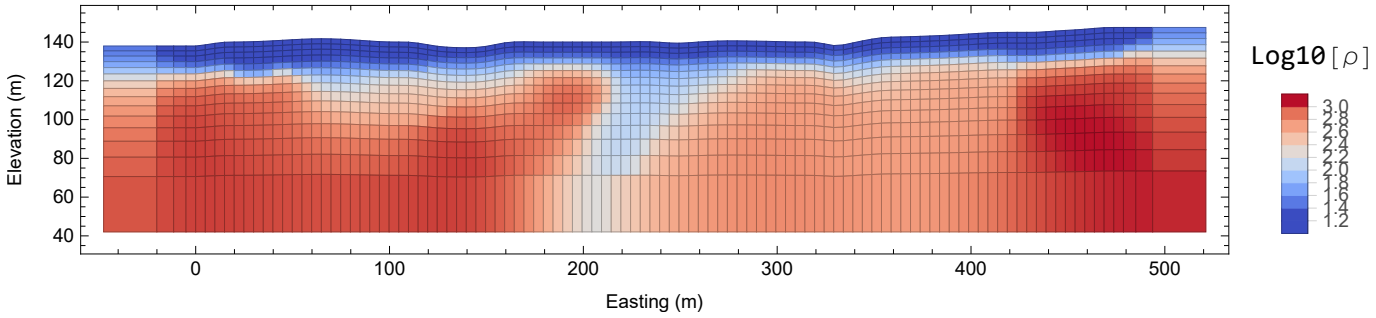

Figure 10.34: MGS resistivity starting model.

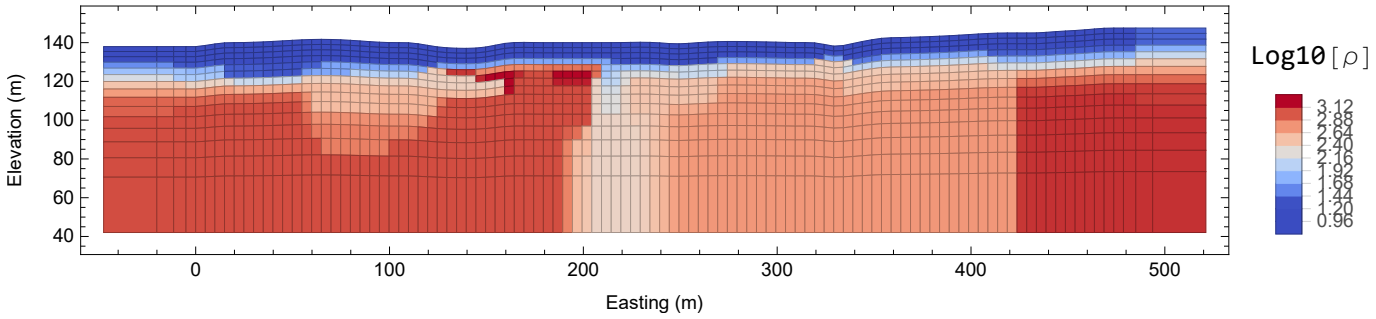

Figure 10.35: Sharp resistivity solution with $\beta = 7 \times 10^{-4}$.

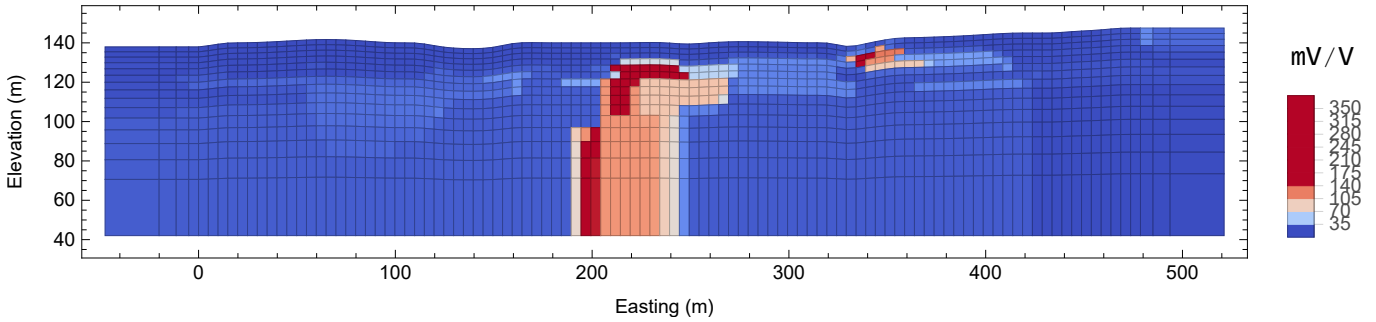

Figure 10.36: Sharp chargeability solution with $\beta = 7 \times 10^{-4}$.

The resistivity solution in Figure 10.35 gives more credit to the actual resistivity structure. The border effect is bypassed and the resistivity magnitudes according to the litho-

logical units are accurate. The hooked appearance of the diorite is not so well depicted. Thus, the fault zone geometry is more vertical than the actual structure.

The chargeability solution in Figure 10.35 faithfully represents the sharp appearance of the mineralized body. Since it depends on the fault zone, it is as well more vertical than it should be. The chargeability magnitudes are greater than they should be, especially at the border of the diorite. It might be an effect of the MGS approach when a strong resistivity contrast is present in the subsurface structure. The small chargeability feature in the soil has been resolved even though its magnitude is superior than the true value. The chargeability features in the diorite alteration and at the contact sandstone/siltstone have been recovered in neither inversion scheme. This might be due to a combination of their low amplitude and closeness to the borders.

The focusing parameter value has been defined based on the resolved features appearance. From a vast array of β values, was chosen the one that produced the best compromise between the presence of many artefacts and an unrealistically rectangular model. The choice is very subjective, based on the user's interpretations.

Discussion

Obtaining a "satisfactory solution" using the MGS approach requires more effort than with the classic smooth scheme. It is also facilitated by the knowledge of a-priori information. When none is available, the smooth solution can be used as a starting model for the sharp inversion. However, when the user trusts the presence of certain features, the MGS approach can tune the smooth solution to resemble the true model.

The choice of the focusing parameter is made based on the appearance of the solution only, thus dependent on the interpreter aptitude to recognize unrealistic geological features.

Based on the trials on synthetic models, a flow sheet is presented on the next page for the computation of IP data using the minimum gradient support approach.

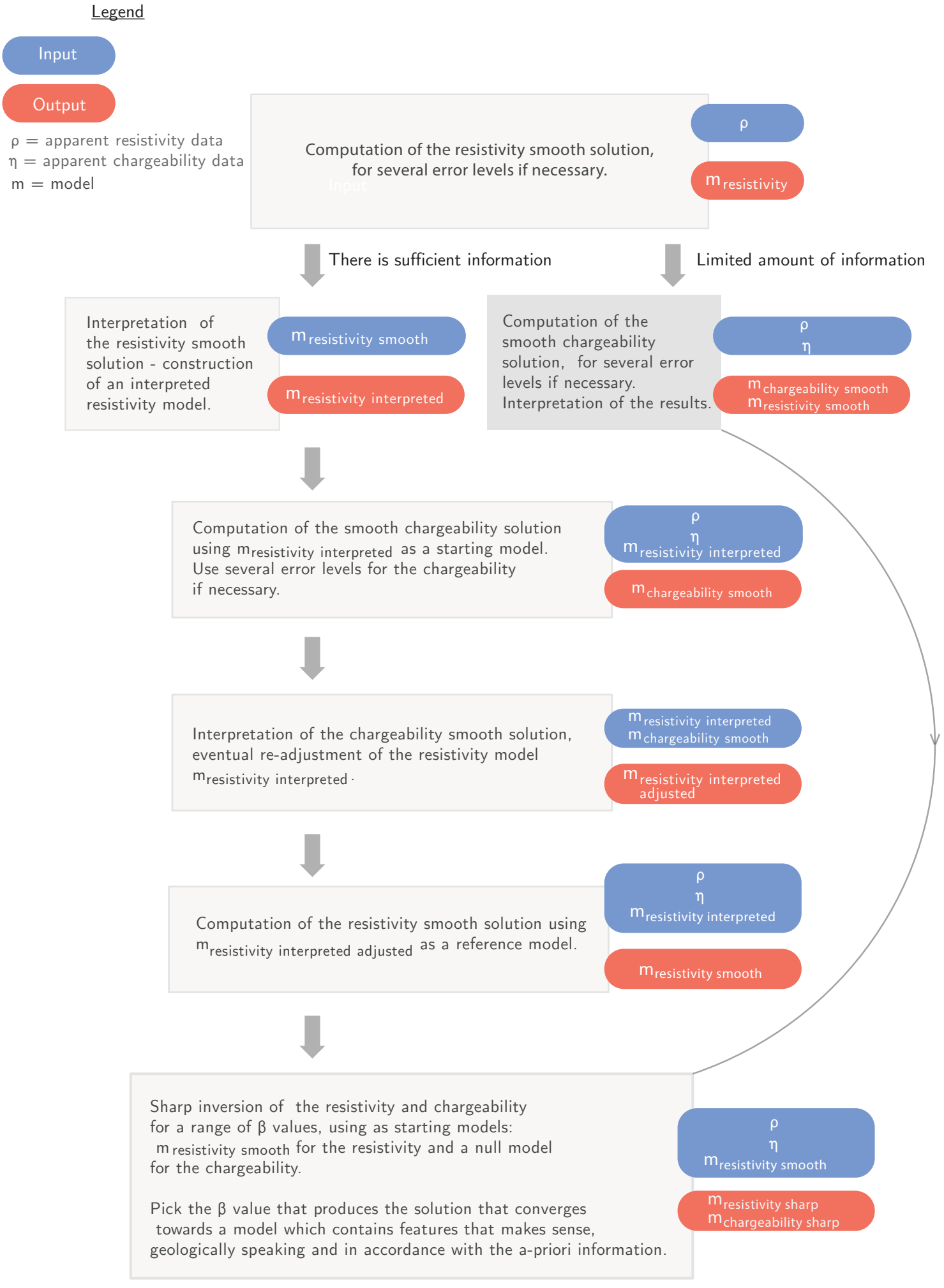
Legend
Input
Output
ρ = apparent resistivity data
η = apparent chargeability data
m = model
Computation of the resistivity smooth solution, for several error levels if necessary.
ρ
m resistivity
There is sufficient information
Limited amount of information
Interpretation of the resistivity smooth solution - construction of an interpreted resistivity model.
m resistivity smooth
m resistivity interpreted
Computation of the smooth chargeability solution, for several error levels if necessary. Interpretation of the results.
ρ
η
m chargeability smooth
m resistivity smooth
Computation of the smooth chargeability solution using m resistivity interpreted as a starting model. Use several error levels for the chargeability if necessary.
ρ
η
m resistivity interpreted
m chargeability smooth
Interpretation of the chargeability smooth solution, eventual re-adjustment of the resistivity model m resistivity interpreted.
m resistivity interpreted
m chargeability smooth
m resistivity interpreted adjusted
Computation of the resistivity smooth solution using m resistivity interpreted adjusted as a reference model.
ρ
η
m resistivity interpreted
m resistivity smooth
Sharp inversion of the resistivity and chargeability for a range of β values, using as starting models: m resistivity smooth for the resistivity and a null model for the chargeability.
Pick the β value that produces the solution that converges towards a model which contains features that makes sense, geologically speaking and in accordance with the a-priori information.
ρ
η
m resistivity smooth
m resistivity sharp
m chargeability sharp

Chapter 11

Data processing and statistical analysis

Synopsis

Thousands of data points have been collected for each profiles. It is necessary to assess their quality and remove eventual outliers before proceeding to the inversion. Some descriptive statistics of the apparent chargeability and resistivity are presented.

11.1 Introduction

In DC/IP investigations, the datasets from the ABEM Terrameter include the position of the injecting and measuring electrodes along the profile layout, the measured voltage V, the resistance R, the different values of IP in mV/V for the 17 IP windows, and the error percentage (computed with the different stacks).

Some operations need to be conducted to obtain the apparent resistivity and apparent chargeability to invert:

- The injected current amplitude I (A) should be close to the value fixed by the user and can be found using Ohm's law, $I = V/R$.
- The geometric factor k is computed using the relationship (5.6).
- The apparent resistivity ρ_a (Ω·m) can then be recovered using the last two results, $\rho_a = k\frac{V}{I}$.

- Let *ipw* be the [1×17] vector containing the 17 IP values for each window and let *ipt* be the [1×17] vector containing the duration of each window. The apparent chargeability M_a is then computed by :

$$M_a = \frac{ipw \cdot ipt}{\sum_{j=1}^{17} ipt_j}, \tag{11.1}$$

  where the operator in the numerator corresponds to the scalar product and the denominator is the total integration interval.

The operations described above are realized for every point of each profile, and will now be analysed in a statistical fashion.

The data will be processed as follows :

1. Removal of noise-contaminated data points, i.e. points with a percentage error above a specified threshold.
2. Removal of bad IP curves data points, i.e. points whose IP curves clearly depart from a gradual decay.

11.2 Noise-contaminated data removal

The error (variance) in % of each point is measured by the stacks during the acquisition. Ideally, it should be equal to 0, but in practice, it can be in the order of a few percent. The removal threshold is 2 %. Above this value, the data points are removed.

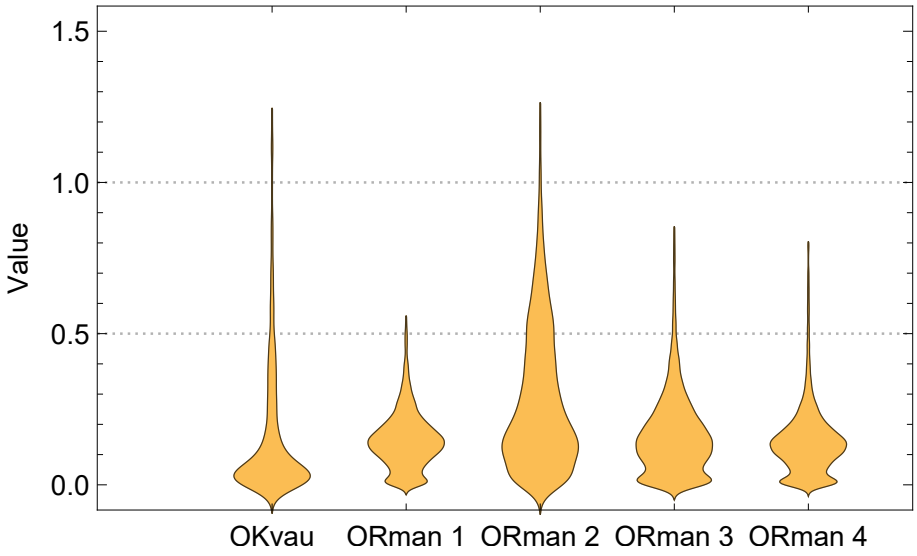

Figure 11.1: Box whisker chart of the variance of the data points of each profile after removing the points exceeding 2 %.

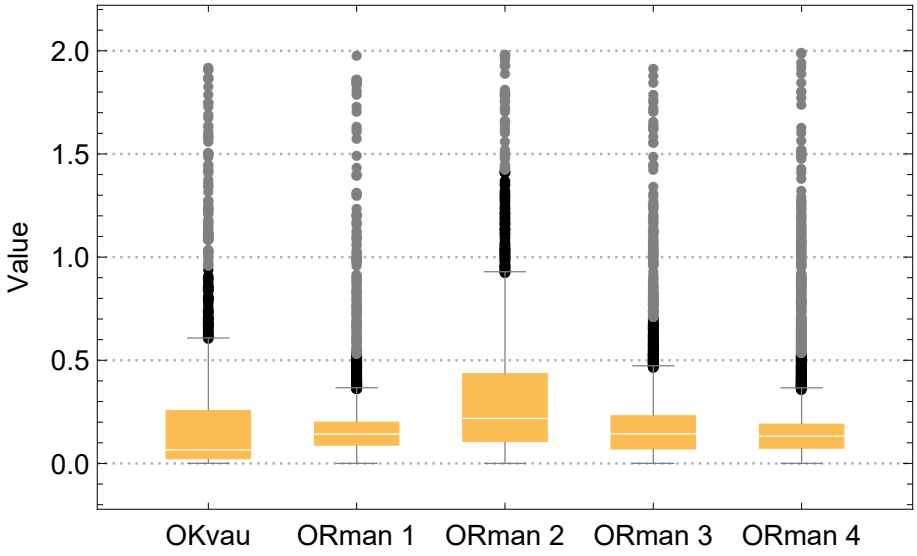

Figure 11.2: Distribution chart of the variance of the data points of each profile after removing the points exceeding 2 %. The near outliers are depicted as the black points and the far outliers as the gray ones.

11.3 Bad IP curves removal

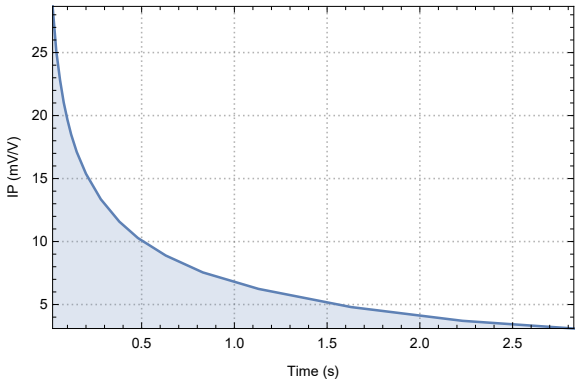

Figure 11.3: Typical IP curve expected from the measurements.

As stated in section 5.3, IP data is susceptible to different kinds of noise and some spurious IP readings need to be eliminated. According to the level of departure from the ideal decay curve (Figure 11.3), data points will be eliminated or not. Mainly 3 kinds of problems, or a mix of those, can occur, due to a combination of phenomena described in subsection 5.2.3:

(a) The curve starts in the positive part of the graph and plunges to the negative part.

(b) The curve begins to decay gradually but unexpectedly starts to rise after some time.

(c) Spurious oscillations occur.

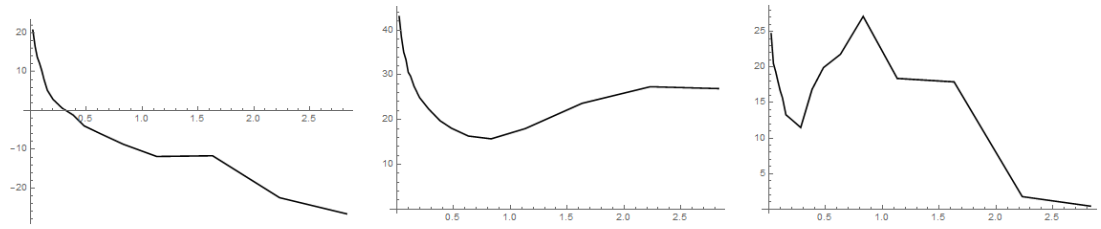

(a) (b) (c)

Figure 11.4: Bad IP curve shapes.

11.4 Apparent resistivity data

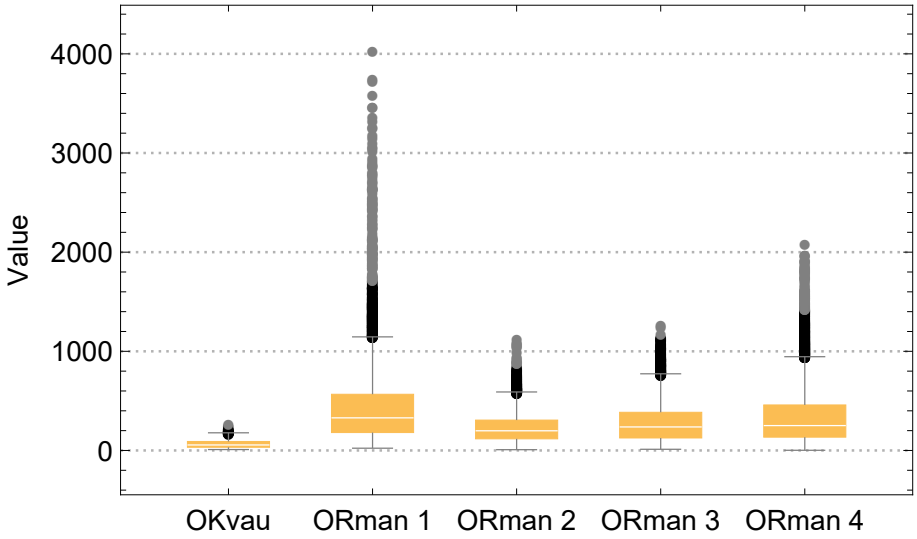

Figure 11.5: Box whisker chart of the apparent resistivity values (in Ω·m) for each profile. The near outliers are depicted as the black points and the far outliers as the gray ones.

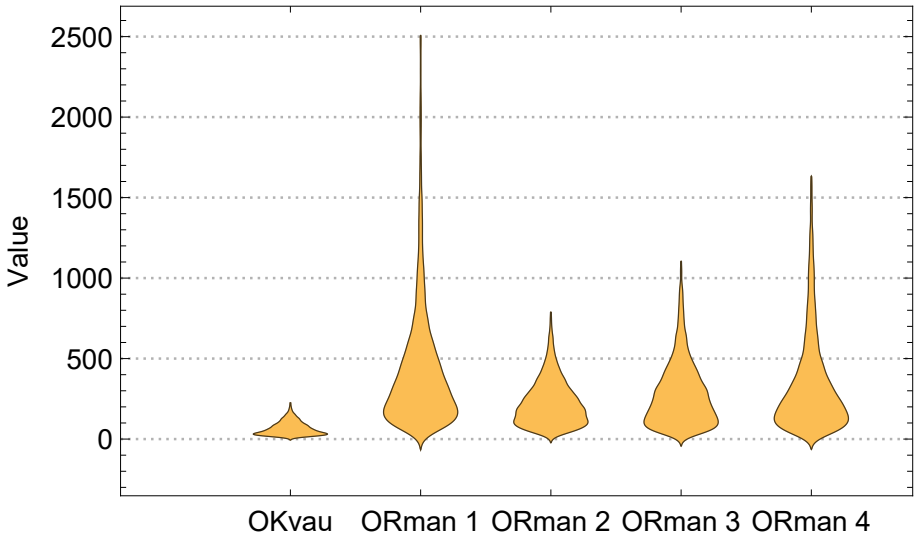

Figure 11.6: Distribution chart of the apparent resistivity values (in Ω·m) for each profile.

11.5 Chargeability data

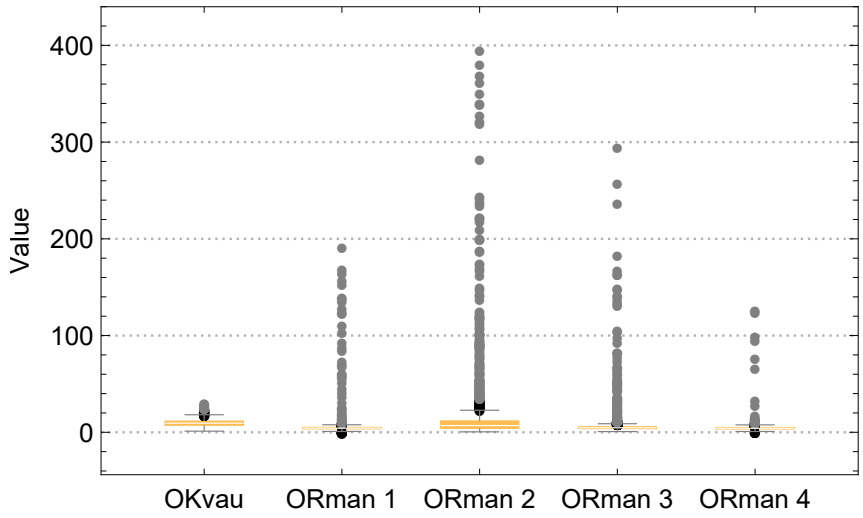

Figure 11.7: Box whisker chart of the apparent chargeability values (in mV/V) for each profile. The near outliers are depicted as the black points and the far outliers as the gray ones.

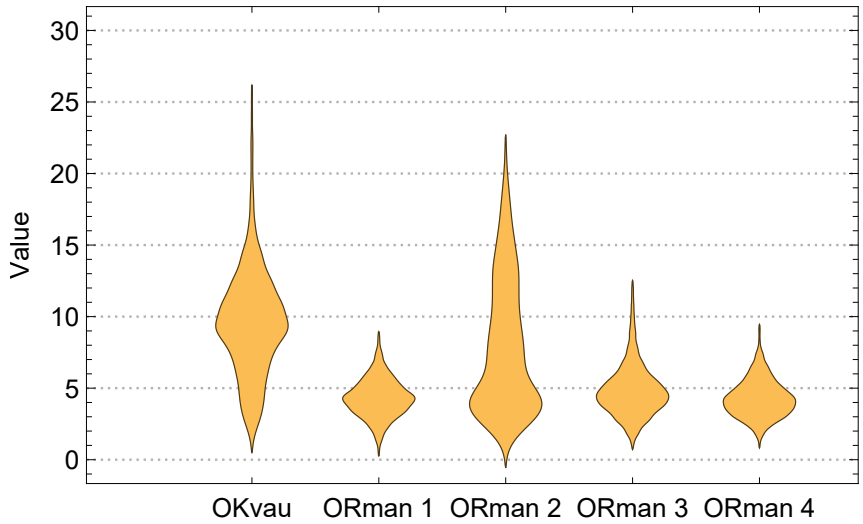

Figure 11.8: Distribution chart of the apparent chargeability values (in mV/V) for each profile.

Conclusion

The data is not contaminated by spurious noise. The variance statistics demonstrates that most of the profiles have 75 % of their variance values below 0.6 %, at the exception of ORman 2 (75 % below 0.9 %).

11.5.1 OKvau calibration line

Associated with low apparent resistivity values and high apparent chargeability data points.

Variance. Out of 2150 initial data points, 100 were removed because they exceeded the variance threshold of 2 %.

IP curves. Out of the 2050 remaining points, 248 points were screened for having a bad IP curve.

15.8 % of the data points was removed from the original dataset, which is quite significant compared to the following profiles. Furthermore, several data points were not measured because of 4 missing electrodes.

11.5.2 ORman 1

Associated with high apparent resistivity values and low apparent chargeability data points.

Variance. Out of 5808 initial data points, 83 were removed because they exceeded the variance threshold of 2 %.

IP curves. Out of the 5725 remaining points, 240 points were screened for having a bad IP curve.

5.5 % of the data points was removed from the original dataset.

11.5.3 ORman 2

Associated with medium to high apparent resistivity values and elevated chargeability data points, with several outliers of great magnitude.

Variance. Out of 7750 initial data points, 116 were removed because they exceeded the variance threshold of 2 %.

IP curves. Out of the 7634 remaining points, 288 points were screened for having a bad IP curve.

5.2 % of the data points was removed from the original dataset.

11.5.4 ORman 3

Associated with high apparent resistivity values and low apparent chargeability data points.

Variance. Out of 7495 initial data points, 95 were removed because they exceeded the variance threshold of 2 %.

IP curves. Out of the 7400 remaining points, 367 points were screened for having a bad IP curve.

6.1 % of the data points was removed from the original dataset.

11.5.5 ORman 4

Associated with high apparent resistivity values and low apparent chargeability data points.

Variance. Out of 7164 initial data points, 106 were removed because they exceeded the variance threshold of 2 %.

IP curves. Out of the 7058 remaining points, 344 points were screened for having a bad IP curve.

6.3 % of the data points was removed from the original dataset.

Chapter 12

Inversion results

Synopsis

The methodology developed in Chapter 10 is applied to the cleaned data (Chapter 11) and the results are interpreted.

12.1 Introduction

The resistivity and chargeability graphics share the same color map, scaled to the values of the OKvau calibration line. The divergent color map chosen follows the recommendations of Moreland (2009).

12.2 OKvau calibration line

The OKvau area is riddled with drills. Lots of information are available (see the figure on the next page).

The resistivity smooth solution is computed using the L1-norm with 2% estimated noise level.

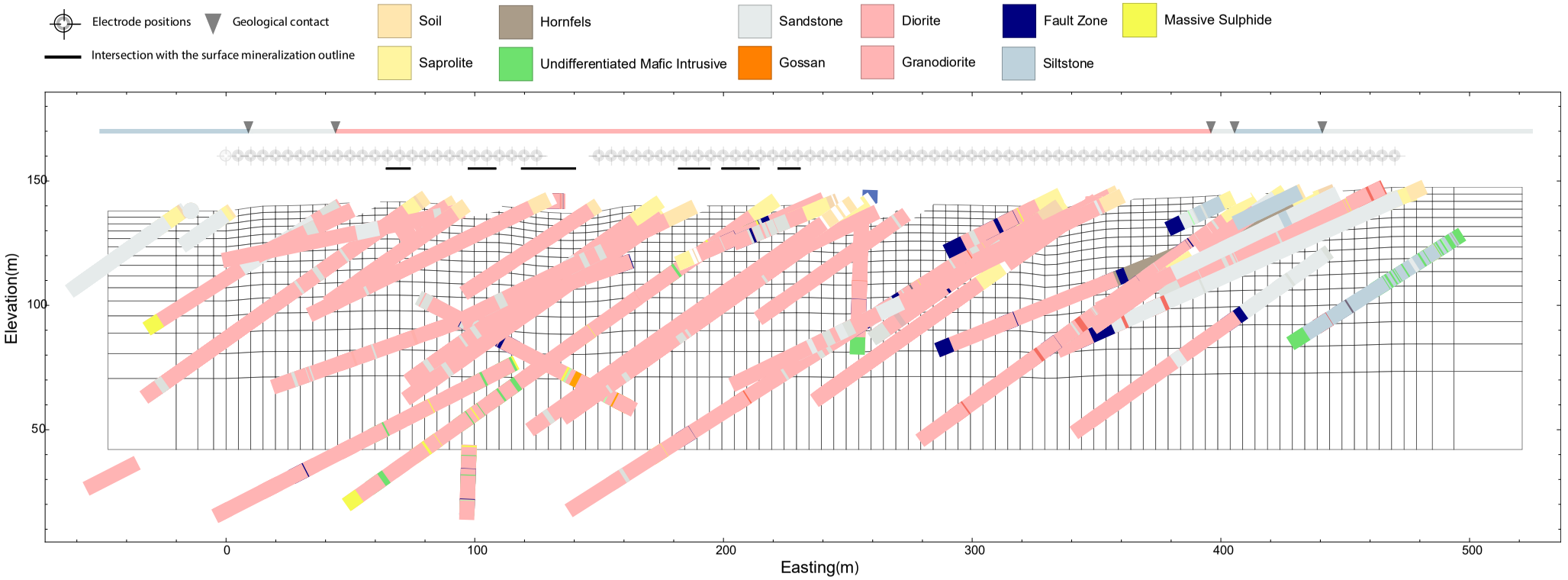
Electrode positions
Geological contact
Intersection with the surface mineralization outline
Soil
Saprolite
Hornfels
Undifferentiated Mafic Intrusive
Sandstone
Gossan
Diorite
Granodiorite
Fault Zone
Siltstone
Massive Sulphide
Elevation(m)
150
100
50
0
100
200
300
400
500
Easting(m)

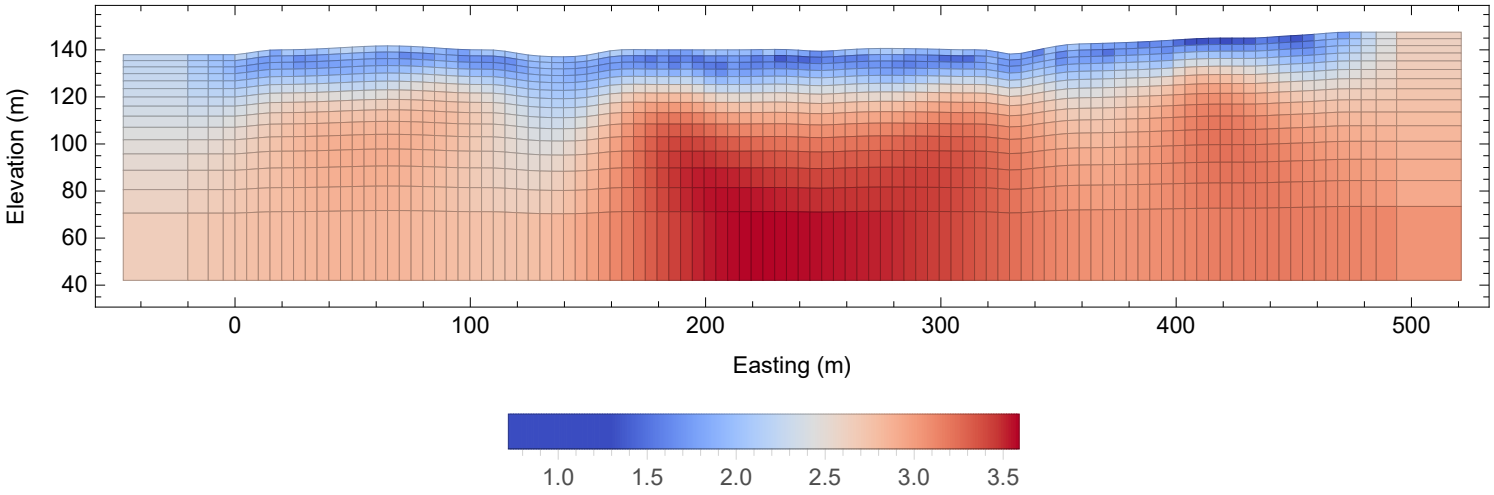

Figure 12.1: OKvau calibration line smooth solution. The values are given in Log_{10} of the resistivity.

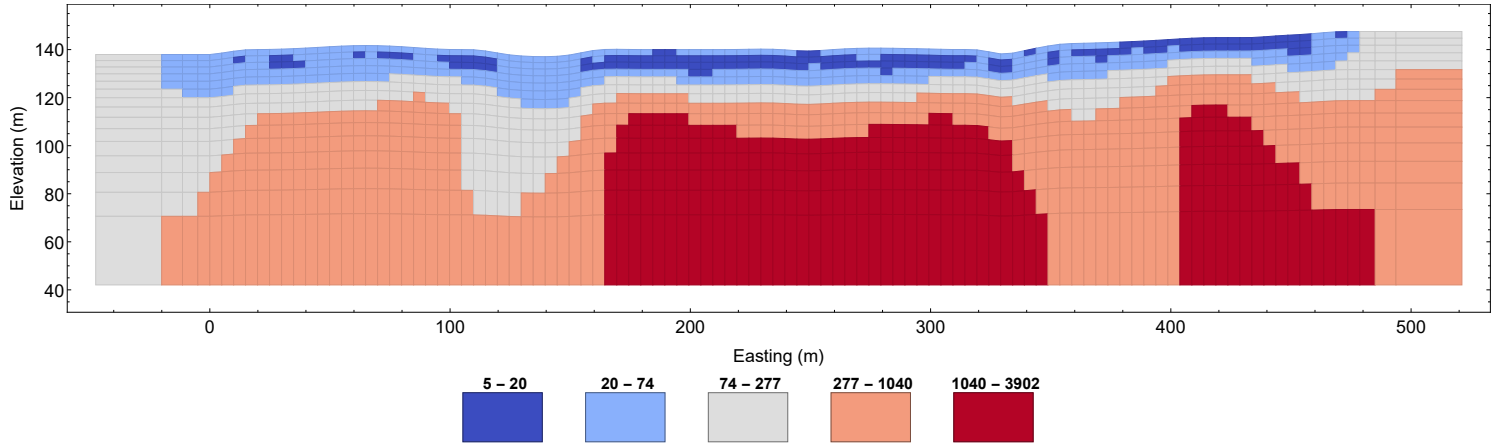

Figure 12.2: OKvau calibration line smooth solution displayed with 5 contours. The values are given in Ω·m.

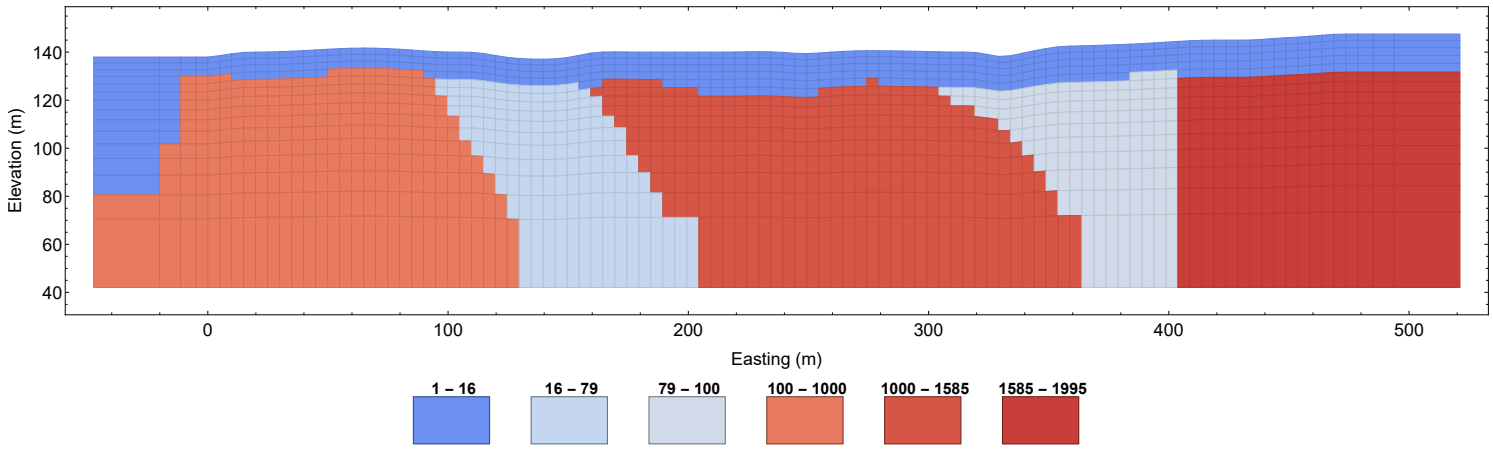

Figure 12.3: OKvau calibration line model based on the smooth solution and the geological information. The values are given in Ω·m.

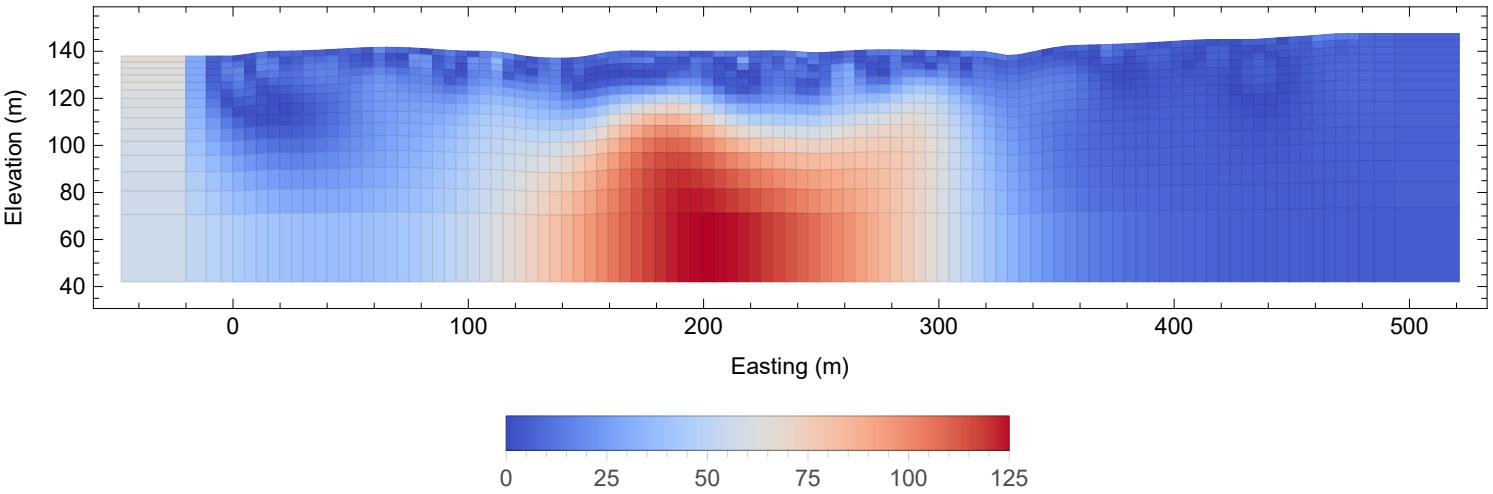

Figure 12.4: OKvau calibration line's chargeability smooth solution when Figure 12.3 is used as starting model.

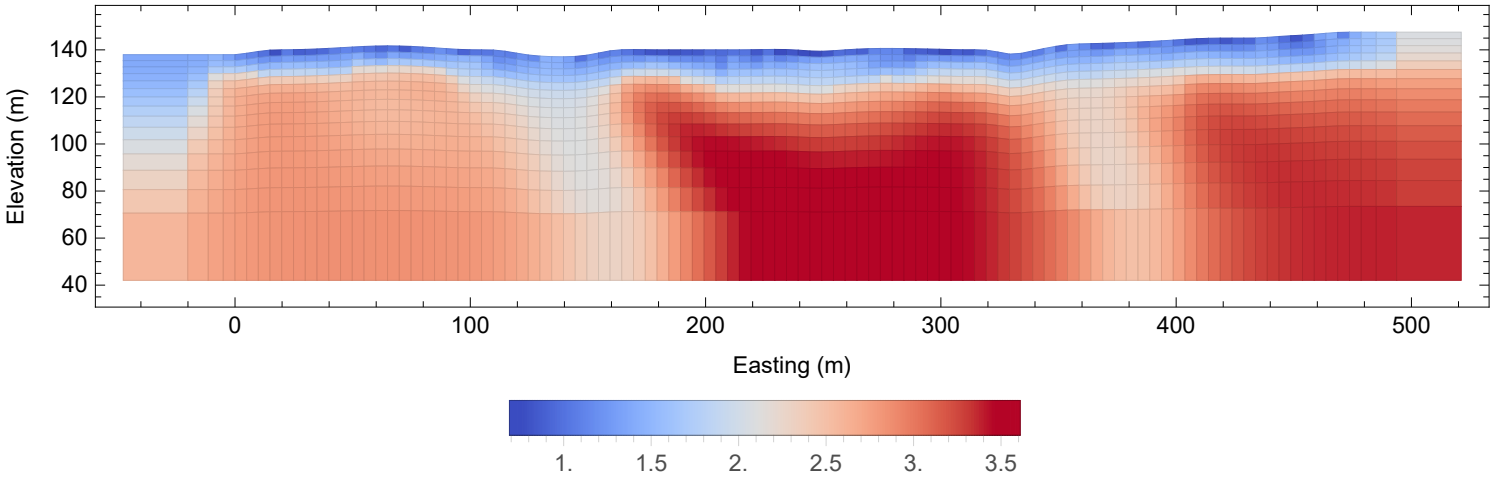

Figure 12.5: MGS resistivity starting model. Values in $\log_{10}$ of resistivity.

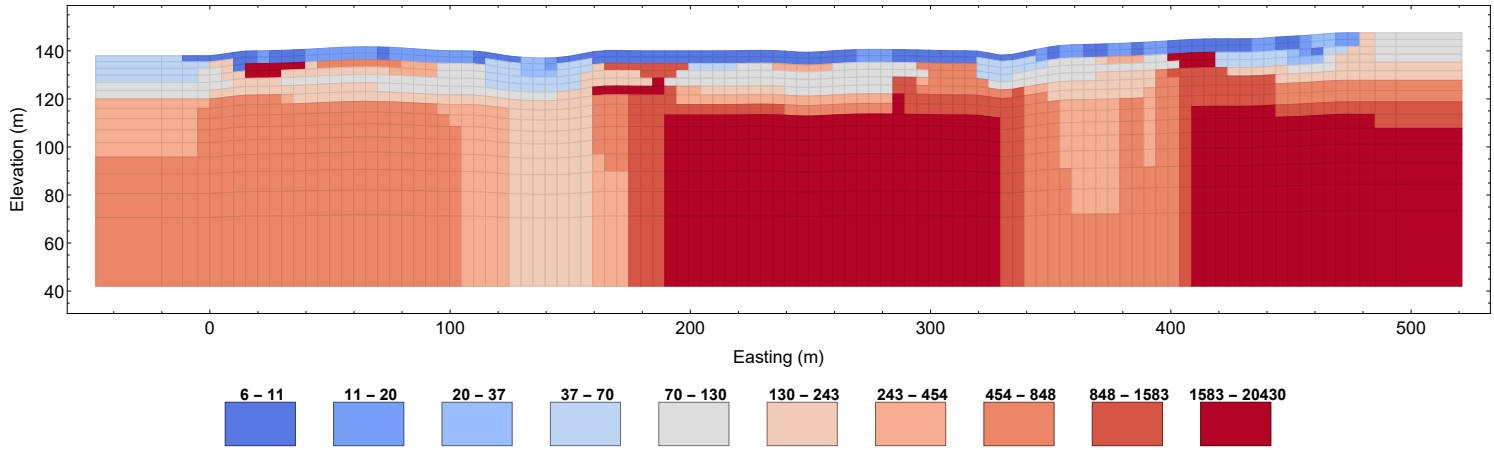

Figure 12.6: OKvau chargeability sharp solution with $\beta = 7.5 \times 10^{-4}$.

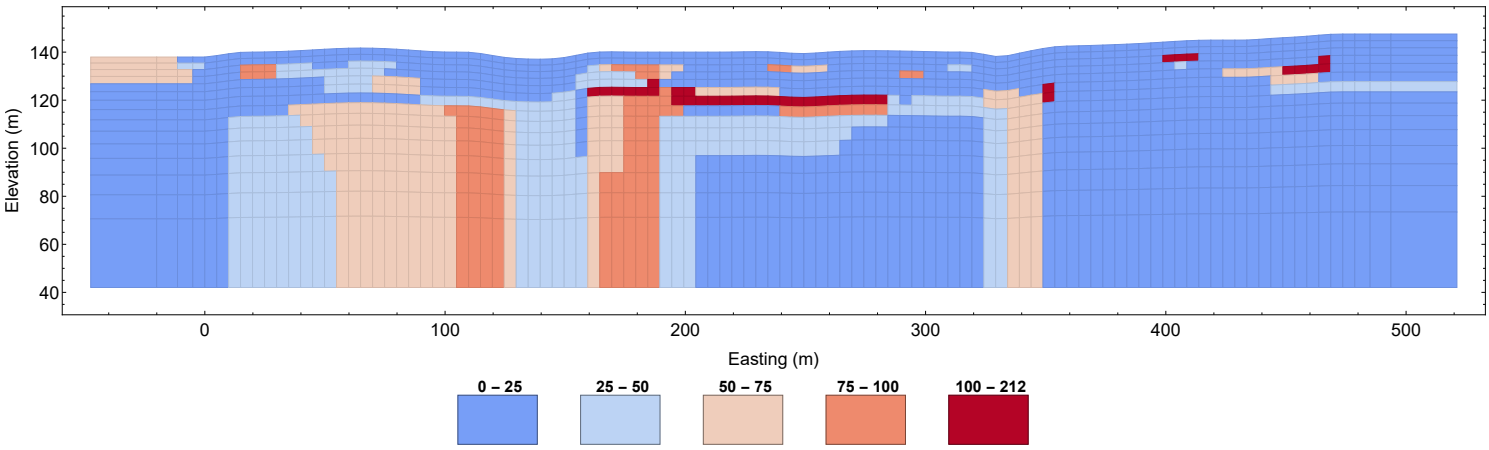

Figure 12.7: OKvau chargeability sharp solution with $\beta = 7.5 \times 10^{-4}$.

12.2.1 Interpretation

Descriptive observations

The main chargeability feature is identified at 200 m from the start of the profile by the smooth solution (Figure 12.4). It coincides with the south-east dipping mineralization zone. However, it is located just below four missing electrodes. Indeed, a large pit filled with water, result of the artisanal mining, was present. It makes sense to detect a chargeable zone in the rock below this area since the artisanal miners exploit vein continuation in the regolith.

The hosting rock is mainly diorite, and the contact with the sedimentary sequence is visible on both resistivity profiles at around 400 meters from the start (Figure 12.2 and Figure 12.6), but no chargeability anomaly is detected at this zone.

The IP sharp solution (Figure 12.7) suggests that the chargeable mineralized zone adheres on resistivity contrasts, perhaps due to a fractured/veined zone. Precaution must be taken because of the lack of data points in the area located between 100 and 200 meters from the start.

Small chargeable anomalies appears in the first 20 meters of the subsurface, and may be linked to the regolithic material exploited by the artisanal miners.

Link with previous geophysical study

The chargeable zone conforms with the previous study conclusions, it is located in zones of low to medium resistivity, nearby an elevated magnetic susceptibility feature.

Link with petrophysics

The resistivity values of the diorite and hornfels match with the ones computed. The conductive zone between 100 and 200 meters from the start should correspond to an altered diorite zone.

Solutions comparison

The two solutions behave as expected from the previous trials on synthetic models. Thanks to the information available, the sharp inversion was able to resolve the structure of the rock formations at the borders of the profile rather than smooth them out. They both allow the same interpretation in terms of resistivity, but the sharp solutions suggests that the surface contains a lot of small chargeable features, an that the main chargeable body adheres to the wall of a fractured zone, rather than being smoothly distributed around the conductive zone.

12.3 ORman 1

12.3.1 Computation

The smooth resistivity and chargeability solutions were computed. The resistivity model was consistent with the drill holes and the geological map, indicating diorite altered to some degree.

The smooth solution was used as the starting model for the sharp inversion. The β value judged the most adequate is 7.0×10^{-4}.

12.3.2 Interpretation

Descriptive observations

The highly resistive diorite is easily recognizable along the profile. There seems to be an altered zone of greater conductivity between 250 and 400 meters from the start. The eastern lithological contact, marked by a fault (see Figure 6.2), can be guessed by a resistivity shift at around 100 meters from the start. It also corresponds to a depression in the relief, visible on the surface.

The altered zone seems to be linked with low chargeability features between 25 and 50 mV/V, and a small anomaly of great magnitude on the surface. Within the diorite, at 600 meters from the start, a medium chargeability body is recognizable. It is located just below a conductive inclusion within the resistive diorite on the subsurface.

From these observations, the diorite in the ORman area does not seem to be of great interest in terms of mineralization.

Link with previous geophysical study

Figure 7.2 shows that ORman 1 is located within a zone of high magnetic anomaly, typical of magmatic intrusions, whereas mineralizations at OKvau is linked to deep low magnetic anomalies. Furthermore, the ambient elevated resistivity and the absent chargeable bodies does not match with the rule established by Bourne (2016).

Link with petrophysics

The computed resistivity values is consistent with the value from the petrophysics study. The medium chargeable bodies recovered from the inversions could correspond to fractured or veined zones but with low mineralizations. The interpreted altered diorite zone between 250 and 500 meters was drilled up to 100 meters deep. The logs confirm that some fractures are present with little amount of pyrite mineralization.

Solutions comparison

The contact zone at about 100 meters from the West is better resolved with the sharp inversion, as well as the diorite/sandstone contact at the end of the profile. More subsurface chargeability features are also resolved compared to the smooth solution.

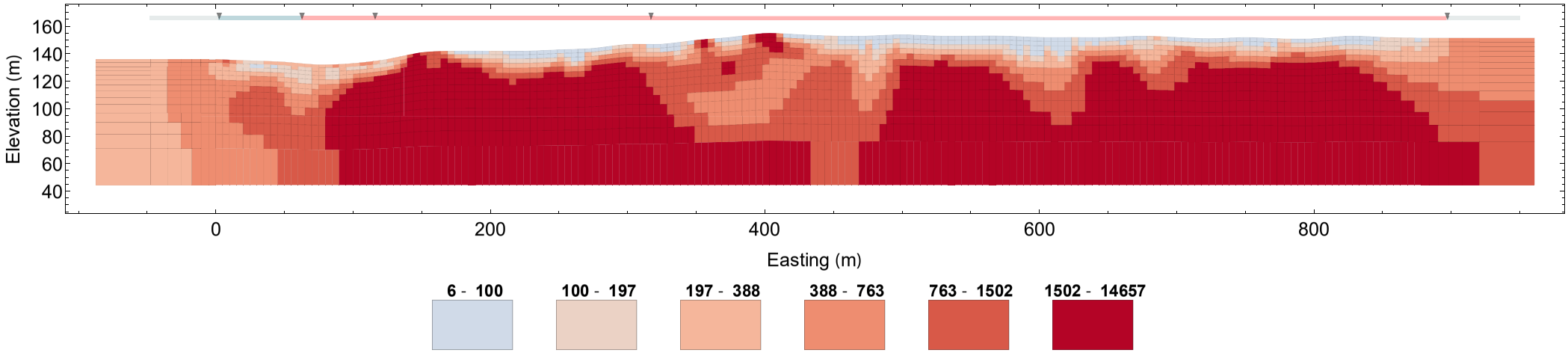

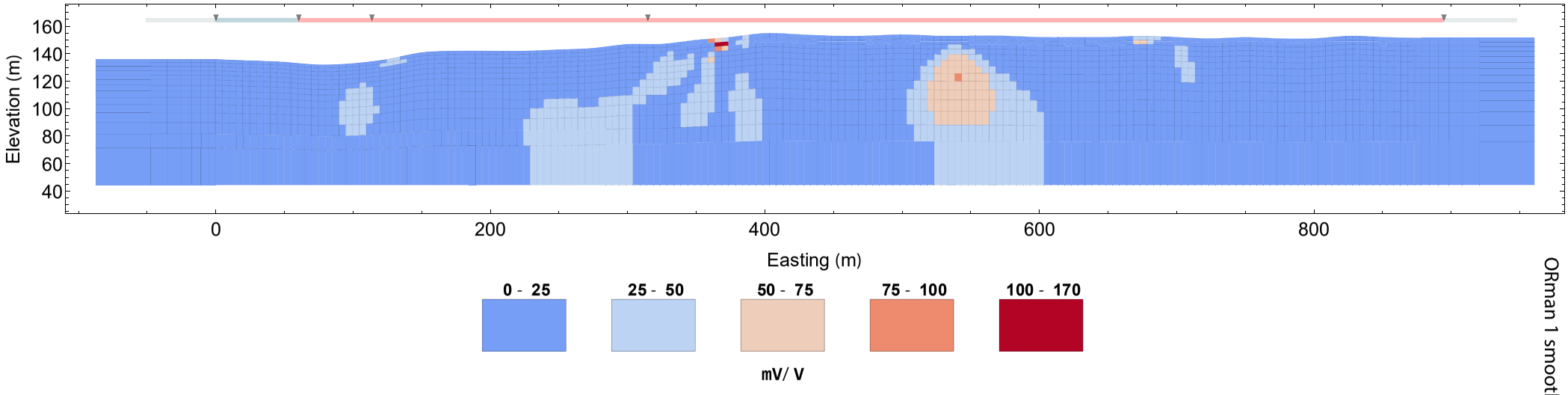

ORman 1 smooth solution

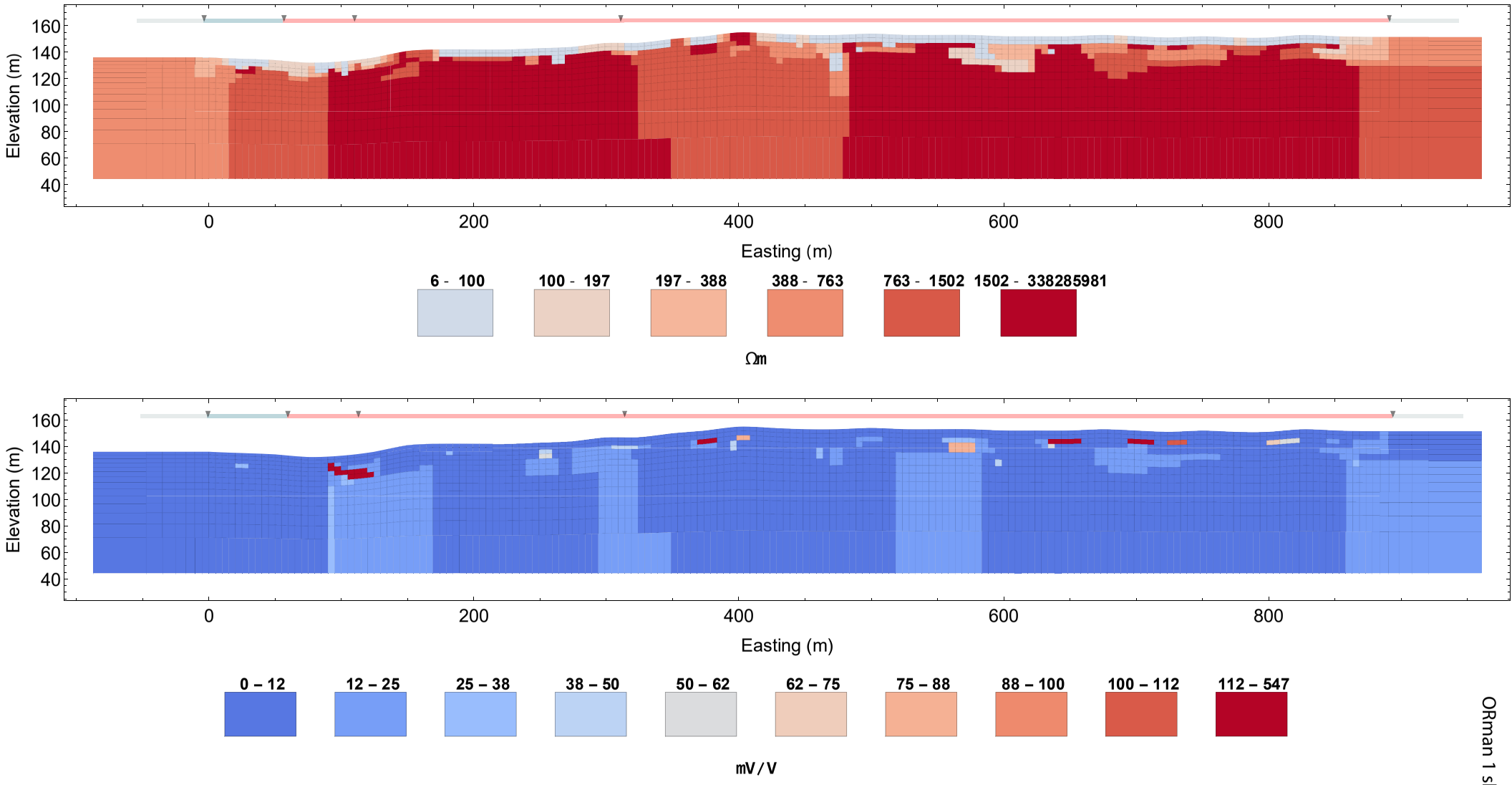

ORman 1 sharp solution

12.4 ORman 2

12.4.1 Computation

The smooth resistivity and chargeability solutions were computed. The smooth solution was used as the starting model for the sharp inversion. The β value judged the most adequate is $1{\times}10^{-3}$.

12.4.2 Interpretation

Descriptive observations

The contact diorite/siltstone at 550 meters from the West is well defined on both solutions, as well as the contact siltstone/sandstone a hundred meters on the west. Both these contacts seem to be linked with great chargeable zones, located in the outside of the conductive zone, that is linked to a fault crossing the siltstone as can be seen on Figure 6.2. The siltstone formation seems to be greatly altered, as indicated by the conductive area between 850 and 950 meters from the start. This zone is associated with high subsurface chargeability features of great magnitude. Another chargeable body is located at around 300 meters from the start, within the diorite.

In this particular profile, the chargeable anomalies are linked with an elevated resistivity regardless of the lithology.

Link with previous geophysical study

As can be seen on Figure 7.2, the main chargeable zone located between 500 and 800 meters from the West is linked with a magnetic low, in the neighbourhood of a fault zone. However, the chargeable anomalies lie within highly resistive rock.

Link with petrophysics

The situation does not seem to match with the cases discussed in the petrophysics study. Drilling in the chargeable zones defined on the section should bring light on their mineralization state.

However, the high resistivity associated to high chargeability could be a sign of disseminated sulphides. It could correspond to the situation on the bottom right of Figure 4.3, where veined/banded, poorly connected mineralizations occur, as illustrated by the texture sketches.

Solutions comparison

As expected, the several lithological contacts across the section are better resolved with the sharp inversion, based on the resistivity solution. The smooth inversion produces a chargeable body at around 300 meters from the start which is not present in its sharp counterpart. The main chargeable bodies located between 500 and 800 meters in the smooth solution are extended horizontally in the sharp solution, and are both associated with highly resistive rocks.

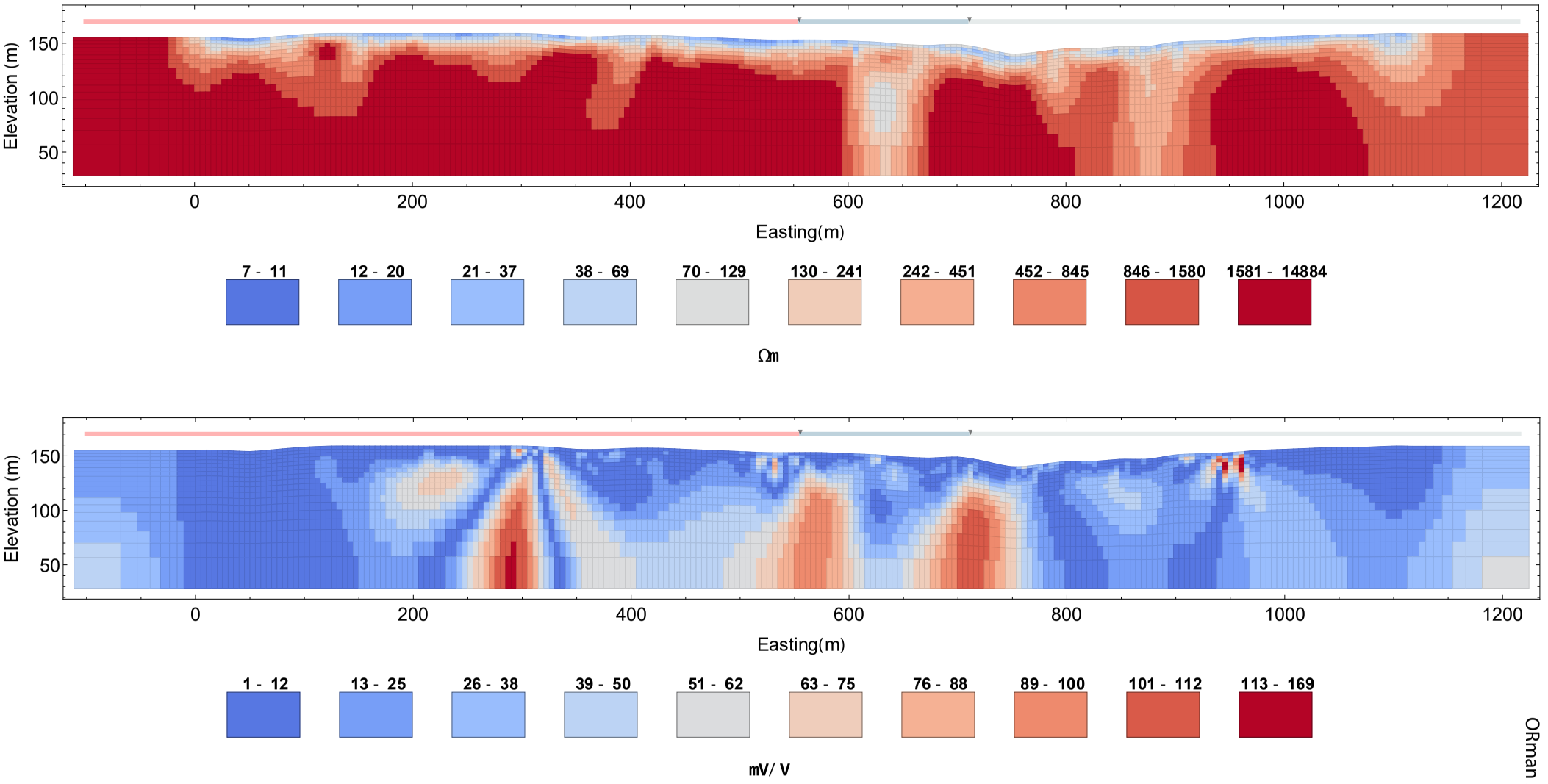

ORman 2 smooth solution

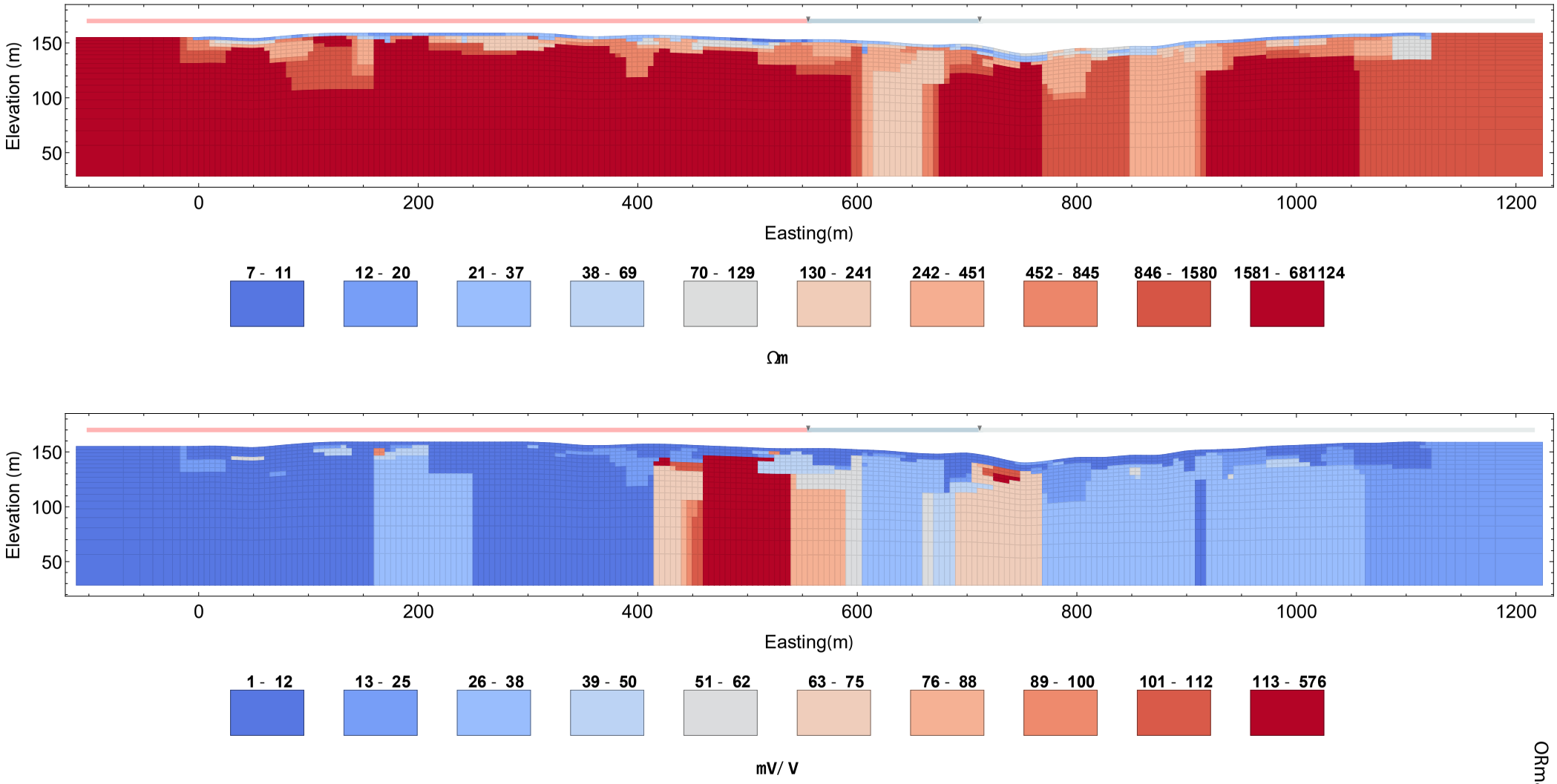

ORman 2 sharp solution

12.5 ORman 3

12.5.1 Computation

The smooth resistivity and chargeability solutions were computed.

The smooth solution was used as the starting model for the sharp inversion. The β value judged the most adequate is 7.0×10^{-4}.

12.5.2 Interpretation

Descriptive observations

The lithological contact between the diorite and the siltstone at 250 meters from the start is well defined, based on the resistivity solution. The fault zone between the siltstone and the sandstone can be inferred from the more conductive zone 400 meters from the start. It would seem that the contact between the sandstone and the granodiorite on the east, defined by the geological map, could be shifted 50 meters to the right, or maybe the contact zone, defined by a low resistivity zone at 900 meters from the East, has an oblique component in the east direction.

One could expect the presence of chargeable bodies due to the presence of the conductive zones at lithological contacts, but only low chargeability magnitude bodies seem to appear, mainly confined to resistive rocks.

Link with previous geophysical study

From the RTP magnetic map (Figure 7.2), it would be expected to find chargeable zones since the western half of the section covers the magnetic low zone. However, it is not the case. One interpretation would be that the mineralized, chargeable zone plunges deeper into the rock, towards the SW direction.

Link with petrophysics

The resistivity values are in accordance with the petrophysical study for the inferred lithologies.

Solutions comparison

The lithological contacts at 300 and 500 meters from the start in the smooth solution are more evident with the sharp inversion, as well as the inferred altered siltstone zone in the eastern part of the profile.

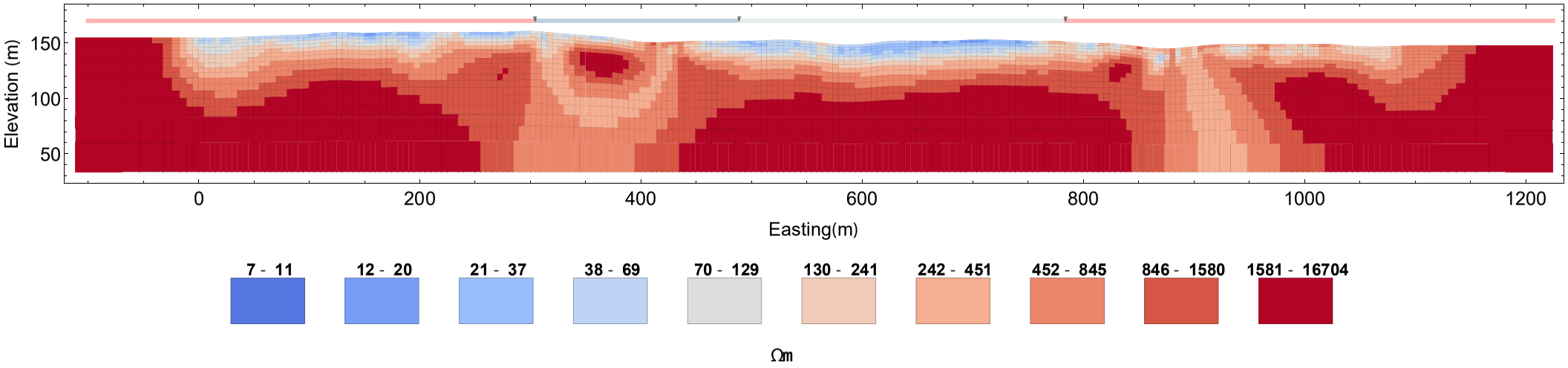

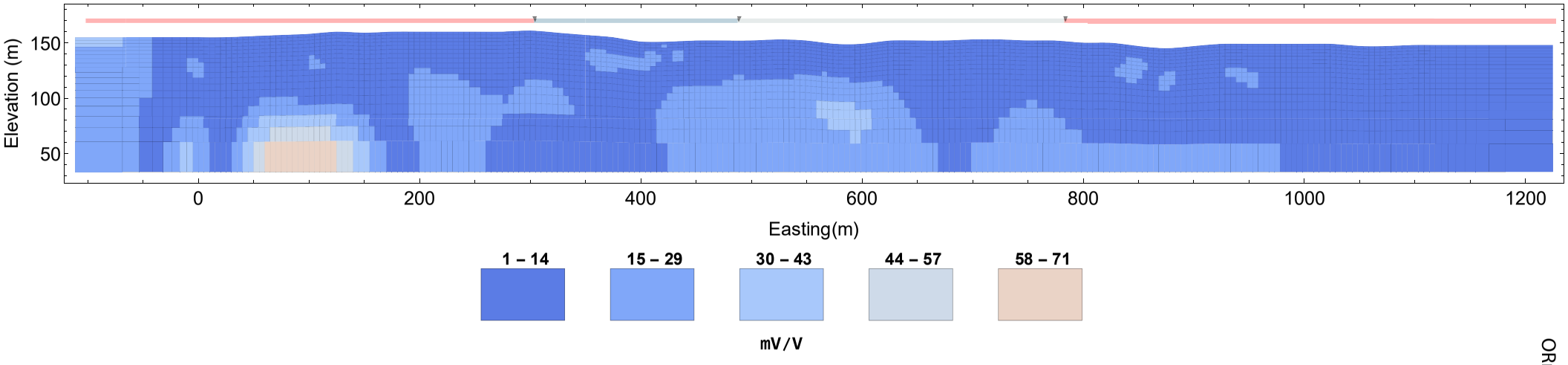

ORman 3 smooth solution

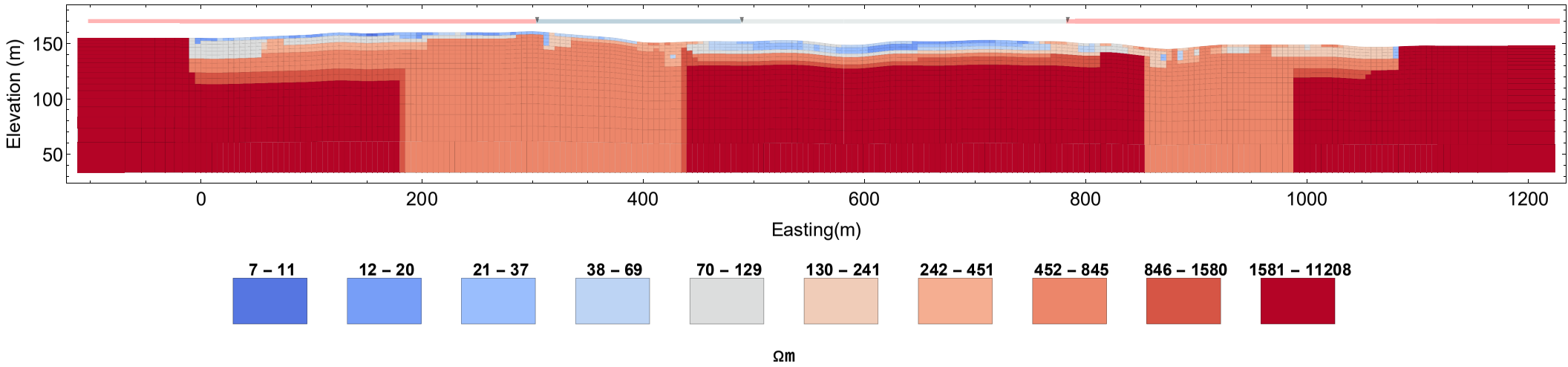

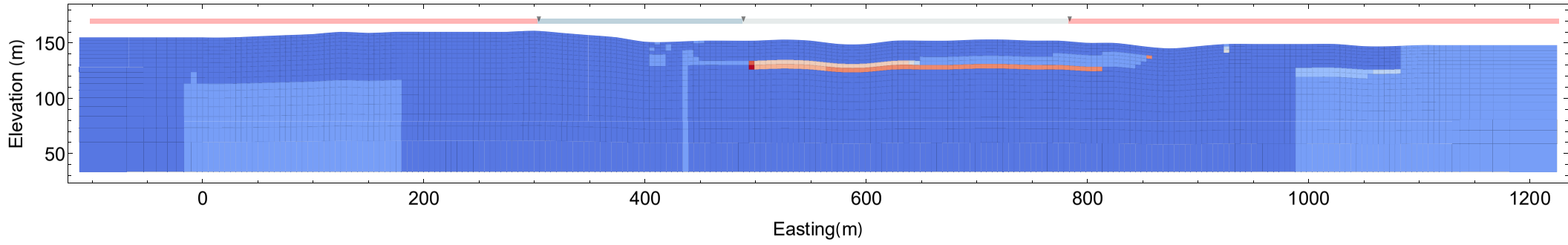

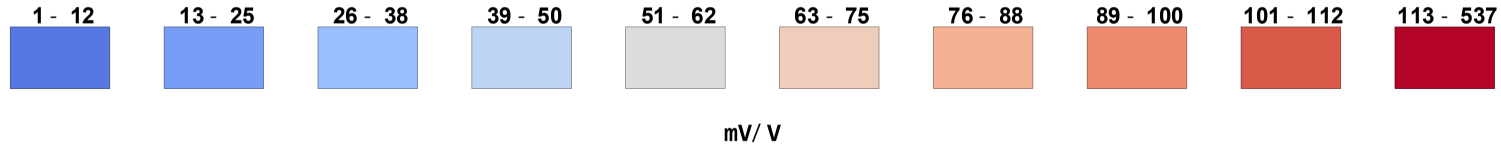

ORman 3 sharp solution

12.6 ORman 4

12.6.1 Computation

The smooth resistivity and chargeability solutions were computed.

The smooth solution was used as the starting model for the sharp inversion. The β value judged the most adequate is 20×10^{-4}.

12.6.2 Interpretation

Descriptive observations

The first contact from the East (diorite/siltstone) is recognizable from the resistivity contrast. At 600 meters from the start, the contact zone between the sandstone and the granodiorite can easily be inferred from the medium resistivity zone surrounded by resistive formations. However, the fault zone passing between the siltstone and sandstone formation (see Figure 6.2) can not be guessed from the resistivity results. The chargeability of this profile is fairly low.

Link with previous geophysical study

The section line is located at the southern tip of the magnetic low anomaly Figure 7.2. From this observations and the last profiles chargeability results, it is obvious that there exists a correlation between the magnetism and the chargeability features magnitudes.

Link with petrophysics

From the lack of chargeable zones, it can be inferred that the section area lacks in sulphide mineralizations. Otherwise, there is no significant departure from the resistivity values determined by the petrophysics study.

Solutions comparison

The sharp resistivity solution offers significant interpretation advantage when identifying lithological contacts. Especially at 200 and 600 meters from the East.

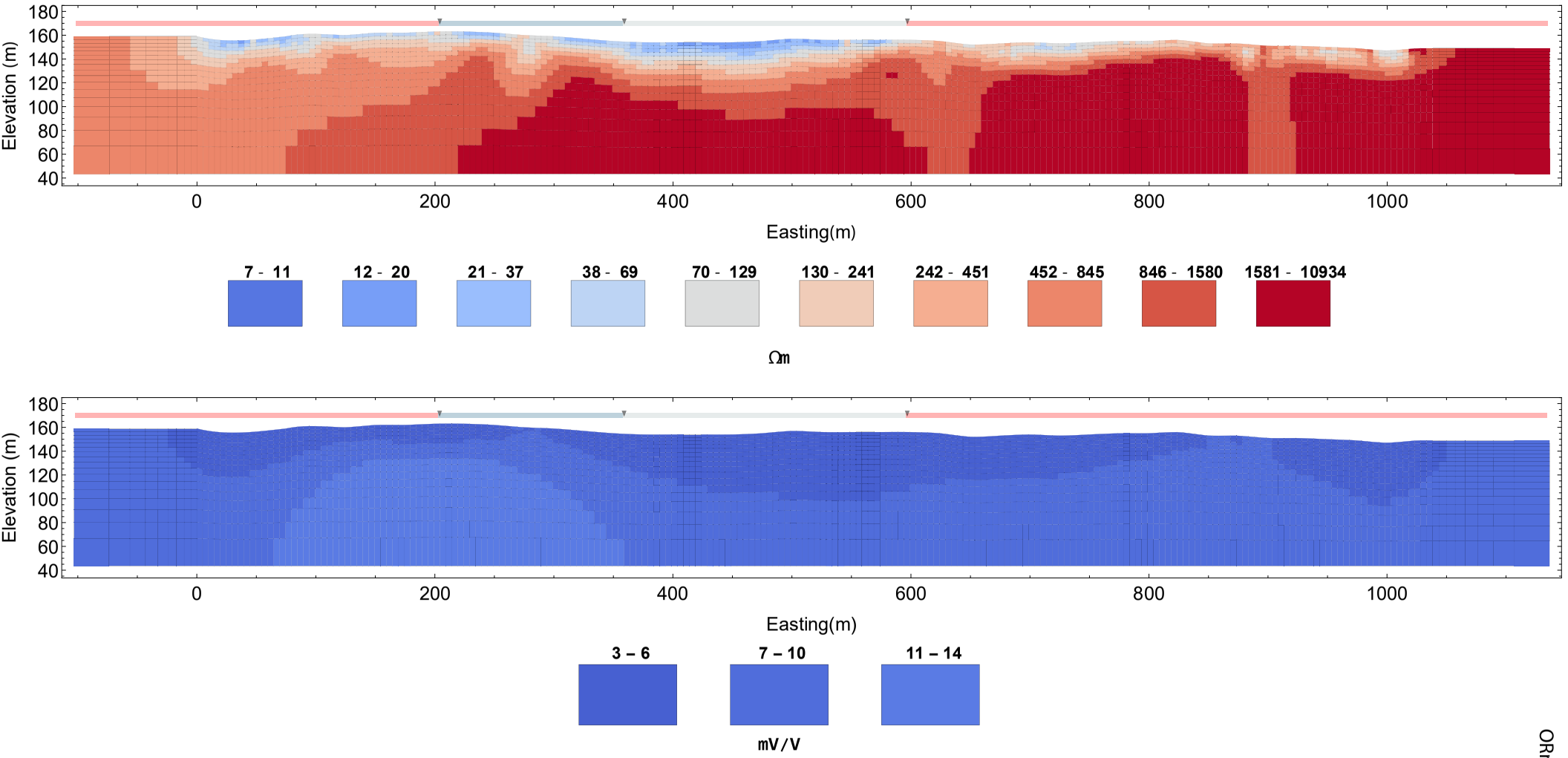

ORman 4 smooth solution

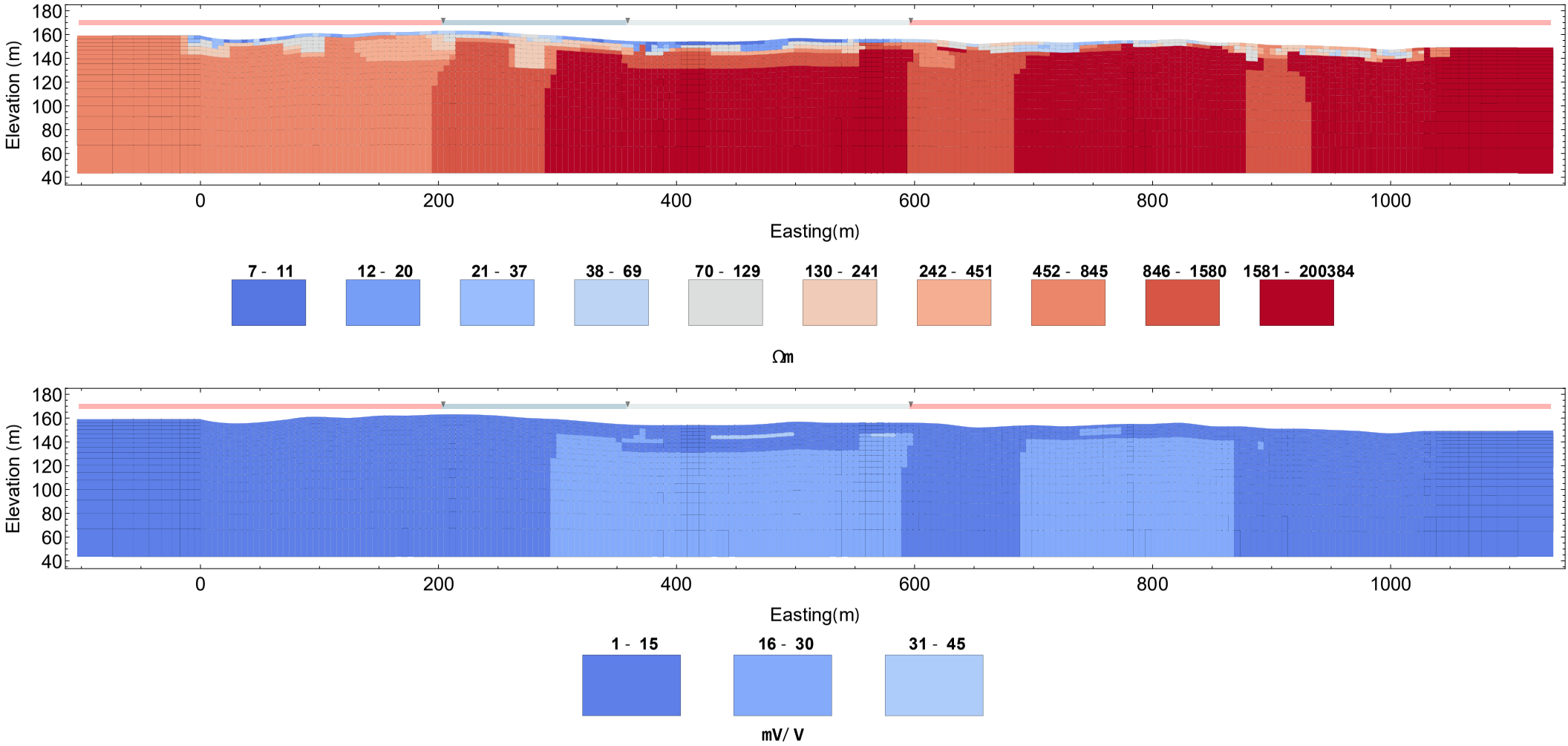

ORman 4 sharp solution

Discussion

The MGS approach allows to better identify lithological contacts. It facilitates interpretation when several lithologies are present, and it preserves the sharp contact at the section borders. However, as stressed out in Chapter 10, the inversion necessitates a starting model to allow its convergence. It requires much more time and interpretation skills to use this approach, but the results can be rewarding.

The sharp inversions suggest that mineralized zones in the OKvau section adheres to the wall of conductive zones, and that globally more chargeability features exists in the subsurface, features that may have been smoothed out by the classic inversion scheme.

It is observed that the chargeable zones are linked to zones characterized by magnetic lows, and high resistivity in the ORman case. Drilling boreholes in the chargeable area in ORman 2 could remove the ambiguity about its origin.

There seems to be a southern-decreasing trend of the chargeability state of the underground.

Chapter 13

Conclusion

The objective of this thesis was to establish new guidelines in the application of the Minimum Gradient Support functional, applied to a real and large electrical investigation campaign.

13.1 Minimum Gradient Support implementation

The functional was first applied to synthetic cases artificially contaminated by a Gaussian noise component. It was observed that it offers significant advantages in the interpretation of simple models with two bodies of different resistivity. Indeed, the resulting images were closer to the true model than the classic solution, which tends to smooth out the resistivity contrasts of interest.

When more complex synthetic resistivity models were implemented, the method failed to faithfully recover the resistivity structure of the underground. The smooth inversion scheme however was able to resolve the presence of the different bodies. When combined with the smooth solution as a starting model, the sharp inversion finally converges towards satisfactory results.

The influence of the a-priori information was then further explored in a synthetic DC/IP investigation scenario, similar to the conditions of the OKvau prospect. The imagined a-priori information available were :

- Geological mapping.
- Boreholes data.
- Petrophysics study.

It allowed to constraint the inversion in a way to recover a solution that is superior to the classic Occam's solution.

Finally, using the guidelines developed in the synthetic trials, the method was applied to the field data of this thesis, and the results were compared with the smooth solution.

It appeared that the sharp inversion provides useful hindsight in the resistivity structure, as clearer images were produced. The sharp resistivity solutions suggests that several anomalies lies in the subsurface, not present in the smooth solution.

13.1.1 Focusing parameter

Several attempts were made to automate the choice of the focusing parameter β, but due to time constraints, it was left to the user judgement, for a battery of trials and errors results. The value chosen had to produce a model that was in accordance with the a-priori information.

13.1.2 Advantages

- The MGS approach can provide models that are very close to the true solution, especially when dealing with relatively simple models, compared to the classical smooth solution.
- When lots of information is available, it allows to tune the smooth solution towards a more realistic, sharper solution.
- The method is well suited to resolve lithological contacts.

13.1.3 Disadvantages

- Requires a-priori information and interpretation skills. It is much more time costing than the smooth inversion scheme.
- The choice of the focusing parameter β adds a level of complexity, it is necessary to test an array of values in order to select one that produces a coherent solution.
- It is not popular. It is relatively recent and proper guidelines do not exist yet.

13.1.4 Perspectives

During the realization of this work, it was tried to automate the choice of the focusing parameter, however, the outcomes were inconclusive and/or took too much time. The following ideas should be further explored in future research.

1. For an array of β values, selecting the one that minimizes the data misfit.
2. Perform a line-search on β at each iteration and pick the one that minimizes the data misfit.
3. Start from a large β value, and divide it at each iteration by a certain factor.

Another idea would be to select the β value that reconstructs certain geological features, utilizing image processing techniques. I have come to be persuaded that the choice of the focusing parameter could be automated given enough time to develop the proper algorithm, and that the a-priori information will play an preponderant role in its selection.

I hope this thesis will open the door for a larger implementation of the Minimum Gradient Support approach in geophysical studies, not only in electrical methods, and bring more research towards the automation of the choice of the focusing parameter.

13.2 DC/IP results

The survey designed aimed to characterize the ORman prospect zone by using electrical resistivity tomography and induced polarization. A calibration line was first realized on the extensively-studied OKvau prospect, to calibrate the measurements of the ORman area.

Four profiles parallel to each other, crossing the lithological contacts between a magmatic intrusive and the sedimentary hosting sequence, allowed to estimate the chargeability state of the underground following the south-west trend of the structure. It was observed that chargeable materials lie preferentially at the contact zone between lithologies, and are correlated with a low magnetic anomaly. Previous drilling survey, geophysical and petrophysical studies conducted by private consultants helped in the interpretation of the results and to constrain the solution during the inversion process.

The chargeability state of the underground decreases towards the south. The results could also suggest that significant mineralization occur at greater depth below the low magnetic anomaly.

13.2.1 Perspectives

From the chargeability magnitudes, the profile ORman 2 seems to be the more promising in terms of mineralization. However, boreholes should be realized to confirm its potential.

Bibliography

Aizebeokhai, Ahzegbobor P. and Kehinde D. Oyeyemi (2014), "The use of the multiple-gradient array for geoelectrical resistivity and induced polarization imaging." *Journal of Applied Geophysics*, 111, 364–376, URL http://dx.doi.org/10.1016/j.jappgeo.2014.10.023.

Ajo-Franklin, Jonathan B., Burke J. Minsley, and Thomas M. Daley (2007), "Applying compactness constraints to differential traveltime tomography." *Geophysics*, 72, R67–R75, URL http://library.seg.org/doi/10.1190/1.2742496.

Alliborne, A (2013), "Geological setting and targeting of Au (As, Bi, Te, W, Mo) mineralization in the OKvau District, NE Cambodia. Consultant report prepared for Renaissance Minerals Ltd."

Alliborne, A (2014), "Petrography of 16 specimens from the OKvau gold deposit, Cambodia. Consultant report prepared for Renaissance Minerals Ltd."

Ashley, PM (2006), "Petrographic Report on Nineteen Rock Samples from the OKvau Gold Prospect, Cambodia. Consultant report prepared for Oxiana Ltd."

Aster, Richard C., Brian Borchers, and Clifford H. Thurber (2013a), "Introduction." *Parameter Estimation and Inverse Problems*, 1–23, URL http://linkinghub.elsevier.com/retrieve/pii/B978012385048500001X.

Aster, Richard C., Brian Borchers, and Clifford H. Thurber (2013b), "Nonlinear Inverse Problems." In *Parameter Estimation and Inverse Problems*, 239–252, Elsevier, URL http://linkinghub.elsevier.com/retrieve/pii/B9780123850485000100.

Aster, Richard C, Brian Borchers, and Clifford H Thurber (2013c), "Nonlinear Regression." *Parameter Estimation and Inverse Problems (Second Edition)*, 217–238.

Bar, Moshe and Maital Neta (2007), "Visual elements of subjective preference modulate amygdala activation." *Neuropsychologia*, 45, 2191–2200, URL http://linkinghub.elsevier.com/retrieve/pii/S0028393207001042.

Binley, A (2015), "Tools and Techniques: Electrical Methods." In *Treatise on Geophysics*, volume 11, 233–259, Elsevier B.V., URL http://linkinghub.elsevier.com/retrieve/pii/B9780444538024001925.

Binley, Andrew (1995), "Regularised Image Reconstruction of Noisy Electrical Resistance Data." *Proceedings of the 4th Workshop of the European Concerted Action on Process Tomography,*, 401–410.

Blaschek, R., A. Hördt, and A. Kemna (2008), "A new sensitivity-controlled focusing regularization scheme for the inversion of induced polarization data based on the minimum gradient support." *Geophysics*, 73, F45–F54, URL http://geophysics.geoscienceworld.org/content/73/2/F45.abstract.

Bolster, S (2012), "Field Visit to OKvau Project, Cambodia. Internal memo, Renaissance Minerals Ltd."

Bourne, B (2015), "The Geophysical Response of Intrusion Related Gold with an Example from Okvau, Cambodia." 2015, 1–39.

Bourne, B (2016), "IP / Resistivity and Magnetic 3D Inversion, Okvau, Cambodia." Technical report.

Bourne, Barry and Lynelle Beinke (2015), "OKvau project." Technical report, Terra resources pty ltd.

Dahlin, Torleif and Bing Zhou (2006), "Multiple-gradient array measurements for multichannel 2D resistivity imaging." *Near Surface Geophysics*, 4, 113–123.

Franey, Nick (2014), *Geology of the Okvau gold deposit, Cambodia.* Internal Report, Renaissance Minerals Ltd.

Glover, PWJ (2015), "Geophysical Properties of the Near Surface Earth: Electrical Properties." In *Treatise on Geophysics*, 89–137, URL http://linkinghub.elsevier.com/retrieve/pii/B9780444538024001901.

Halliday and Resnick (2015), *Fundamental of Physics 10th Edition*, volume 1.

Hart, C (2005), "Classifying, distinguishing and exploring for intrusion-related gold systems." *The Gangue*, 1–18.

Hart, Craig J R and Rich Goldfarb (2005), "Distinguishing intrusion-related from orogenic gold systems." *New Zealand Minerals Conference ...*, 2703, 125–133.

Hart, Craig J.R. (2007), "Reduced Intrusion-Related Gold Systems." *Exploration Methods: Geological Association of Canada, Mineral Deposits Division, Special Publication*, 5, 95–112.

Kamvong, T (2014), "A review of the Cu-Au Metallogeny and Tectonics of Mainland SE Asia. Consultant report prepared for Renaissance Minerals Ltd."

Kearey, Philip, Michael Brooks, and Ian Hill (2002), *An Introduction to Geophysical Exploration*, 3rd edition. Blackwell Science Ltd.

Kemna, Andreas (2000), "Tomographic inversion of complex resistivity." *Ruhr-Universität Bochum*, 169, URL http://www2.geo.uni-bonn.de/members/kemna/Kemna{_}2000{_}PhD{_}thesis.pdf.

Kemna, Andreas, Andrew Binley, Giorgio Cassiani, Ernst Niederleithinger, André Revil, Lee Slater, Kenneth H. Williams, Adrián Flores Orozco, Franz Hubert Haegel, Andreas Hördt, Sabine Kruschwitz, Virginie Leroux, Konstantin Titov, and Egon Zimmermann (2012), "An overview of the spectral induced polarization method for near-surface applications." *Near Surface Geophysics*, 10, 453–468.

King, S (2008a), "Interpretation of the Regional Fault Architecture of Cambodia from Landsat TM and Aster Satellite Imagery. Consultant report prepared for Oz Minerals Cambodia Ltd."

King, S (2008b), "Structural Interpretation of drilling at the OKvau Project, Cambodia. Consultant report prepared for Oz Minerals Cambodia Ltd."

King, S (2010), "Phase 2 Structural logging and interpretation of drilling at the OKvau Project, Cambodia. Consultant report prepared for Oz Minerals Cambodia Ltd."

Kirsch, Andreas (2011), *An Introduction to the Mathematical Theory of Inverse Problems*. URL http://books.google.com/books?hl=en{&}lr={&}id=RTo9ZFaSSugC{&}pgis=1.

Last, B. J. and K. Kubik (1983), "Compact gravity inversion." *Geophysics*, 48, 713–721.

Loke, D. M. (1999), "Electrical imaging surveys for environmental and engineering studies." *Cangkat Minden Lorong*, 6574525, 63.

Loke, M H (2015), "Electrical imaging survey for environmental and engineering studies." *A practical Guide to 2D and 3D surveys*, 187, URL http://seisweb.oma.be/bibadmin/uploads/pdf/COURSENOTES.pdf{%}5Cnwww.geotomosoft.com.

Loke, M. H., J. E. Chambers, D. F. Rucker, O. Kuras, and P. B. Wilkinson (2013), "Recent developments in the direct-current geoelectrical imaging method." *Journal of Applied Geophysics*, 95, 135–156, URL http://dx.doi.org/10.1016/j.jappgeo.2013.02.017.

Loke, M.H. (2017), "RES2DINV, GeoTomo Software."

Lowrie, William (2007), *Fundamentals of geophysics*. Cambridge University Press.

Moreland, Kenneth (2009), "Diverging color maps for scientific visualization." *Lecture Notes in Computer Science (including subseries Lecture Notes in Artificial Intelligence and Lecture Notes in Bioinformatics)*, 5876 LNCS, 92–103.

Morris, S. (2017), *Topology without tears*. URL http://www.topologywithouttears.net/topbook.pdf.

Nguyen, Frederic, Andreas Kemna, Tanguy Robert, and Thomas Hermans (2016), "Data-driven selection of the minimum-gradient support parameter in time-lapse focused electric imaging." *Geophysics*, 81, A1–A5, URL http://library.seg.org/doi/10.1190/geo2015-0226.1.

Oldenburg, Douglas W. and Yaoguo Li (1994), "Inversion of induced polarization data." *GEOPHYSICS*, 59, 1327–1341, URL http://library.seg.org/doi/10.1190/1.1443692.

Parasnis, D. S. (1962), *Principles of applied geophysics*, volume 84. URL http://www.worldcat.org/oclc/1245225.

Portniaguine, Oleg and Michael S. Zhdanov (1999), "Focusing geophysical inversion images." *GEOPHYSICS*, 64, 874–887, URL http://library.seg.org/doi/10.1190/1.1444596.

Rosas Carbajal, Marina, Niklas Linde, and Thomas Kalscheuer (2012), "Focused time-lapse inversion of radio and audio magnetotelluric data." *Journal of Applied Geophysics*, 84, 29–38, URL http://dx.doi.org/10.1016/j.jappgeo.2012.05.012.

Routh, Partha S and Douglas W Oldenburg (2001), "Electromagnetic coupling in frequency-domain induced polarization data: a method for removal." *Geophysical Journal International*, 145, 59–76.

Ruffet, C., M. Darot, and Y. Guéguen (1995), "Surface conductivity in rocks: a review." *Surveys in Geophysics*, 16, 83–105.

Seigel, Harold O. (1959), "Mathematical formulation and type curves for induced polarization." *Geophysics*, 24, 547–565, URL http://library.seg.org/doi/10.1190/1.1438625.

Sen, Pabitra N. and Peter A. Goode (1992), "Influence of temperature on electrical conductivity on shaly sands." *GEOPHYSICS*, 57, 89–96, URL http://library.seg.org/doi/abs/10.1190/1.1443191.

Sumner, J.S. (1976), "Principles of induced polarization for geophysical exploration." *Elsevier Scientific, Amsterdam*, 277.

Systems Exploration (NSW) Pty Limited. (2008), "Petrophysical results - Systems Exploration (NSW) Pty Limited. Report realized for Oxiana (Cambodia) Ltd / Oz Minerals Cambodia." Technical report.

Telford, Wm, Lp Geldart, and Re Sheriff (1990), "Electrical Properties of Rocks and Minerals." In *Applied geophysics*, chapter Electrical, 283–292, Cambridge University Press.

Tikhonov, Nikolaevich Andre I and V. Y. Arsenin (1977), *Solutions of ill posed problems*. Winston.

Wolfram Research Inc. (2017), "Mathematica, Version 11.1."

Zhdanov, M. S. (1993), "Tutorial: Regularization in Inversion Theory." Technical report, Center for Wave Phenomena, Colorado School of Mines.

Zhdanov, M S, G Vignoli, and T Ueda (2006), "Sharp boundary inversion in crosswell travel-time tomography." *Journal of Geophysics and Engineering*, 3, 122–134, URL http://stacks.iop.org/1742-2140/3/i=2/a=003?key=crossref.c21ec8fdd890df92164ae6ba544f4afe.

Zhdanov, Michael and Ekaterina Tolstaya (2004), "Minimum support nonlinear parametrization in the solution of a 3D magnetotelluric inverse problem." *Inverse Problems*, 20, 937–952.

Zhdanov, Michael S. (2009), *Geophysical Electromagnetic Theory and Methods*, 1 edition. Elsevier B.V., URL http://linkinghub.elsevier.com/retrieve/pii/S0076689509700010.

Zhdanov, Michael S (2015), *Inverse Theory and Applications in Geophysics Inverse Theory and Applications Second Edition*, 2nd edition. Elsevier B.V.

Zonge, Kenneth L. and Larry J. Hughes (1985), "Effect of electrode contact resistance on electric field measurements." *SEG Expanded Abstracts*, 85716, 231–234.